2023

Icing Mitigation via High-pressure Membrane Dehumidification in an Aircraft Thermal Management

Danielle D. Hollon
Wright State University

ICING MITIGATION VIA HIGH-PRESSURE MEMBRANE DEHUMIDIFICATION IN AN AIRCRAFT THERMAL MANAGEMENT SYSTEM

A dissertation submitted in partial fulfillment
of the requirements for the degree of
Doctor of Philosophy

by

DANIELLE D. HOLLON
B.S., College of Charleston, 2016
M.S.M.E., Wright State University, 2019

2023
Wright State University

Wright State University
COLLEGE OF GRADUATE PROGRAMS AND HONORS STUDIES

April 11, 2023

I HEREBY RECOMMEND THAT THE DISSERTATION PREPARED UNDER MY SUPERVISION BY Danielle D. Hollon ENTITLED Icing Mitigation via High-pressure Membrane Dehumidification in an Aircraft Thermal Management System BE ACCEPTED IN PARTIAL FULFILLMENT OF THE REQUIREMENTS FOR THE DEGREE OF Doctor of Philosophy.

Mitch Wolff, Ph.D.
Dissertation Director

Ahsan Mian, Ph.D.
Program Director
Ph.D. in Engineering Program

Shu Schiller, Ph.D.
Interim Dean
College of Graduate Programs
& Honors Studies

Committee on
Final Examination

Mitch Wolff, Ph.D.

James Menart, Ph.D.

Abdeel Román, Ph.D.

José Camberos, Ph.D., P.E.

ABSTRACT

Hollon, Danielle D., Ph.D., Engineering Ph.D. Program, Department of Mechanical and Materials Engineering, Wright State University, 2023. *Icing Mitigation via High-pressure Membrane Dehumidification in an Aircraft Thermal Management System.*

Icing, or the formation of ice from water via freezing or water vapor via desublimation, is a phenomenon that commonly occurs within air cycle-based refrigeration systems and requires thermal control that limits system performance. In aircraft applications icing frequently occurs in the heat exchangers and turbine(s) that are part of the air cycle machine, the refrigeration unit of the environmental control system. Traditionally, water vapor is removed from an air cycle machine via condensing in a heat exchanger and subsequent high-pressure water separation. This approach is not capable of removing all of the vapor present at low altitude conditions, corresponding to a high risk of icing. To mitigate icing under these conditions, a membrane dehumidifier is considered to separate the water vapor that remains after condensing and liquid water separation.

Three distinct investigations are conducted as part of this work. The first is aimed at modeling approaches for desublimation frosting, or frost growth on sufficiently cold flat surfaces. This results in a novel, analytical, and non-restrictive solution well-suited for representing frost growth and densification in moist air heat exchangers. The second investigation concerns membrane dehumidification and module design. A custom component model is developed and verified under aircraft conditions, then the Pareto frontier of volumetrically efficient membrane modules is characterized via a multi-objective optimization study. The final investigation evaluates three two-wheel air cycle subsystem architectures with differing dehumidification approaches: (1) condenser-based, (2) membrane dehumidifier-based, and (3) combined. Steady-state simulations are run for each of these over a range of flow rates and altitudes. The results demonstrate that incorporating a membrane dehumidifier reduces the turbine inlet saturation temperature, which mitigates icing in the turbine and reduces the required bypass flow, thus increasing the cooling capacity.

This research was sponsored by the Air Force Research Laboratory located at Wright-Patterson Air Force Base, OH. The views and conclusions contained herein are those of the author and should not be interpreted as necessarily representing the official policies or endorsements, either expressed or implied, of Air Force Research Laboratory or the U.S. Government. Distribution Statement A: Approved for Public Release; Distribution is Unlimited. PA# AFRL-2023-1808.

Nomenclature

Alphabetic/Acronyms	
2W-ACM	Two-wheel Air Cycle Machine
4W-ACM	Four-wheel Air Cycle Machine
ACM	Air Cycle Machine
a_0, a_1, a_2	coefficients of (2.15)
A	plate area (m^2)
A_{ext}	lateral exterior surface area of membrane fiber (m^2)
b_0, b_1, b_2, b_3	coefficients of (2.13)
Bi	Biot number
c, c_1	generic constants
c_p	specific heat capacity (J/kg·K)
C_{min}	minimum heat capacity rate (W/K)
C_r	ratio of min. to max. heat capacity ratio
CFD	Computational Fluid Dynamics
d_h	hydraulic diameter (m)
d_i	membrane fiber inner diameter (m)
d_o	membrane fiber outer diameter (m)
dz	differential length of control volume (m)
D	shell inner diameter (m)
D_{va}	diffusivity of water vapor in air (m^2/s)
DAE	Differential Algebraic Equations
ECS	Environmental Control System
f	friction factor
$Fo = \frac{\alpha t}{L^2}$	Fourier number

h	heat transfer coefficient, in Chapter 3
	enthalpy (J), in Chapter 4
HR	humidity ratio (kg_v/kg_a)
j	mass flux of water vapor ($kg/m^2 \cdot s$)
j_m	total mass flux of water vapor ($kg/m^2 \cdot s$)
$j_{m,cyl}$	water vapor mass flux for one fiber ($kg/m^2 \cdot s$)
Ja	modified Jakob number
k	thermal conductivity (W/mK), in Chapter 2
	mass transfer coefficient (m/s), in Chapter 3
k_{f0}	frost thermal conductivity (W/mK) intercept from (2.25)
$\tilde{k}$	ratio of k_{f0} and k_a
lnQ	logarithm of the accuracy ratio
L	plate length (m), in Chapter 2
	module length (m), in Chapters 3 and 4
Le	Lewis number
L_{sv}	latent heat of desublimation (J/kg)
k	mass transfer coefficient (m/s)
$m(X,\tau), M(X,\tau)$	generic ODE terms
$\dot{m}$	mass flow rate (kg/s) or (lbm/s) where specified
M	molar mass (g/mol)
MAE	Mean Absolute Error (%)
MAPE	Mean Absolute Percentage Error (%)
MD	Membrane Dehumidifier
MD-ECS	Membrane Dehumidification-based ECS
MRE	Mean Relative Error (%)
MRR	moisture removal rate (g/h)

n	generic iteration counter
N	number of membrane fibers/discretized segments
$n(X,\tau), N(X,\tau)$	generic ODE terms
Nu, Nu_L	Nusselt number
NTU	Number of Transfer Units
ODE	ordinary differential equation
p	pressure (Pa)
p_v	partial pressure of water vapor (Pa)
Pe	permeability (kg/m·s·Pa)
$PERC$	percentage of points within proportional error bands (%)
Pr	Prandtl number
PR	pressure ratio
q	specific humidity (kg_v/kg_a)
Q	rate of heat transfer (W)
r	overall mass transfer resistance (Pa·s/kg)
r_m	resistance to permeation (Pa·s/kg)
r_t	overall heat transfer resistance
R	universal gas constant (J/mol·K)
Re, Re_L	Reynolds number
RH	relative humidity (1) or (%)
Sc	Schmidt number
Sh	Sherwood number
t	time (s)
T	temperature (K) or (°C) or (°F)
TMS	Thermal Management System
u	velocity (m/s)

UA	overall heat transfer coefficient times area
V	membrane dehumidifier module volume (m^3)
w	humidity ratio (kg_v/kg_a)
$\tilde{w}$	supersaturation degree (kg/kg)
x	spatial coordinate (m)
x_s	frost thickness (m)
x_w	specific humidity (kg_v/kg_a)
X	non-dimensional frost thickness
z	longitudinal coordinate (m)
z^*	non-dimensional length

Greek

α	frost density time exponent
	thermal diffusivity of air, in Fourier number (m^2/s)
β	linear constant of k_f
δ	membrane thickness (m)
Δp	pressure drop (Pa)
$\Delta T = T_{dp} - T_w$	supercooling degree (K)
ϵ	effectiveness
η	efficiency (1) or (%)
γ	frost thickness time exponent
λ	thermal conductivity (W/m·K)
$\mu(X)$	integrating factor
ω	shaft speed (rpm)
ϕ	module packing density, in Chapter 3
	energy (kW), in Chapter 4

ρ	density (kg/m^3)
τ	non-dimensional time
θ	non-dimensional temperature
$\sum(\text{lnQ}^2)$	sum of the squared logarithm of the accuracy ratio

Subscripts

$1-12$	sensor location
a	moist air
amb	ambient
$bleed$	bleed air from engine
$calculated$	value predicted with model
$cond$	condensate/condensation
$cool$	coolant
$corr$	corrected
deh	dehumidification
des	design
dp	dew point
f	frost, in Chapter 2
	feed side of membrane dehumidifier, in Chapters 3 and 4
fm	air-membrane interface on the feed side
i	arbitrary discretized segment of MD component model
ice	ice
in	inlet
max	maximum
$measured$	empirical value found via experiment
$mech$	mechanical

min	minimum
p	permeate side of membrane dehumidifier
pm	air-membrane interface on the permeate side
$poly$	polytropic
ram	ram air
ref	reference
s	frost surface
sat	saturation
set	turbine outlet set point
sub	sublimation
tp	triple point
$turb$	turbine
v	water vapor
vap	vaporization
w	wall/plate surface
x	along plate length

Contents

List of Figures

List of Tables

Acknowledgment

The research presented here would not have been possible without years of discussion and collaboration with my colleagues in the Mechanical and Thermal Systems branch of the Air Force Research Laboratory. Thanks to Dr. Abdeel Roman, Dr. Larry Byrd, Travis Michalak, Jim Tschantz, and Earl Gregory who all provided feedback on the direction and documentation of this work, and a particular thanks to Nick Truster for the extended discussions and many rounds of edits that served to greatly improve this work.

I would also like to thank the students, faculty, and staff at Wright State University who helped me navigate multiple programs and departments. I am particularly grateful to the members of my committee - the time and effort they have given this work is greatly appreciated. A special thanks to Dr. Mitch Wolff, who showed unwavering support and kindness.

Further, many thanks to my friends and family who have supported and encouraged me through this academic journey. Especially my wonderful, patient husband, Jeffrey Hollon, and his parents, John and Jennifer Hollon, who welcomed me from day 1. Finally, many thanks to my parents, Beth and Gaétàn Massé, and sister, Rachelle Massé - my academic pursuits would never have been possible without their love and enthusiastic support.

For Jeffrey and Shiva,

who light up my life.

Introduction and Background

Over several generations of aircraft, air cycle machines (ACMs) have been the primary thermal management system (TMS) used to dissipate heat loads during flight. Fundamentally, an ACM is governed by the reverse Brayton gas refrigeration cycle which consists of a compressor, turbine, and one or more heat exchangers (HXs). In practical implementations, these systems incorporate additional components to ensure operability over relevant ranges of pressure, temperature, and humidity conditions. The cooling capacity of an ACM can be increased in two ways: (1) increase the flow rate, and (2) produce air at a lower temperature. Increasing the flow to an ACM means taking more bleed air from the engine, which directly impacts engine performance and aircraft range. Therefore, it is more desirable to lower the temperature of the air that the ACM produces. While low temperatures can be achieved with current turbomachinery, decreasing the turbine outlet temperature below freezing leads to the formation of ice crystals. This ice travels downstream and collects on available surfaces, such as ducts, valves, or heat exchanger faces, ultimately clogging the ACM flowpath. To enable subfreezing air cycle outlet temperatures, the water vapor must be removed before expansion in the turbine. Here, the suitability of a membrane dehumidifier to dry the air upstream of the turbine, thus mitigating turbine outlet icing, is evaluated.

1.1 Two-Wheel Air Cycle Machines

An ACM is a practical implementation of a gas refrigeration cycle, also called the reverse Brayton cycle. The idealized cycle occurs over four processes:

1-2: The gas is compressed to a high-pressure, high-temperature state.

2-3: The gas is cooled at a constant pressure to T_0 by rejecting heat to the surroundings.

3-4: The gas is expanded in a turbine to a low-temperature state.

4-1: The cool gas absorbs heat from the refrigerated environment.

The ideal cycle and its T-s diagram are shown in Figure 1.1. As this is an ideal gas refrigeration cycle, each of the processes are internally reversible and the compression and expansion are assumed to be adiabatic and reversible.

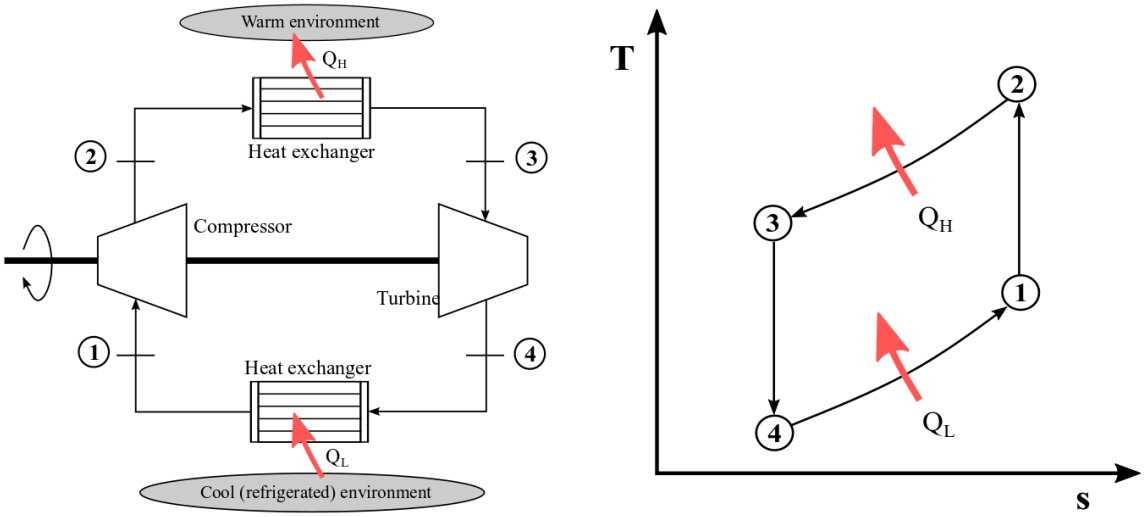

Figure 1.1: An idealized reverse Brayton cycle (left) and the corresponding $T - s$ diagram (right). Recreated from [1].

In real gas refrigeration cycles, the compression and expansion processes are not isentropic and thus $T_3 > T_0$ with a finitely sized HX. While the gas refrigeration cycle has a lower coefficient of performance when compared to the reverse Carnot or vapor com-

pression cycle, it is still the most desirable for aircraft environmental control applications because of the comparatively simple and light constituent components [1].

The fundamental components of an ACM are a HX, compressor, and turbine, connected in line as shown in Figure 1.2. The two pieces of turbomachinery - the compressor and turbine - are the reason this architecture is referred to as two-wheel; there are many other ACM architectures that incorporate additional wheels via fans and/or additional turbines. Further, this is an open air cycle system, meaning that working fluid is continuously supplied and removed from the system rather than remaining within the system at all times, as in the closed ideal cycle shown in Figure 1.1. The purpose of this system, and moreover the environmental control system (ECS), is to provide adequately cool air where it is needed - typically, the cool air is supplied to downstream HXs which regulate the temperature of avionics and hydraulic systems, as well as the cabin.

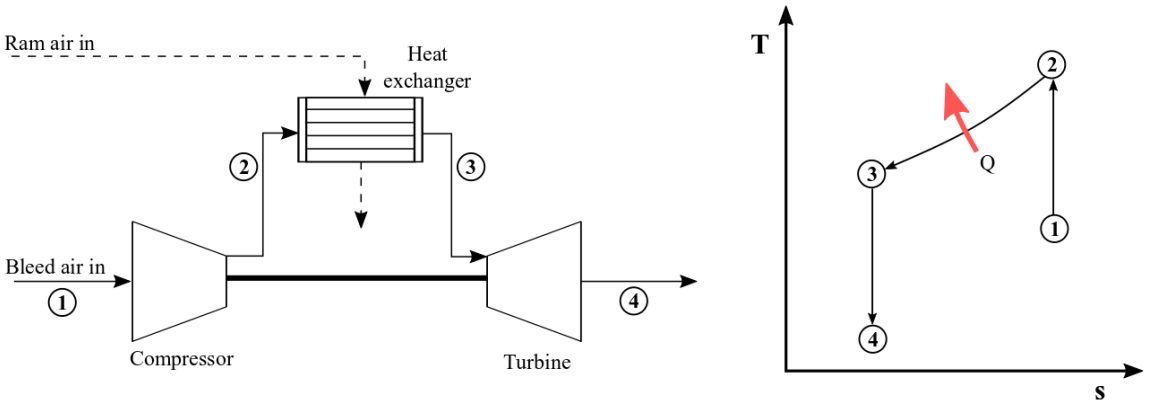

Figure 1.2: An idealized aircraft air cycle machine and its $T - s$ diagram.

While the system shown in Figure 1.2 is capable of providing the cool air needed to dissipate these heat loads, aircraft systems incorporate additional components, shown in Figure 1.3, to properly control the temperature and humidity of the working fluid [21]. The condenser and high-pressure water separator (HPWS) serve to dehumidify the air before expansion; the condenser brings the air to saturation, removing vapor via condensing, then the HPWS coalesces and separates the entrained water droplets from the flow. The primary

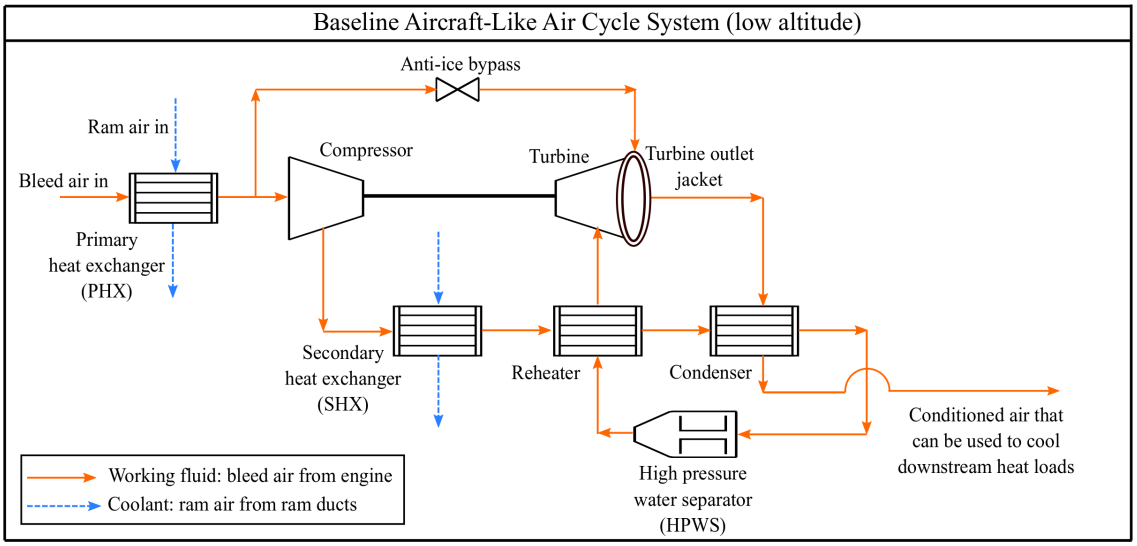

Figure 1.3: A traditional aircraft-like ACM with high-pressure water separation system.

HX is introduced to pre-cool the air before compression, decreasing the work required by the compressor. The secondary HX is vital for system functionality - by rejecting heat here, the system is able to reach sub-ambient temperatures out of the turbine. The reheater is introduced to reduce the inlet temperature to condenser, making it easier to reach saturation. Overall, the turbine is driven by bleed air from the aircraft engine, and its power is transmitted via a single shaft to the compressor. To avoid icing at the turbine outlet, an anti-ice bypass is used to allow hot air to bypass the air cycle machine altogether and heat the turbine outlet; typically, the bypass flow controller is set to regulate the turbine outlet temperature to a few degrees above freezing.

1.1.1 Hydrophobic Coatings to Delay Icing Onset

The research and development of icephobic coatings to mitigate icing on aircraft surfaces has been the focus of much work in recent years [3, 22–24]. This work has resulted in the advancement of manufacturing and fabrication methods for coatings as well as an increased understanding of ice nucleation and adhesion. Application of hydrophobic coatings have been shown to repel water droplets, delay ice nucleation, and significantly reduce ice ad-

hesion [3]. However, despite the capability of icephobic coatings to delay icing, they are not represented as a part of this work since the ultimate goal is to mitigate icing rather than just delay its onset; hybrid approaches to delay and mitigate icing could be the subject of future studies.

1.1.2 Previous Modeling Investigations of Air Cycle Machines

In addition to works investigating hydrophobic coatings to delay icing onset, there have been many physical modeling and simulation investigations of relevant subsystems. In 2011, Tu and Lin developed a three-wheel ECS model with dynamic control in Flowmaster to achieve above-freezing turbine outlet temperatures [25]. In 2014, Jordan and Schmitz developed a Modelica library for scalable modeling of an aircraft ECS; the same year Santos et al. conducted a thermodynamic study of an ACM capable of determining an optimal ECS design in response to dynamic flight and cabin parameters [26, 27]. In 2017, exergy analysis of a three-wheel bootstrap ACM in Modelica revealed highly variable system performance over a range of simulation scenarios [28]. More recently, Jennions et al. conducted simulations of a Boeing 737 ECS in MATLAB® Simscape™, the software tool utilized for the current work [29]. Concurrently, a series of academic theses focused on modeling and simulation of commercial aircraft ECS have emerged as well [30–32].

From these investigations, much has been learned about how to best represent component behavior under aircraft operating conditions; however, the level of fidelity of these works with respect to humidity and phase change modeling varies by a large margin. Some efforts choose to use a dry air model [26, 27, 31, 32], and others employ idealized water separation techniques such that no water will be present in or downstream of the turbine, eliminating humidity and the associated phase change effects from their results [25, 28, 29]. The work that most realistically represents phase change within a refrigeration cycle is shown in [30]; unfortunately, the frost growth and melt models are incorporated into a commercial library, and are only applied to vapor compression systems in the scope of

the thesis. Hence, the literature indicates that modeling and simulation of icing and its mitigation in air cycle machines is limited.

1.2 Phase Change as Moist Air is Cooled

In refrigeration applications involving moist air as the working fluid and/or coolant, such as ACMs, the water vapor present in the air can research saturation and subsequently change phase. Therefore, it is necessary to develop an understanding of humidity, saturation, and the progression of icing in cold internal moist air flows.

1.2.1 Humidity

Generally, humidity is the concentration of water vapor present in the air. To clearly quantify humidity in a variety of different physical systems and conditions, three primary definitions have been established as well as a number of related parameters.

(1) Absolute humidity is typically expressed as the mass of water vapor per volume of moist air, with units of kg/m^3. (2) Relative humidity, RH, is the ratio of how much water vapor is in the air, to the maximum amount of water vapor the air could potentially contain at a given temperature. In terms of physical properties, this is the ratio of the partial pressure of water vapor in the mixture to the equilibrium water vapor pressure at a given temperature; this ratio is typically reported as a percentage. Since relative humidity depends on the vapor partial pressure, it will increase as system pressure increases. Further, since hotter air has a higher carrying capacity for water vapor, it will decrease as temperature increases. (3) The final humidity measure is specific humidity, x_w, which is the ratio of water vapor mass to the total moist air mass with units or kg/kg, also called the mixing ratio; a similar measure is the humidity ratio, HR, which is the ratio of water vapor mass to the total air mass. These can be related to one another simply as:

$$x_w = \frac{HR}{1+HR} \implies HR = \frac{x_w}{1-x_w} \tag{1.1}$$

For a given air flow, its temperature and humidity determine its relationship to saturation. As air is cooled, if it reaches saturation then phase change of water vapor will occur via condensation, resulting in liquid water, or deposition (also called desublimation), resulting in solid water, i.e. ice.

1.2.2 Saturation

Per Romps, the dew point is the temperature to which air must be cooled, at a constant pressure, to reach saturation with respect to liquid water [2]. Hence, at the dew point, the vapor pressure is equal to the saturation pressure with respect to liquid water, and the relative humidity is 100% with respect to a planar surface of liquid. Similarly, the frost point is the temperature to which air must be cooled, at a constant pressure, to research saturation with respect to solid ice. Using the Rankine-Kirchhoff approximation, Romps derived accurate, explicit, and analytical expressions for the dew point and frost point as functions of temperature and relative humidity [2]. In his derivation, it is shown that the distinction between the dew and frost points concerns the interpretation of the relative humidity of the air - i.e., whether it is interpreted as with respect to a planar surface of liquid water or solid ice. This difference changes the expressions for the saturation vapor pressures, which involve specific heat capacities at constant volume for vapor, liquid, and solid forms of water. For the full derivation with comparison to empirical data, refer to Romps [2].

The expressions developed can be used to calculate the dew and frost point depressions, defined as the difference between the temperature and dew/frost point for a given humidity. The minimum depression will determine the mode of phase change, or, alternatively, the greater of the dew and frost points. This is because as air is cooled, it will pass through the maximum of the dew or frost point first, and so the corresponding phase change process is thermodynamically preferred to occur. This is used by Romps to construct the regions shown in Figure 1.4 for a range of temperatures and relative humidities, along with

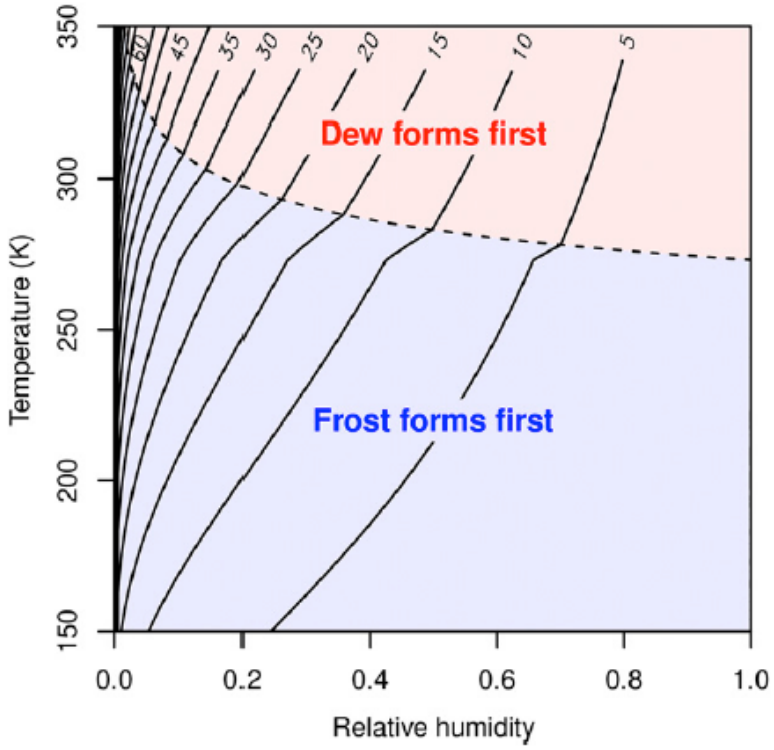

Figure 1.4: Maximum of dew and frost point depression over a range of relative humidity and temperatures, with the dashed line separating the region where, as air is cooled, dew forms first (red) and frost forms first (blue), as prepared by Romps [2].

the line of temperature and relative humidity conditions where the dew and frost points are equal [2]. Thus, if the dew point is greater than the frost point, then nucleation of water will preferentially occur and thus the phase change process is condensation. On the other hand, if the frost point is greater than the dew point, then solid ice will preferentially nucleate and the phase change process is deposition/desublimation [2, 33]. Further, as the relative humidity is reduced and temperature increased, it is observed that air moves farther from its saturation point; this is used to inform the air cycle architectures considered as part of this work.

1.2.3 Icing

Aircraft icing can be split into two categories: exterior and interior. Exterior icing is concerned primarily with icing due to the impact of supercooled water and ice on the exterior

surfaces of an aircraft, such as the wings and engine inlets. For aircraft at altitudes below ∼20,000 ft., exterior icing is particularly of concern due to the high concentrations of supercooled water droplets and ice crystals, as shown in the left of Figure 1.5.

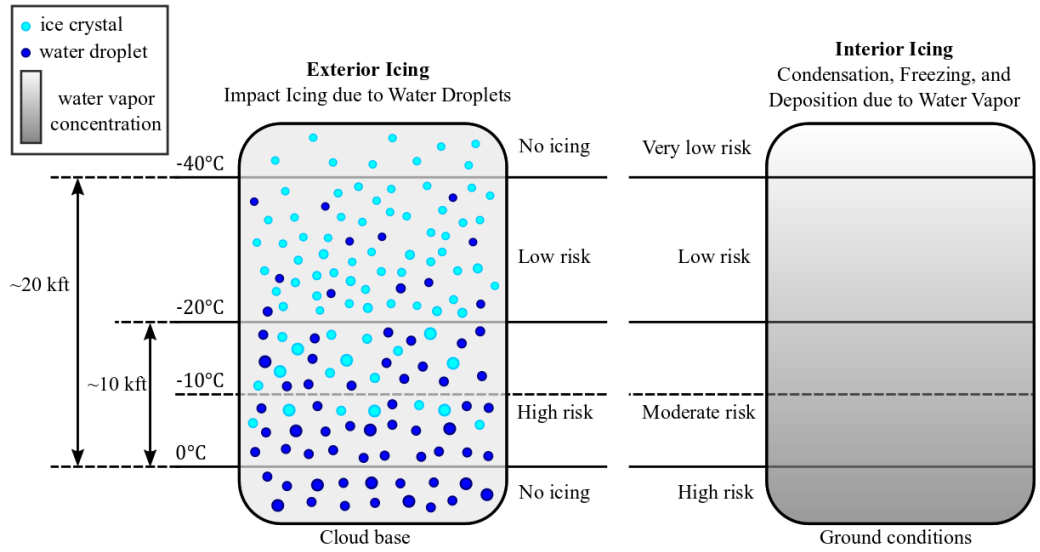

Figure 1.5: Water and ice formation (left, adapted from [3]) and water vapor concentration (right), within the lower atmosphere and the corresponding probability of aircraft icing.

Alternatively, interior icing is concerned with icing along interior flow surfaces [4]. The risk of interior icing is primarily dependent on the moisture of the atmospheric air, and decreases with increasing altitude as shown in the right of Figure 1.5. In typical aircraft operating conditions, the risk of interior icing is highest during ground and low altitude operations. The interior icing process can be split into two phase change processes: condensation frosting and desublimation.

Condensation Frosting

An idealized representation of the phase change progression via condensation frosting over time for a moist air flow over a cold flat plate is shown in Figure 1.6. This process consists of sequential stages of condensation on solid surfaces from vapor, freezing of the condensate, and then deposition of vapor on the ice surface [4]. Considering an ACM flowpath, condensation frosting may occur within the condenser - as the air is cooled to saturation,

if the wall is below freezing due to low turbine outlet temperatures, then the conditions for condensation frosting would exist. For a more in-depth review of approaches to model condensation frosting, refer to Zhao et al. [4].

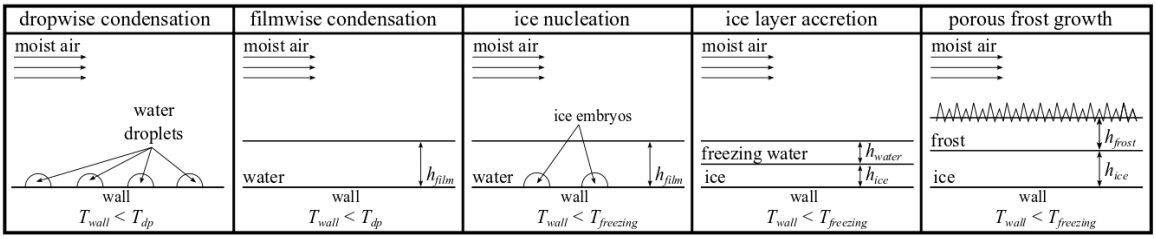

Figure 1.6: An idealized phase change progression for moist air flow over a sufficiently cooled surface. The progression shows the phase change processes that occur as time passes from left to right, with required wall temperatures, T_{wall}, shown for each stage relative to the dew and freezing point temperatures, T_{dp} and $T_{freezing}$ respectively. Adapted from [4].

Desublimation Frosting

Desublimation frosting is the direct formation of ice, without intermediate phase change. This can occur on solid surfaces, or within the air itself as snow when nucleation of ice and subsequent frost growth preferentially occurs around particulates [4, 33]. In an ACM, desublimation frosting occurs at the turbine outlet in the absence of thermal control via a bypass flow. This will occur if, as the air is expanded and thus cooled within the turbine, it passes through its saturation point. Hence, the turbine inlet saturation conditions are critical to properly mitigating icing.

1.3 Membrane Dehumidification

Air dehumidification is the process of removing water vapor from humid air. Dehumidification is most commonly done as a part of building air conditioning to provide comfortable thermal conditions. In an ACM, dehumidification is required to handle the ambient humidity present in the bleed air and prevent significant condensation and/or icing in the turbine. Typically, dehumidification is achieved via condensing.

In condensation-based dehumidification, the supply air is cooled to the its dew point, then to the dew point of the air to be supplied along a saturation curve, and finally reheated to the desired supply temperature. This process is inefficient due to the required over-cooling and re-heating of the air, but it currently in use in over 90% of air dehumidification systems [34]. An alternative to condensation-based dehumidification are desiccant-based dryers, which utilize desiccant materials. Desiccants bond with water vapor molecules, thus adsorbing them from the humid air stream. The most common desiccant dehumidification approaches use a solid desiccant wheel or a liquid desiccant, with the former typically requiring a condensation-based dehumidification system as well and the latter requiring cooling of the product air. Further, both styles of desiccant require regeneration via heat; hence, they only offer efficiency savings if free heat energy is available [34–37]. Moreover, the required maintenance of desiccant dryers makes them an undesirable choice. Another alternative that has garnered recent attention due to its low cost and limited energy consumption is membrane-based dehumidification [34, 38–41].

1.3.1 Membrane Dehumidifier Modules

Membrane-based dehumidification is achieved via a membrane dehumidification module, also called a membrane dehumidifier (MD), that is capable of efficient mass transfer of water vapor. These modules typically consist of hollow-tube fibers or sheets made from various polymers. As such, MDs consist of porous materials, and the pore size can be used to classify different types of modules - dense MDs typically have pores on the order of 10^{-1} nm, which porous MDs have pores on the order of 10^{-1} μm [42]. MD modules are typically constructed in either flat-plate or hollow-tube configurations. The flat-sheet style yields a flow pattern that resembles a crossflow plate-fin heat exchanger, with the feed and permeate flows separated by membrane sheets. The flow pattern of a hollow-tube style MD is more similar to shell-and-tube style heat exchanger, with the feed and permeate flows separated by hollow-fiber membrane tubes. Due to the circular cross-section of the feed

flow channels, the hollow-tube style is typically preferred over flat-sheet due to the smaller pressure drop [34]. Hence, hollow-tube style MDs will be the focus of this work.

1.3.2 Mass Transfer in Hollow-tube Style Membrane Dehumidifiers

Hollow-tube style MDs involve several modes of mass transfer that occur as shown in Figure 1.7. Under no pressure difference, water vapor will diffuse across the membrane based on the concentration gradient as stated by Fick's law of diffusion. However, in the strictest sense, Fick's law is only valid for a system of two components: a membrane, and one diffusing component [43]. With moist air being a mixture of multiple components, and hollow-fiber membrane tubes consisting of an arrangement of varying pore sizes along a non-porous polymer, there are more accurate descriptions of the mass transfer.

The transport of gas through a porous media can be accurately represented by the Dusty-Gas model [44–46]. For this model, a system of n gas species moving within a porous medium is viewed as a system of $(n + 1)$ constituents, with the porous medium itself viewed as giant, constrained molecules. This model takes into account the following independent and concurrent modes of transport: Knudsen flow, continuum diffusion, viscous flow, and surface diffusion [46]. On the other hand, for a dense, non-porous membrane, or the regions of a porous membrane with pore diameters smaller than 5 $\mathring{A}$, gas permeation across the membrane is best described by the solution-diffusion model [43,47]. This mode of transport takes place in three steps: absorption of a constituent into the membrane, diffusion through the solid membrane along a concentration gradient, and desorption at the opposing membrane interface. Separation of different constituents is achieved due to differences in the amount of material that diffuses, and its' rate of diffusion; this can be quantified by the permeability and selectivity of a membrane material with respect to different permeating constituents.

For the MD module under consideration here, the hollow-fibers are known to be man-

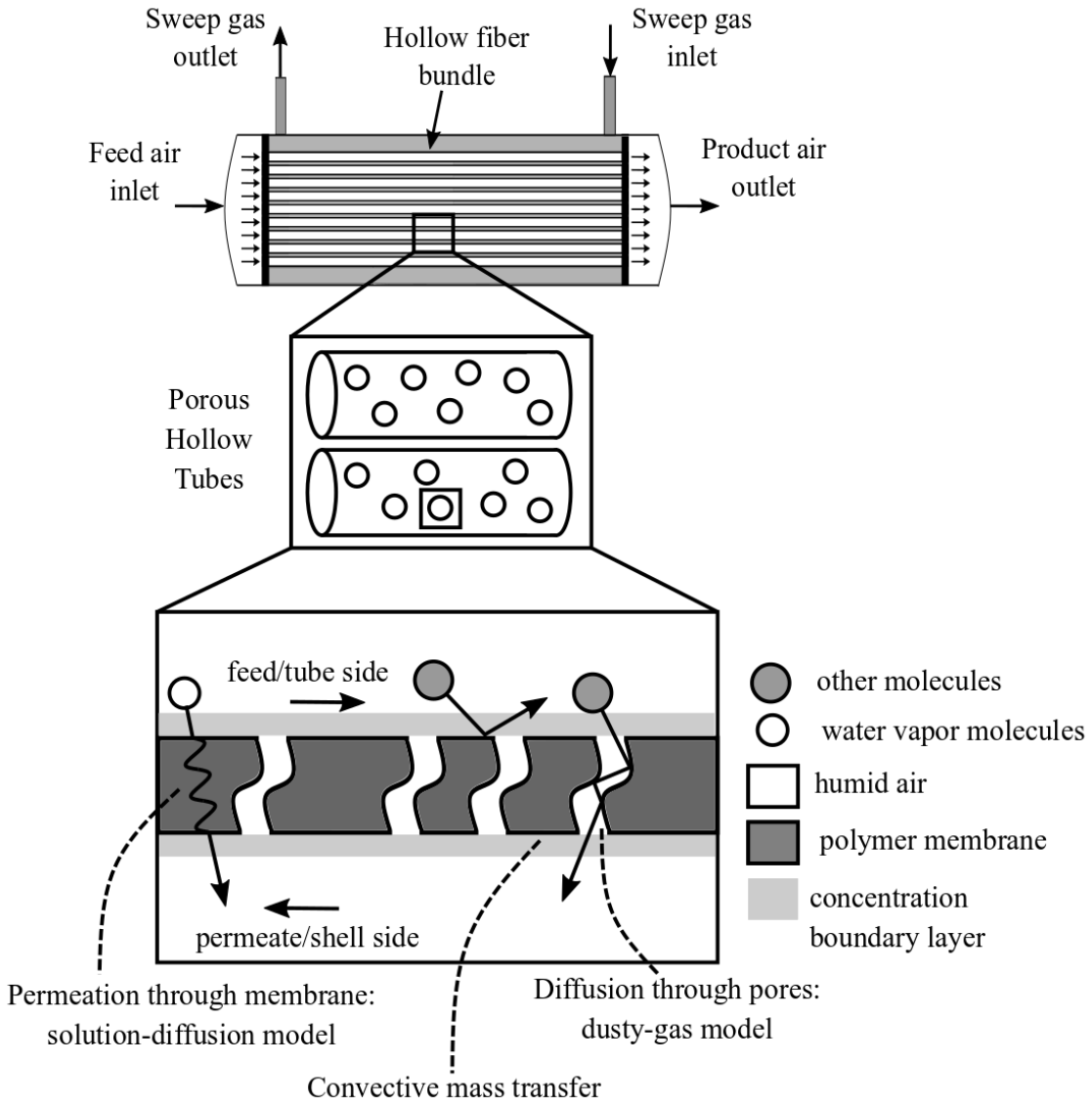

Figure 1.7: Mass transfer mechanisms for a counter-flow shell-and-tube style porous hollow-fiber membrane dehumidifier under high pressure.

ufactured via a multi-step composite coating process [48–50]. The porous polymer fibers are put through a variety of treatments to enhance their dehumidification performance, including a bore-side (interior tube-side) hydrophilic coating to achieve a hollow-fiber tube with a higher permeability for water vapor than for air. Ultimately, water vapor mass transport occurs via permeation through the dense polymer, viscous flow through the pores, and Knudsen flow through very fine pores; of these, permeation through the dense polymer is the dominant mode of transport. Air mass transport occurs via the same three ways, with

viscous flow being the dominant mode [49]. Furthermore, the hydrophilic coating applied to the interior of the membrane tubes is not found to affect the permeation of water vapor, but decreases both viscous pore flow and Knudsen flow of air [49]. The study by Yang et al. further supports this; the membrane tested had a high selectivity for water vapor over nitrogen, yielding negligible air transfer of 1.3×10^{-4} kg/h at the highest feed pressure [41]. Hence, for the membrane considered here, air permeation through the membrane is neglected and mass transport for water vapor is represented by permeation through the dense polymer.

1.3.3 Sweep Considerations

A MD system depends on a concentration or partial pressure gradient between to two sides of the membrane to drive the water vapor from the feed air through the membrane to the permeate side. There are three practical approaches to create the required partial vapor pressure difference: feed compression, vacuum pumping, and gas sweep [34]. Both the feed compression and vacuum pump approaches require additional work to drive turbomachinery; feed compression uses a compressor to increase the feed side pressure and vacuum pumping uses a vacuum pump to decrease permeate side pressure. On the other hand, the gas sweep approach uses an inert gas on the permeate side to dilute the flow and sweep away the permeated water vapor. The majority of studies on MD systems utilize vacuum pumping or a combination of vacuum pumping and gas sweep. For this work, gas sweep is chosen due to the availability of sweep air in ACMs, the lack of additional required work, and the fact that the flow rate of an ACM exceeds typical vacuum pump capabilities. Further, by placing the membrane between the compressor and the turbine in an ACM, feed compression is utilized as well to increase the feed side partial pressure without needing to introduce additional turbomachinery. With the sweep approach decided, another consideration in membrane module research and development is the material properties of the hollow fiber membranes themselves.

1.3.4 Some Material Properties of Membranes

To achieve the desired separation, MD modules consist of membrane materials with a high permeability and selectivity for water vapor. Permeability characterizes the ease with which a penetrating gas can move through a material, and can be derived via Darcy's law as:

$$Pe = \frac{Q\tau}{A\Delta p} \tag{1.2}$$

where Q is the flow rate through the material related to the volume under standard conditions (cm^3_{STP}), τ is the membrane thickness (cm), A is the flow area (cm^2), and Δp is the pressure difference across the membrane (cmHg). While there is no standardized unit for permeability, one that is used throughout industry is the barrer, oftentimes defined as:

$$1 \text{ barrer} = 10^{-10} \frac{\text{cm}^3_{\text{STP}} \cdot \text{cm}}{\text{cm}^2 \cdot \text{s} \cdot \text{cmHg}} \tag{1.3}$$

However, it should be noted that alternative barrer units have long been suggested, and care should be taken understand the definition used in a particular context [51, 52]. There are many equivalent quantities for barrer, including:

$$1 \text{ barrer} = 10^{-10} \frac{\text{cm}^3_{\text{STP}} \cdot \text{cm}}{\text{cm}^2 \cdot \text{s} \cdot \text{cmHg}} \tag{1.4}$$

$$= M \times 3.35 \times 10^{-13} \frac{\text{g} \cdot \text{cm}}{\text{cm}^2 \cdot \text{s} \cdot \text{bar}} \tag{1.5}$$

$$= M \times 3.35 \times 10^{-16} \frac{\text{mol} \cdot \text{m}}{\text{m}^2 \cdot \text{s} \cdot \text{Pa}} \tag{1.6}$$

$$= M \times 3.35 \times 10^{-13} \frac{\text{kg} \cdot \text{m}}{\text{m}^2 \cdot \text{s} \cdot \text{Pa}} \tag{1.7}$$

$$\tag{1.8}$$

where M is the molar mass of the permeating gas (g/mol). For common gases in polymers, permeability coefficients can span a range of 10^{-3} to 10^4 barrer or more [43]. Another key quantity is the selectivity, which characterizes a materials ability to preferentially allow some constituents of the feed flow to pass through while retaining others. With a specific gas selected for separation from a flow, the ideal membrane has high permeability and high selectivity. However, there are well-known trade-offs between these permeability

and selectivity that hinder the applicability of membrane technology in many applications [53, 54]. For an in-depth review of membrane separation terminology, applications, and foundational concepts, there are several substantial reference texts [43, 46].

For dehumidification membranes where water vapor is the targeted permeating gas, many materials have been identified with reasonably high permeability and selectivity [52, 55–58]. In recent years, materials with permeabilities of 450,000+ barrer have been demonstrated, with selectivities greater than 10^5 [58]. The challenge facing membrane module manufacturers is consistent fabrication of these materials in sufficiently small hollow fiber form factors to maintain high mass transfer surface area. For the work conducted here, a recently published permeability of $Pe = 1.2 \times 10^{-12}$ kg/m·s·Pa is used for the majority of membrane module studies. A module design study over a range of permeabilities is also conducted to demonstrate the potential benefits of state-of-the-art and future membrane materials. With the fundamentals of ACMs, icing, and MDs established, the mathematical approach for this work is via modeling and simulation using MATLAB® Simulink™/Simscape™.

1.4 Physical Modeling in MATLAB®

Regardless of the modeling environment, physical modeling is a way to mathematically represent and exercise via simulation a system of physics-based components. In MATLAB® Simscape™, custom components are developed in the Simscape™ language and then connected together to form a physical network in Simulink®. There are also many standard components provided in the Simscape® Foundation library, which is organized by physical domain including: electrical, gas, hydraulic, isothermal liquid, magnetic, mechanical, moist air, physical signals, thermal, thermal liquid, and two-phase fluid. The physical network can consist of components from multiple domains so long as each physical circuit is closed, i.e. all inlet, boundary, and reference conditions are appropriately provided and

all components are connected correctly. The physical network approach is distinct from the standard Simulink® modeling approach in that Simscape® connection ports are non-directional (or bi-directional) as compared to the uni-directional nature of Simulink® ports. In this way, MATLAB® Simscape™ allows for representation of systems wherein functional elements (components) interact with each other by exchanging energy through their ports; i.e., conservation can be enforced across the physical network. The number of ports for each component is determined by the number of energy flows it exchanges with other components, and each energy flow is associated with two variables: one through and one across. All of the custom components developed as part of this work belong to the moist air domain. When the models are exercised via simulation, all of the supporting equations are used to set up a system of differential algebraic equations (DAEs). The DAEs are then sorted, simplified, and solved numerically by MATLAB® ordinary differential equation (ODE) solvers so long as the system of equations is full rank [59].

1.4.1 MATLAB® Simscape™ Moist Air Domain

To properly represent the dynamics of ACMs and account for humidity effects, a humid air media model that is valid over relevant pressure and temperature ranges is necessary. Since this work makes use of MATLAB® Simscape™ for physical modeling, the moist air domain within the Simscape® Foundation library is an obvious choice.

In the Moist Air Domain, moist air is represented as a mixture of three constituent components: dry air, water vapor, and trace gas; by default, the trace gas component is carbon dioxide. This representation is done through a series of look up tables for different physical properties for each constituent, and a mixture property function which combines the constituent properties based on specified mass fractions. This moist air model is used by flow ports which dictate the flow into and out of component models. To fully close the moist air model, several variables for a given port are needed to fully define the moist air flowing in a given model. These variables can be divided into two groups - through and

across variables. These variables characterize the energy flow and usually come in pairs, i.e. one across and one through. The values of each through variable have to balance at a node, meaning the flow into and out of branch points is conservative. For the Moist Air Domain, the across variables are pressure, temperature, specific humidity, and trace gas mass fraction, and the through variables are the mass flow rates of the mixture, water vapor, trace gas, and the mixture energy flow rate.

1.5 Specific Aims

Although much work has been done to numerically investigate air cycle machine behavior and performance, investigations into high-pressure membrane dehumidification for aircraft applications are limited. Moreover, the risk of icing in the air cycle flowpath and its effects on performance are often poorly characterized or neglected entirely. Considering this, the main objectives of this work which are addressed in each chapter are:

1. Develop and implement a suitable model for frost growth and densification applicable to desublimation frosting along the walls of sufficiently cool moist air components.

2. Implement, verify, and validate a custom membrane dehumidifier component model, then use it to characterize the design space of membrane modules for aircraft applications and the dehumidification performance under exhaust sweep conditions.

3. Characterize the performance of an air cycle that incorporates a membrane, and compare to a traditional architecture baseline over a range of operational design points.

Chapter 2 details a novel non-restrictive, fully-algebraic analytical solution for frost growth and densification over flat surfaces. Following the derivation, the accuracy of the proposed solution is evaluated compared to flat plate and parallel plate frost thickness databases. Overall, good qualitative and quantitative agreement is found.

Chapter 3 details a series of modeling and simulation studies of a custom membrane dehumidifier component. These studies first explore the optimal design space of membrane dehumidifier modules for aircraft conditions. Then, the performance of the optimal module is evaluated under exhaust sweep conditions.

Chapter 4 defines and exercises a series of air cycle architectures, including a baseline two-wheel and various architectures that incorporate a membrane dehumidifier. For a range of steady-state operating conditions, the cooling capacity is found for each architecture with respect to a common maximum temperature. Further, saturation and thermal control metrics are quantified and discussed.

1.5.1 Novel Contributions

To the best of the author's knowledge, the fully-algebraic, non-restrictive frost growth and densification solution derived and evaluated in Chapter 2 is the first of its kind. All similar such solutions are restrictive, or require the frost surface temperature as an input, a quantity which is difficult to accurately measure and predict. The novel solution proposed here overcomes this, reducing the numerical complexity for predicting frost thickness.

The set of Pareto-optimal high-pressure membrane module designs found in Chapter 3, which are capable of satisfying aircraft design constraints, have not been characterized elsewhere. The general assumption in other works are that multiple modules will be used in parallel, but for practical applications this will quickly become too large and heavy. Moreover, the characterization of membrane dehumidifier performance under exhaust sweep conditions is novel, with other works relying solely on the product air as the sweep source.

The air cycle architectures evaluated in Chapter 4 are novel in and of themselves, with no other work considering exhaust air as sweep or membrane dehumidification in addition to the traditional condensing-based water separation approach. Further, the thermal control scheme used and corresponding performance evaluation is novel, and demonstrates the icing mitigation capability of membrane dehumidification with a practical control scheme.

A Non-Restrictive Solution to Frost Growth and Densification on Flat Surfaces

An approximate analytical solution for frost growth and densification on horizontal flat surfaces is derived. As opposed to other such solutions, the proposed solution uses a generic, power-law frost density expression that does not depend on frost surface temperature, i.e., it is non-restrictive. This yields a new class of non-iterative, fully-algebraic solutions to the problem of frost growth and densification on flat surfaces that are based explicitly on time and heat transfer characteristics. The derived solution is then exercised for three empirical frost density expressions, and its predictive accuracy for each is compared to flat plate and parallel plate frost thickness databases. The proposed solution accurately predicts frost thickness, with 73.2% and 81.5% of the predictions falling within $\pm 20\%$ proportional error bands for the flat and parallel plate geometries respectively. Moreover, the proposed solution is shown to be comparably or more accurate when compared with other predictive methods while often being more straightforward to implement. This is particularly useful in applications that require a non-iterative approach, or those interested in decreasing computational effort in frost predictions.

2.1 Introduction

Frost formation is an engineering problem that affects system performance in a variety of applications. Consequently, it is necessary to be able to predict frost growth in key affected components, such as air-air heat exchangers in aircraft environmental control systems (ECS). For ECS subsystem models, the chosen frost growth and densification method must be applicable to a wide range of operating conditions, and methods that are relatively simple to implement and control are particularly useful.

Throughout the last few decades, a multitude of frost growth and densification models have been proposed. Empirical models are the simplest to understand and implement, but their range of applicability is inherently limited by the range of operating conditions included in the corresponding tests [60]. Models utilizing computational fluid dynamics (CFD) are numerically complex and are capable of most realistically representing the physics of frost growth, especially the early phases; however, their implementation is overly complex for component and subsystem modeling [61]. Analytical models based on heat and mass diffusion are a compromise in terms of fidelity between empirical and CFD-based approaches, and as a result are the most widely applicable.

To mathematically close an analytical approach, empirical formulas for the frost density and thermal conductivity must be introduced; correspondingly, these frost growth models are called semi-empirical [5, 7, 8, 11, 16, 17, 62–66]. In 2016, Leoni et al. compared a number of semi-empirical and empirical approaches to frost thickness and density databases. Overall, they found that several established methods were able to predict at least half of the database within $\pm 20\%$ error bounds. Further, it was more recently demonstrated that an algebraic frost growth model is suitably accurate for predicting frost growth and densification in relevant 3D flow geometries [67]. However, Leoni et al. emphasized the need for a non-restrictive predictive method for frost thickness, i.e., one that does not require frost surface temperature as an input [9]. Such approaches would enable realistic representation of frost growth and densification in modeling languages that do not permit

iteration, e.g. MATLAB® Simscape™.

In this work, a non-restrictive predictive method is derived for frost densities of the form $\rho_f = ct^{\alpha}$. The formulation of the analytical solution proceeds in the next section. Upon its closure, the analytical solution is then computed for 3 selected density expressions and its predictive accuracy for each is compared to appropriate databases. Following this, the accuracy of the proposed solution for frost thickness is compared with other predictive methods.

2.2 Formulation

2.2.1 Modeling Frost Growth and Densification

Following a number of other works in open literature concerning modeling frost growth and densification on flat surfaces, the following general assumptions have been made: (i) heat and mass diffusion within the frost layer are assumed to be one-dimensional and quasi-steady, (ii) frost thickness and air pressure are assumed uniform over the plate length, and (iii) the Lewis analogy for heat and mass transfer applies [5, 6, 17, 63, 68–73]. Thus, assuming that frost accretion results in a layer of porous solid ice, Fig. 2.1 shows the control volume geometry for the mathematical problem under consideration, with moist air characterized by its temperature, humidity ratio, and velocity flowing over a chilled plate at a uniform surface temperature. The water vapor deposited can either increase the layer thickness, or diffuse into the porous frost and increase the density. From Fig. 2.1, the mass balance in the frost layer can be formulated as:

$$j_x = \frac{\dot{m}}{A} = \frac{d}{dt}\int_0^{x_s} \rho(x)dx \tag{2.1}$$

Defining a space-averaged frost density as:

$$\rho_f = \frac{1}{x_s}\int_0^{x_s} \rho(x)dx \tag{2.2}$$

allows (2.1) to be written in terms of two mass fluxes as:

$$j_x = \rho_f \frac{dx_s}{dt} + x_s \frac{d\rho_f}{dt} = \frac{\dot{m}_{x_s}}{A} + \frac{\dot{m}_{\rho f}}{A} \tag{2.3}$$

where $\dot{m}_{x_s}$ (kg/s) is deposited, increasing the frost thickness, and $\dot{m}_{\rho f}$ (kg/s) diffuses, increasing the frost density.

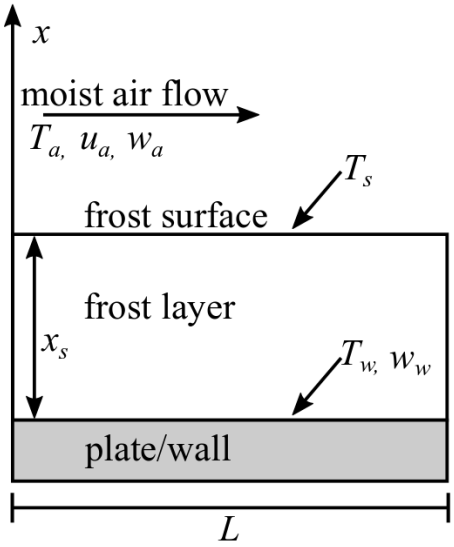

Figure 2.1: Control volume geometry for frost formation over a flat horizontal surface (adapted from [5, 6]).

The total mass flux of water vapor normal to the surface, j_x (kg/m^{2}s), can be determined from the analogy between heat and mass transfer. Further, the Chilton-Colburn analogy for air-water vapor mixtures, called the Lewis relation, gives the relationship between the heat and mass transfer coefficients [74]. Beyond the overall mass balance, the mass and energy balances within the frost layer are used to determine the humidity ratio and temperature profiles. The humidity ratio profile, or concentration of water vapor, is found from combining Fick's law of diffusion with the water vapor mass balance. The temperature profile is determined from Fourier's law combined with the water vapor energy balance. Each of these ordinary differential equations (ODEs) can be solved by applying Cauchy boundary conditions, assuming both the plate and frost surface are saturated. The details of this heat and mass balance approach are shown by Hermes et al. [6].

In 2012, Hermes further simplified this approach by assuming that the temperature profiles in the frost layer are approximately linear [5]. Then, key dimensionless quantities were defined as:

$$\text{non-dimensional time:} \quad \tau = \frac{k_f t}{\rho_f c_p L^2} \tag{2.4}$$

$$\text{non-dimensional frost thickness:} \quad X = \frac{x_s}{L} \tag{2.5}$$

$$\text{non-dimensional temperature:} \quad \theta = \frac{T_s - T_w}{T_a - T_s} \equiv Bi\left(1 + \frac{1}{Ja}\right) \equiv Nu_L \frac{k}{k_f}\left(1 + \frac{1}{Ja}\right) X \tag{2.6}$$

$$\text{Jakob number:} \quad Ja = \frac{c_p(T_a - T_w)}{L_{sv}(w_a - w_w)} \tag{2.7}$$

where L_{sv} = 2,838 kJ/kg. The final key assumption is a frost thermal conductivity of the form $k_f = k_{f0} + \beta\rho_f$ with $\beta << 1$ such that $k_f \approx k_{f0}$. Altogether, an ODE describing frost growth over time can be found from substitution and simplification as:

$$dX + \left(X - \frac{Nu_L}{\tilde{k}} \frac{\tilde{w}\tau}{1+\theta}\right) \frac{d\rho_f}{\rho_f} = \frac{Nu_L}{\tilde{k}} \frac{\tilde{w}}{1+\theta} d\tau \tag{2.8}$$

The details of the derivation are shown by Hermes [5]. At this point, a frost density expression must be imposed to close the problem. For his analytical solution, Hermes chose a frost density that is dependent on the frost surface temperature, which in turn is ultimately dependent on the frost density. Hence, the resultant analytical solution necessitates an iterative approach to resolve the frost layer thickness and its characteristics. The current work deviates at this point, instead choosing a frost density that is independent of the frost surface temperature of the form $\rho_f = ct^{\alpha}$.

For mathematical convenience, c is shown as a generic constant; in frost density expressions from literature, c can be proportionally dependent on a number of flow variables including the humidity and temperature of the air/surface, saturation conditions, and non-dimensional parameters of the flow (e.g., Reynolds and Fourier numbers), and other relevant quantities such as the the density of ice. The exact form of c depends on the modeling approach taken, i.e. semi-empirical or fully empirical. For the work here, frost density ex-

pressions will be selected such that for a given steady-state flow situation c is independent of time. Theoretical models for frost growth assume that frost is a uniform porous media consisting of column-shaped ice crystals; hence, for $t = 0$, ice nuclei have not yet begun to grow columnar dendrites to form the porous structure, so the porosity of the frost is 1 [8]. At this limit, the density of the frost would be equal to the density of the air. In general, analytical models for frost thickness and frost density take the form of $x_s \propto t^{\gamma}$ and $\rho_f \propto t^{\alpha}$, with $\alpha = \gamma = 0.5$ for semi-empirical models and $0.25 \leq \alpha \leq 0.35$ and $0.55 \leq \gamma \leq 0.75$ for empirical correlations [7].

2.2.2 Proposed Analytical Solution for Frost Thickness

For closure, consider a generic power-law frost density expression of the form:

$$\rho_f = ct^{\alpha} \tag{2.9}$$

where $t > 0$ is the elapsed time of frost growth. Differentiating with respect to time and converting to non-dimensional quantities, it follows that:

$$\frac{d\rho_f}{\rho_f} = \frac{\alpha}{1-\alpha}\frac{d\tau}{\tau} \tag{2.10}$$

Now, conducting a scale analysis [5, 66, 75] shows that $X \sim \sqrt{\tau}$, so $d\tau \sim 2XdX$ and thus (2.10) becomes

$$\frac{d\rho_f}{\rho_f} = \frac{\alpha}{1-\alpha}\frac{d\tau}{\tau} = \frac{2\alpha}{1-\alpha}\frac{dX}{X} \tag{2.11}$$

Substituting (2.11) into (2.8), the following first-order nonlinear ODE for the growth of non-dimensional frost thickness over non-dimensional time is found as:

$$\frac{dX}{d\tau} = \frac{Nu_L\tilde{w}}{\left(1+\left(\frac{2\alpha}{1-\alpha}\right)\right)\tilde{k}(1+\theta) - \left(\frac{2\alpha}{1-\alpha}\right)Nu_L\tilde{w}\left(\frac{\tau}{X}\right)} \tag{2.12}$$

Defining the following constants:

$$b_0 = \frac{Nu_L\tilde{w}}{\tilde{k}}$$
$$b_1 = 1 + \frac{2\alpha}{1-\alpha}$$
$$b_2 = \frac{Nu_L\tilde{w}}{\tilde{k}}\left(\frac{2\alpha}{1-\alpha}\right)$$
$$b_3 = \frac{Nu_L}{\tilde{k}}\left(1 + \frac{1}{Ja}\right)$$

and recalling the definition of θ, equation (2.12) can be rewritten as:

$$\frac{dX}{d\tau} = \frac{b_0}{b_1(1+b_3X) - b_2\left(\frac{\tau}{X}\right)} \tag{2.13}$$

To solve this, the first step is to rewrite (2.13) as:

$$\frac{dX}{d\tau}(b_1X + b_1b_3X^2 - b_2\tau) - b_0X = 0 \tag{2.14}$$

Now, let $m(X,\tau) = -b_0X$ and $n(X,\tau) = b_1X + b_1b_3X^2 - b_2\tau$. Then, (2.14) becomes:

$$\frac{dX}{d\tau}n(X,\tau) + m(X,\tau) = 0 \tag{2.15}$$

This is the general form of an exact ODE, a class of differential equations that have a well-established analytical solution method [76]; however, equation (2.15) is not an exact differential equation since $\frac{\partial m}{\partial X} \neq \frac{\partial n}{\partial \tau}$. However, some equations that are not exact can be multiplied by some factor, μ, called an integrating factor, to make the partial derivatives of interest equal and thus make the equation exact. For equation (2.15), it is indeed possible to find an integration factor $\mu(X)$ such that:

$$\frac{dX}{d\tau}\mu(X)n(X,\tau) - \mu(X)m(X,\tau) = 0 \tag{2.16}$$

For this to be true, the partial derivatives must satisfy:

$$\frac{\partial}{\partial X}\left(\mu(X)m(X,\tau)\right) = \frac{\partial}{\partial \tau}\left(\mu(X)n(X,\tau)\right) \tag{2.17}$$

Taking the derivatives for $m(X,\tau)$ and $n(X,\tau)$, a separable ODE can be found as:

$$\frac{\partial \mu}{\partial X}\left(\frac{b_0}{(b_2-b_0)\mu(X)}\right) = \frac{1}{X} \tag{2.18}$$

Integrating both sides and solving for $\mu(X)$ gives:

$$\mu(X) = c_1 X^{\left(\frac{b_2}{b_0}-1\right)} \tag{2.19}$$

where c_1 is a generic constant of integration. Then, with $M(X,\tau) = \mu(X)m(X,\tau)$ and $N(X,\tau) = \mu(X)n(X,\tau)$, the equation is exact since:

$$\frac{\partial M}{\partial X} = -c_1 b_2 X^{\left(\frac{b_2}{b_0}-1\right)} = \frac{\partial N}{\partial \tau} \tag{2.20}$$

So, the exact equation $M(X,\tau) + \frac{dX}{d\tau}N(X,\tau) = 0$ can be solved via the traditional approach [76], then simplified by imposing the initial condition $X(\tau = 0) = 0$ which ultimately yields:

$$\frac{b_1 X(b_3(b_0+b_2)X + 2b_0 + b_2)}{(b_0+b_2)(2b_0+b_2)} - \tau = 0 \tag{2.21}$$

Rewriting shows the quadratic form as:

$$b_1 b_3 X^2 + X\left(\frac{b_1(2b_0+b_2)}{(b_0+b_2)}\right) - \tau(2b_0+b_2) = 0 \tag{2.22}$$

Taking the positive root, the solution is:

$$X(\tau) = \frac{-b_1\left(2 - \frac{b_2}{b_0+b_2}\right) + \sqrt{b_1^2\left(2-\frac{b_2}{b_0+b_2}\right)^2 + 4b_1 b_3(2b_0+b_2)\tau}}{2b_1 b_3} \tag{2.23}$$

Which is written in the classical quadratic equation form as:

$$X(\tau) = \frac{-a_1 + \sqrt{a_1^2 - 4a_0 a_2}}{2a_0} \tag{2.24}$$

where

$$\begin{aligned} a_0 &= b_1 b_3 \\ a_1 &= b_1\left(2 - \frac{b_2}{b_0+b_2}\right) \\ a_2 &= -\tau(2b_0+b_2) \end{aligned}$$

The growth of non-dimensional frost thickness as a function of the square root of non-dimensional time is consistent with diffusive dominant mass transfer processes, such as

frost growth [5, 66]. It is also consistent that the constant of proportionality depends on key frost growth parameters, including the supersaturation degree, thermal conductivity ratio, Jakob number, Nusselt number, and non-dimensional time [5,6]. Another interesting feature of this solution is that it depends on the exponent of time in the chosen density expression; the three selected frost density expressions studied in the next section have different time exponents, with two empirical correlations ($0.25 \leq \alpha \leq 0.35$) and the other a semi-empirical model (α = 0.5).

2.2.3 Model Closure

For the general class of solutions derived, specific expressions must be chosen for the frost thermal conductivity, Nusselt number correlation, and frost density. For the results presented here, the frost thermal conductivity chosen is given by Lee et al. [17] as:

$$k_f = 0.132 + 3.13 \times 10^{-4} \rho_f \tag{2.25}$$

where the second-order term is neglected due to its negligible influence on the results [5]. The Nusselt number correlation chosen is applicable for a flat plate held at a uniform temperature in a fluid flow with $Re_L < 3 \times 10^7$ [77], and defined as:

$$Nu_L = 0.037 Re_L^{0.8} Pr^{0.43} \tag{2.26}$$

The final piece of closing information is the frost density. The solution derived is valid for generic power-law frost density expressions of the form: $\rho_f = ct^\alpha$. As the derived solution is generic, a comparison of its predictive accuracy for different density expressions must be conducted; three such expressions are chosen as shown in Table 2.1 [8–10].

2.2.4 Frost Surface Temperature

To overcome the frost surface temperature input restriction posed by other frost thickness predictive methods, a fully-algebraic, non-iterative analytical solution for the frost surface

Authors	Frost Density Expression	α
Yang and Lee (2004)	$\rho_f = 0.000154\rho_{ice} Re_L^{0.351} Fo^{0.311} w_a^{-0.368} \left(\exp\left(\frac{T_a - T_{tp}}{T_a - T_w}\right)\right)^{2.4}$	0.311
Hermes et al. (2014)	$\rho_f = 0.0024\rho_{ice} \left(\frac{c_p(T_{sat,a} - T_w)}{L_{sv}(w_a - w_{sat,w})}\right)^{-3/2} t^{1/2}$	0.5
Leoni et al. (2016)	$\rho_f = 5.47 Re_L^{0.16} \left(\frac{c_p(T_a - T_w)}{L_{sv}(w_a - w_{sat,w})}\right)^{0.29} \left(\frac{w_w}{w_a}\right)^{0.61} t^{0.34}$	0.34

Table 2.1: Power-law frost density expressions selected from literature [8–10].

temperature is found. Recalling the definition of θ as:

$$\theta = \frac{T_s - T_w}{T_a - T_s} \equiv Bi\left(1 + \frac{1}{Ja}\right) \equiv Nu_L \frac{k}{k_f}\left(1 + \frac{1}{Ja}\right) X \tag{2.27}$$

it can be noted that the temperature differences involving the frost surface temperature are functions of $\theta(X)$, T_a, and T_w [5]. From this, Hermes showed that:

$$\frac{T_s - T_w}{T_a - T_w} = \frac{\theta}{1 + \theta}$$
$$\frac{T_a - T_s}{T_a - T_w} = \frac{1}{1 + \theta}$$

Thus, the frost surface temperature follows as:

$$T_s = T_w + (T_a - T_w)\frac{\theta}{1 + \theta} \tag{2.28}$$

Substituting the frost thickness derived in (2.24) and simplifying, the frost surface temperature can be found as:

$$T_s = T_w + (T_a - T_w)\left(\frac{Nu_L \tilde{k}\left(1 + \frac{1}{Ja}\right)\left(\sqrt{a_1^2 - 4a_0 a_2} - a_1\right)}{2a_0 + Nu_L \tilde{k}\left(1 + \frac{1}{Ja}\right)\left(\sqrt{a_1^2 - 4a_0 a_2} - a_1\right)}\right) \tag{2.29}$$

2.3 Databases and Statistical Metrics

For both frost density and frost thickness, the predictive accuracy is judged against respective databases, defined as follows. Each data point corresponds to experimental air temperature, plate temperature, relative humidity, air velocity, and time.

2.3.1 Frost Density Database

To determine the most accurate power-law frost density expression of the three shown in Table 2.1, predicted frost density values are compared to the frost density database shown in Table 2.2. In total, the current work uses a frost density database of 168 data points.

Authors	Number of points	T_a [° C]	T_w [° C]	RH [%]	u_a [m/s]
Hayashi et al. (1977)	58	25	[-19, -5]	38	[2, 6]
O'Neal and Tree (1984)	6	6	-5	70	[1.3, 4.5]
Lee et al. (2003)	21	[5, 15]	[-20, -15]	[60, 70]	[1.0, 2.5]
Hermes et al. (2009)	52	[16, 22]	[-16, -4]	[50, 80]	0.7
Wang et al. (2012)	15	[-8, 19]	[-16, -8]	[42, 80]	5
Kandula (2014)	3	22.1	-9.3	72	1.8
Nascimento et al. (2015)	13	[2.5, 15.9]	[-10.3, -24.8]	[65, 75]	[0.9, 1.9]
Total:	**168**	**[-8, 25]**	**[-20, -4]**	**[38, 80]**	**[0.7, 6]**

Table 2.2: Experimental parameter range for each author's contribution to flat plate frost density database [6, 8, 11–15].

2.3.2 Frost Thickness Database: Flat Plate

To validate the proposed solution and compare its accuracy with other predictive methods, a database of empirical frost thickness measurements was assembled. The sources and range of experimental parameters for the frost thickness database is detailed in Table 2.3. In total, the current work uses an average frost thickness database of 1141 data points. For later comparisons of the proposed frost thickness solution against other predictive methods, the findings of Leoni et al. are used directly. In these cases, the proposed solution is calculated only over the 382 data points shown in Table 1 of their review [9]. This data is a subset of the flat plate database detailed in Table 2.3.

Authors	Number of points	T_a [° C]	T_w [° C]	RH [%]	u_a [m/s]
Yonko and Sepsy (1967)	74	[21, 23]	[-28, -8]	[57, 80]	[0.27, 2.96]
Jones and Parker (1975)	21	[22, 25]	[-30, -8]	[38, 66]	[1.19, 2.96]
Lee et al. (1997)	40	25	[-30, -8]	[26, 38]	[0.18, 5.0]
Lee et al. (2003)	21	[5, 15]	[-20, -15]	[60, 70]	[1.0, 2.5]
Hermes et al. (2009)	125	[16, 22]	[-16, -4]	[50, 80]	[0.7, 1.0]
Cai et al. (2011)	6	15	-10	65	0.25
Wang et al. (2012)	90	[-8, 19]	[-16, -8]	[42, 80]	[2.22, 5.0]
Kandula (2014)	5	22.1	-9.1	72	1.77
Hermes et al. (2019)	759	[5, 16]	[-20, -10]	80	[0.97, 1.94]
Total:	**1141**	**[-8, 25]**	**[-30, -4]**	**[38, 80]**	**[0.18, 5.0]**

Table 2.3: Experimental parameter range for each author's contribution to flat plate frost thickness database [6, 7, 11–13, 16–19].

2.3.3 Frost Thickness Database: Parallel Flat Plates

Following the same approach as for the flat plate case, data points for frost growth on parallel plate geometries were assembled. The sources and range of experimental parameters for parallel flat plate frost thickness are detailed in Table 2.4. In total, the current work uses an average parallel plate frost thickness database of 124 data points. For later comparisons of the proposed frost thickness solution against other predictive methods for parallel plates, the findings of Leoni et al. are used directly. In these cases, the proposed solution is calculated only over the 24 Ostin and Andersson (1991) parallel plate frost thickness data points [9, 20]. This data is a subset of the parallel plate database detailed in Table 2.4.

Authors	Number of points	T_a [° C]	T_w [° C]	RH [%]	u_a [m/s]
O'neal and Tree (1984)	100	[6, 12]	[-12, -5]	[60, 80]	[1.31, 4.51]
Ostin and Andersson (1991)	24	[20, 21]	[-20, -7]	[31, 72]	3
Total:	**124**	**[6, 21]**	**[-20, -5]**	**[31, 80]**	**[1.31, 4.51]**

Table 2.4: Experimental parameter range for each author's contribution to parallel flat plate frost thickness database [15, 20].

2.3.4 Statistical Metrics

To quantify the predictive accuracy of calculated frost density and frost thickness values, the percent of points within the $\pm 20\%$ error bands (PERC), the mean absolute percentage error (MAPE), and the logarithm of the accuracy ratio (lnQ) are found for the corresponding experimental and predicted values. The percentage of points within proportional error bands was found by a simple accounting, and is a useful but incomplete measure for model performance. To better reflect the predictive performance at small experimental values, the MAPE was found following the traditional definition:

$$\text{MAPE} = \frac{100}{N} \sum \left| \frac{x_{measured} - x_{calculated}}{x_{measured}} \right| \tag{2.30}$$

where N is the number of data points and x is a placeholder variable; for the comparisons here, this was either frost density, ρ_f, or frost thickness, x_s. The MAPE has been reported as the most common measure of predictive accuracy for model selection; however, it has a known bias in favor of models which under-predict due to its asymmetry with respect to positive and negative errors [78]. Taking this into consideration, the sum of the squared logarithm of the accuracy ratio, denoted $\sum(\text{lnQ})^2$, was used to compare the prediction results as well, where the logarithm of the accuracy ratio is defined as:

$$\text{lnQ} = \ln \left(\frac{x_{calculated}}{x_{measured}} \right) \tag{2.31}$$

For strictly positive data sets, such as frost thickness, the measure lnQ and summary statistic $\sum(\text{lnQ})^2$ has been shown to be superior to MAPE as a measure of relative prediction accuracy [78]. When evaluating the accuracy of the proposed solution compared to other predictive methods, the mean absolute error (MAE) and mean relative error (MRE) are found as well to enable direct comparisons the findings of Leoni et al. As they each report different information, the collection of measures are used to judge predictive performance with the best performance indicated in bold for each metric.

2.4 Power-law Frost Density Comparison

2.4.1 Frost Density Predictive Accuracy

For all of the data points in the frost density database, the proposed solution is calculated for each of the 3 chosen density expressions. Figure 2.2 shows the predicted, or calculated, frost density values against the measured, or experimental, frost density values with a line of perfect agreement and $\pm 20\%$ proportional error bars. From this, it is clear that for each density expression a fair number of points fall within the error bands. More specifically, the Yang and Lee (2004) and Hermes et al. (2014) densities seem to more consistently under-predict the frost thickness, where the Leoni et al. (2016) density results in a wider spread of predictions. This absolute comparison is meant to highlight the inherent error of the semi-empirical/empirical frost density expressions chosen. As the frost densities themselves have errors when compared with experimental data, these errors will propagate in the frost thickness calculations.

The statistical metrics defined in the previous section are shown for each density expression compared to the frost density database in Table 2.5. Each statistical metric indicates that the Yang and Lee density expression has the best predictive capability for the defined frost density database. While the Yang and Lee density is indicated to have the highest predictive accuracy for frost density, the other density expressions are quite similar. Moreover, the comparison here evaluates frost density when, ultimately, the proposed solution calculates frost thickness and will be compared against frost thickness databases. Hence, for completeness, the predictive accuracy of the proposed solution for frost thickness will be compared for each of the density expressions as well.

Predictive Method	PERC [%]	MAPE [%]	$\sum(\text{lnQ})^2$ [1]
Proposed solution, Yang and Lee (2004)	**70.8**	**29.3**	**34.3**
Proposed solution, Hermes et al. (2014)	61.3	37.7	98.7
Proposed solution, Leoni et al. (2016)	69.0	44.2	44.9

Table 2.5: Quantitative comparison of predicted frost density compared to database for selected expressions.

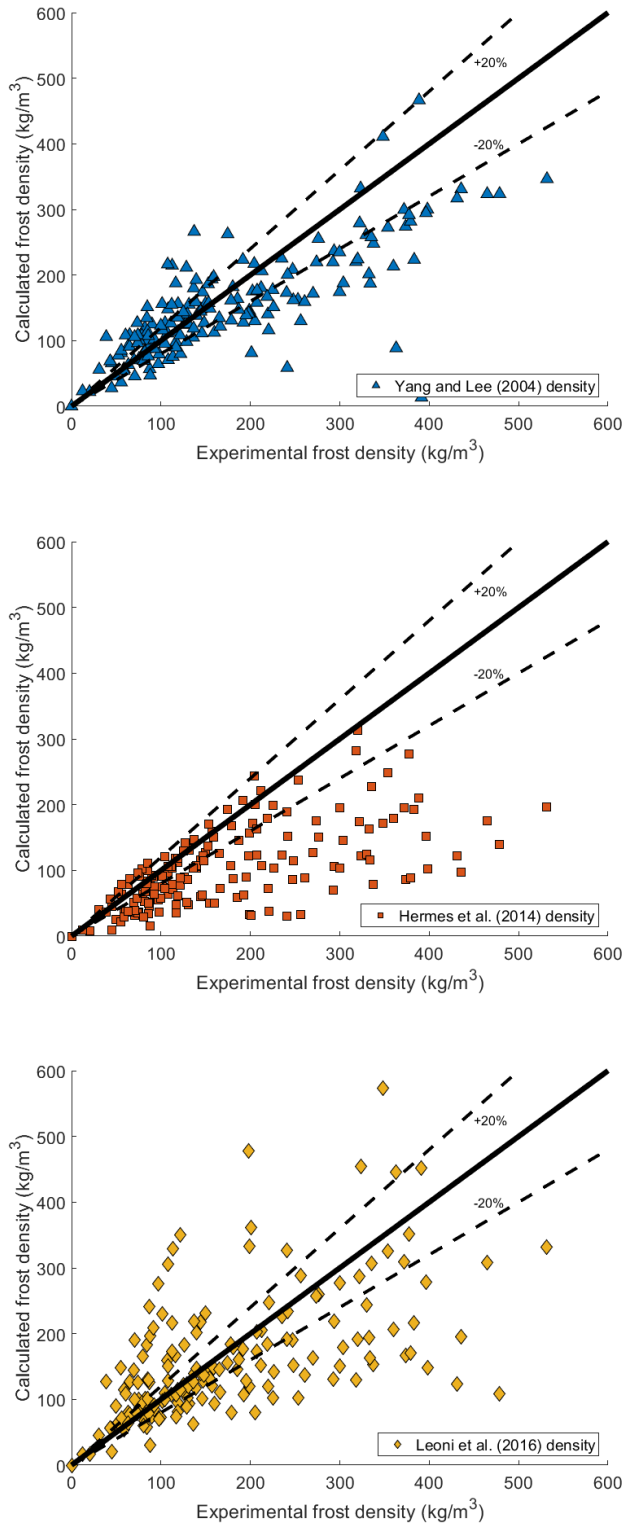

Figure 2.2: Selected frost density expressions compared to database, with line of perfect agreement and $\pm 20\%$ error bars.

2.4.2 Frost Thickness Predictive Accuracy: Flat Plate

Figure 2.3 shows frost thickness predictions for all three density expressions using the proposed solution against the flat plate frost thickness database, with a line of perfect agreement and $\pm 20\%$ proportional errors bands. From this plot, it is clear that all three density expressions lead to overestimated frost thickness values. Moreover, it seems the predicted values have an increased spread as the frost thickness increases. This heteroscedasticity is most extreme when the Leoni density is used, and seems to be lesser so for the Yang and Lee and Hermes et al. expressions. This follows the absolute comparison of the respective densities; since each density expression tends to under-predict frost density, the frost thickness should be over-predicted since a less dense frost layer is thicker.

Table 2.6 shows the previously defined statistical metrics for the predicted frost thickness values using each frost density expression. From Table 2.6, all three of the chosen measures indicate that the Yang and Lee density expression yields the most accurate frost thickness predictions. Further, it can be concluded that, over the selected databases, the most accurate frost density expression also yields the most accurate frost thickness predictions. A similar analysis follows for the proposed solution compared to experimental data for the parallel flat plate database.

Predictive Method	PERC [%]	MAPE [%]	$\sum(\text{lnQ})^2$ [1]
Proposed solution, Yang and Lee (2004)	**73.2**	**31.7**	**164.8**
Proposed solution, Hermes et al. (2014)	47.7	53.5	287.7
Proposed solution, Leoni et al. (2016)	44.2	36.6	208.5

Table 2.6: Quantitative comparison of frost thickness predictions over flat plate for selected density expressions.

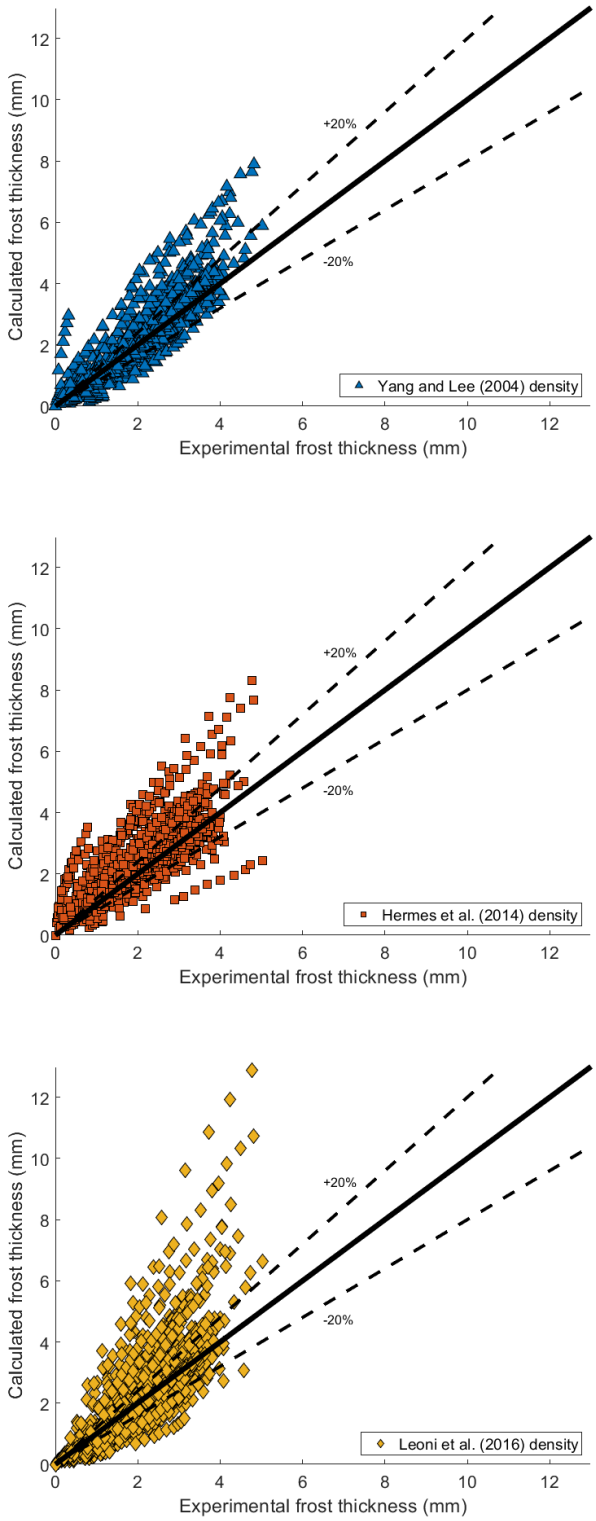

Figure 2.3: Proposed predictive method applied to flat plate frost thickness database calculated using different density expressions, with line of perfect agreement and $\pm 20\%$ error bars shown.

2.4.3 Frost Thickness Predictive Accuracy: Parallel Flat Plates

Figure 2.4 shows the comparison between experimental data and model predictions for all three density expressions for the parallel flat plates database, with a line of perfect agreement and $\pm 20\%$ proportional errors bands. From this plot, it is clear that each density expression overestimates the frost thickness for some experimental conditions, with the most significant deviation from the Hermes density. As was seen for the flat plate database, the predicted values have an increased spread as the frost thickness increases.

Following the same statistical approach as for the flat plate case, Table 2.7 shows the PERC, MAPE, and $\sum(\text{lnQ})^2$ for the three density expressions. As before, each of the chosen measures indicate that the Yang and Lee density expression yields the best predictions. However, the Leoni et al. density performs much better with the parallel plate database and shows comparable statistics for each measure, it just slightly under performs the Yang and Lee density for each. The Hermes et al. density performs worse for the parallel plate database than the flat plate in terms of the PERC and MAPE, indicating the consistent increase in frost thickness over-prediction.

Predictive Method	PERC [%]	MAPE [%]	$\sum(\text{lnQ})^2$ [1]
Proposed solution, Yang and Lee (2004)	**81.5**	**17.4**	**6.55**
Proposed solution, Hermes et al. (2014)	29.8	58.6	30.1
Proposed solution, Leoni et al. (2016)	80.6	20.1	10.4

Table 2.7: Quantitative comparison of frost thickness predictions over parallel plates for selected density expressions.

It has been demonstrated for both frost density and frost thickness against appropriate databases that the proposed solution performs best using the Yang and Lee frost density expression; it will be utilized in all proposed solution calculations henceforth. A series of absolute comparisons showing the predicted frost thickness accuracy for each frost density expression against specific empirical results can be found in Appendix A.

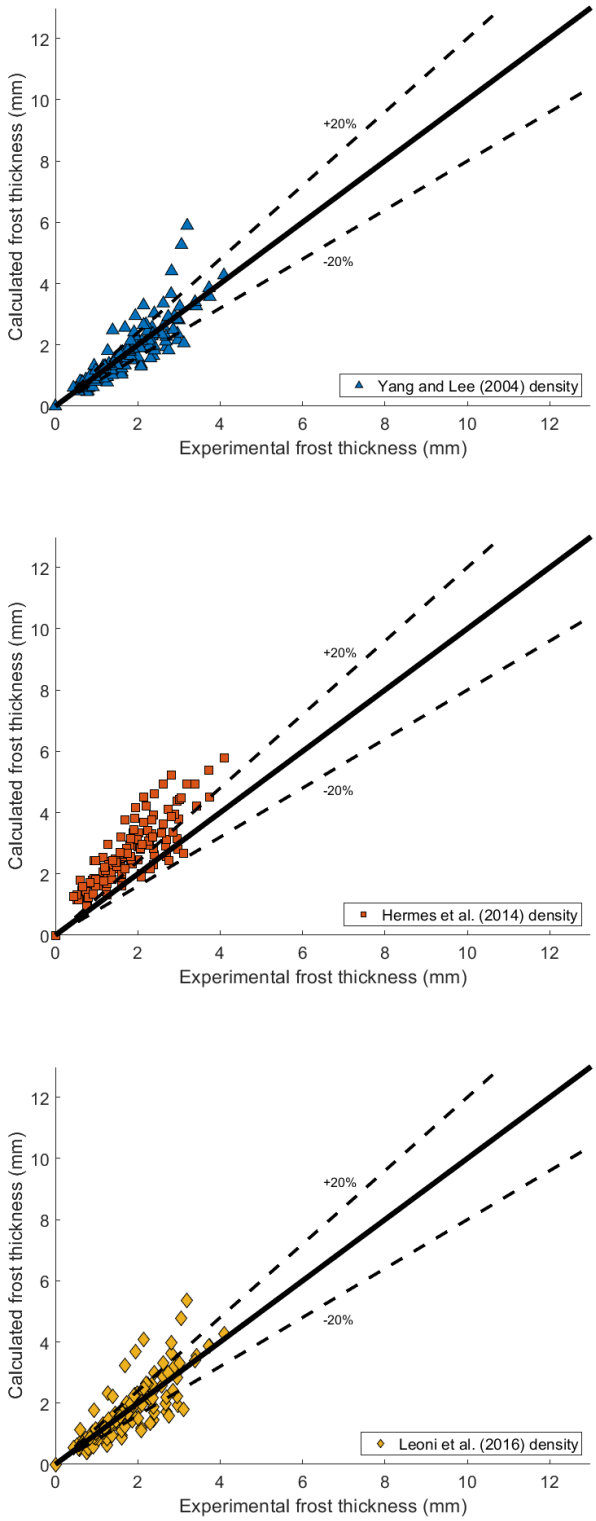

Figure 2.4: Proposed predictive method applied to parallel plate frost thickness database calculated using different density expressions, with line of perfect agreement and $\pm 20\%$ error bars shown.

2.5 Comparison with Other Predictive Methods

2.5.1 Frost Thickness: Flat Plate

For a direct comparison to the findings of Leoni et al., the proposed frost thickness method was exercised over the 382 conditions in their flat plate database and the PERC, MAE, and MRE were computed [9]. Their review found that the frost thickness models developed by Schneider in 1978 and Hermes et al. in 2009 performed best [6, 60]. The results for the proposed solution along with the statistical findings of Leoni et al. are shown in Table 2.8. With respect to the PERC, the proposed solution performs slightly worse than the Hermes et al. (2009) model, which is itself behind the Schneider (1978) correlation. In terms of MAE and MRE, the proposed solution performs better than the other predictive methods. This means that, on average, the proposed solution yields less scattering of results than the Schneider or Hermes approaches, resulting is lower error; however, all can show good agreement for some cases.

Predictive Method	PERC [%]	MAE [%]	MRE [%]
Proposed solution, Yang and Lee (2004)	49.1	**71.6**	**-41.5**
Schneider (1978) correlation	**66.7**	128.6	126.0
Hermes et al. (2009) model	54.9	72.1	64.2

Table 2.8: Results of quantitative comparison of proposed frost thickness with previously established predictive methods for a flat plate.

To look at a more recent, fully-algebraic model for frost growth on a flat plate under forced convection conditions, a comparison is also made to Hermes et al. 2019 4-coefficient model [7]. Since the 4-coefficient model is only valid for supercooling degrees between 12 to 28 K, this was calculated for each experimental run within the flat plate frost thickness database. Of the 122 experimental runs contained within the database, 100 satisfy the supercooling degree requirement with a total of 955 experimental points. Over these 955 test

point conditions, the proposed solution and Hermes 4-coefficient solution were calculated and compared via the established statistical metrics. The results of this comparison are shown in Table 2.9, which indicates that the proposed solution outperforms the Hermes 4-coefficient solution in terms of PERC and MAPE, with both models performing similarly well in terms of $\sum(\text{lnQ})^2$, with a slight lead by the Hermes 4-coefficient model. On average, the proposed solution yields less error, with both the proposed solution and the 4-coefficient model from Hermes et al. displaying similar relative accuracy.

Predictive Method	PERC [%]	MAPE [%]	$\sum(\text{lnQ})^2$ [1]
Proposed solution, Yang and Lee (2004)	**69.3**	**20.5**	0.57
Hermes et al. (2019) 4-coefficient model	42.9	43.5	**0.33**

Table 2.9: Quantitative comparison of proposed frost thickness with previously established fully-algebraic predictive method against cases selected from flat plate frost thickness database.

An absolute comparison is shown in Figure 2.5 over the same 955 points. As before, the proposed solution has a tendency to over-predict the frost thickness but yields good agreement for a large number of points. The 4-coefficient model from Hermes et al. shows more scattered results, as supported by its lower PERC and MAPE. It can be easily demonstrated for some cases that the 4-coefficient model from Hermes et al. is more accurate than the proposed solution, but it does not perform as well over a wide range of operating conditions.

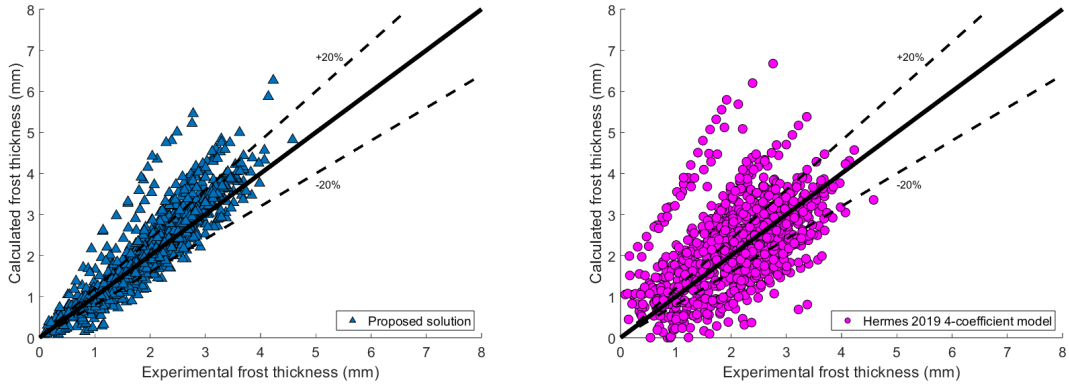

Figure 2.5: Proposed predictive method with Yang and Lee density (left) and Hermes et al. 4-coefficient model [7] (right) applied to flat plate database with appropriate supercooling degree, with line of perfect agreement and $\pm 20\%$ error bars.

2.5.2 Frost Thickness: Parallel Flat Plates

In addition to the flat plate geometry, another commonly considered frost growth and densification flow geometry is parallel flat plates because many internal flow scenarios (e.g., flow in ducts or heat exchanger channel) can be approximated as parallel flat plates. Against the Ostin and Andersson data, it was previously shown by Leoni et al. that the Hermes et al. (2009) and Hermes (2012) correlations showed satisfactory results for predicting frost growth on parallel plates [9, 20]. The proposed frost thickness solution was exercised over the same experimental conditions and the PERC, MAE, and MRE were calculated. The results are shown in Table 2.10, along with the statistical findings of Leoni et al. [9]. The proposed solution performs the best with respect to PERC and MRE, with the Hermes et al. (2009) model leading with respect to MAE. This indicates that the proposed solution is less scattered that the others models on average. Moreover, the MRE being lowest but MAE being highest for the proposed solution reflects its asymmetric tendency to over-predict the frost thickness with an increased skew as frost thickness increases, leading to low relative errors but higher absolute errors. Overall, these results show that the proposed solution performs comparably or more accurately than previously established predictive methods and is well-suited for predicting frost thickness for flat and parallel plate flow geometries.

Predictive Method	PERC [%]	MAE [%]	MRE [%]
Proposed solution, Yang and Lee (2004)	**70.8**	55.3	**-25.8**
Hermes et al. (2009) model	54.2	**29.9**	28.3
Hermes (2012) model	29.2	43.6	40.0

Table 2.10: Quantitative comparison of proposed frost thickness with previously established predictive methods for parallel plates.

2.6 Conclusions

A dimensionless, non-iterative, fully-algebraic expression was derived to find the thickness of a frost layer that grows on horizontal, flat surfaces as a function of key heat transfer characteristics. The derived expression depends on key parameters that drive the frost growth and densification process - the supersaturation degree, the Jakob number, the Nusselt number, and the exponent of time in the chosen density expression. The proposed solution was exercised using three selected power-law density expressions from the literature. For each density expression, good agreement was shown between predicted and experimental frost thickness values over a range of operating conditions for both flat plate and parallel flat plate databases. Further, a statistical analysis of the proposed solution shows that it is comparably accurate, or more accurate, than previously established iterative and fully-algebraic solutions.

To the best of the author's knowledge, this is the most straightforward approach to predict frost growth over time on horizontal surfaces over a wide range of operating conditions. It is particularly useful because it is non-restrictive, i.e. it does not require the frost surface temperature as an input as opposed to many other established analytical predictive methods. Moreover, a fully-algebraic expression for the frost surface temperature is derived and can be used to overcome this limitation in other approaches. Given its accuracy, the proposed solution is best suited for mid-fidelity component and system-level modeling applications where iterative approaches are restricted or too computationally inefficient,

such as complex moist air flow scenarios (e.g., heat exchangers) where representation of frost is critical to system performance evaluation. Nevertheless, the proposed model could be readily improved with the introduction of more accurate frost density or frost thermal conductivity expressions, as well as a better fundamental understanding of the range of validity of standard frost growth and densification assumptions.

Multi-objective Optimization of a High-pressure Membrane Dehumidification Module for Aircraft Applications

High-pressure membrane dehumidification is of interest for aircraft environmental control system applications. To enhance the convective mass transfer characteristics of compressed air membrane dehumidifiers, sweep air is used on the shell side to carry away the permeated water vapor. The sweep supply is typically taken from the product air, sacrificing a significant portion of the flow. To avoid this, alternative sources of sweep air are under consideration. For this study, a discretized high-pressure cross-flow membrane dehumidifier component model is implemented and verified under a range of feed temperatures, flow rates, and sweep ratios. Then, the membrane module design space is explored via constrained Monte Carlo simulation over a range of module design parameter, revealing insights into the volumetric efficiency as a function of key design parameters. From this, the Pareto frontier maximizing efficiency and minimizing volume is obtained for a range of membrane permeabilities to highlight the potential benefits that improved materials could provide. Further, a study on the effects of external hot sweep is conducted that shows sweep temperature results in a small increase in dehumidification performance, showing the feasibility of exhaust air as sweep in an air cycle implementation.

3.1 Introduction

Membrane dehumidification (MD) utilizes a selective layer of material which allows some constituents to pass through while retaining others - for air dehumidification, these membranes separate water vapor from a humid air flow, producing relatively dry air. The degree of dryness of the product air depends on the MD performance. Figure 3.1 shows a generic hollow-tube MD module schematic that uses sweep gas to maintain the required partial pressure difference. The interior of the MD contains many tightly packed hollow fibers. The feed gas is supplied to the interior of these tubes, or the tube side of the MD, and water vapor selectively permeates the membrane and then joins the flow on the shell side of the MD. The shell side flow supply is called the sweep air; it is provided to the exterior of the tubes, or the shell side, to enhance convective mass transfer of the permeated water vapor.

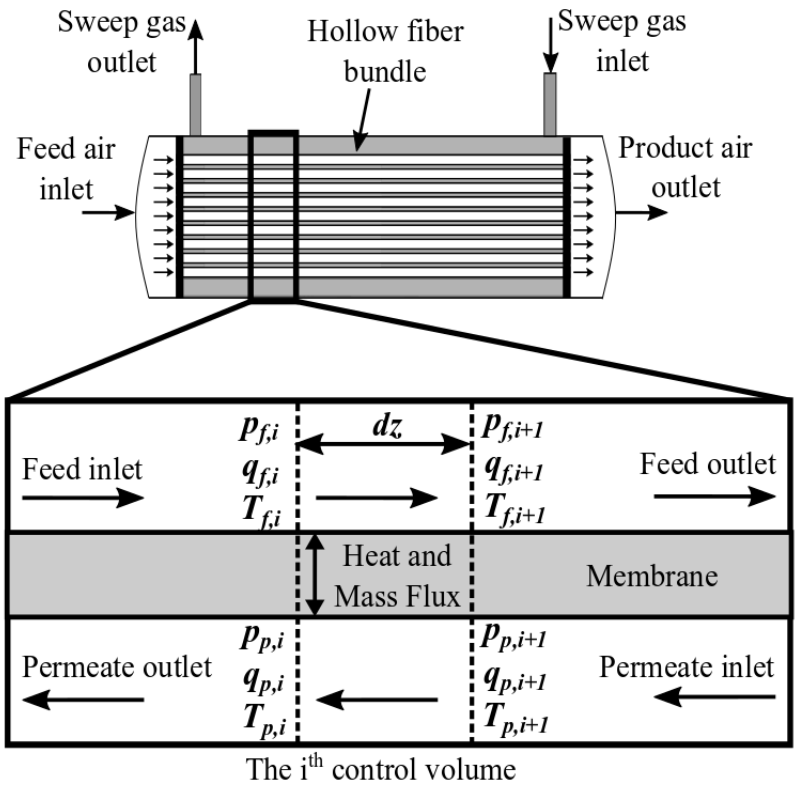

Figure 3.1: Overview of membrane dehumidifier internal structure, with a schematic of the fundamental cross-flow control volume.

Several modeling investigations have been conducted to assess the potential applicability of MD across a wide array of industrial applications, including environmental control for buildings and aircraft [39, 41, 79–85]. Among these, the most common modeling approach is a one-dimensional finite difference scheme; some efforts included two- and three-dimensional computational fluid dynamics simulations, but did not demonstrate significant improvement compared with lower-fidelity approaches [38]. While some investigations have used an electrical circuit analogy of transport resistances to study heat and mass transfer [86], many instead implement empirical models for membrane mass transport [79–83, 87]. However, these empirical models do not represent the material properties or structure of the MD. Other approaches incorporate mass transfer models that are capable of representing several transport mechanisms for diffusion through the membrane, such as Knudsen diffusion, molecular diffusion, and Poiseuille flow [34, 38, 84, 85]. These latter approaches show good agreement with experimental data over a range of operating conditions, and [85] in particular studies the effects of feed velocity, feed humidity, and transmembrane pressure on dehumidification performance. However, this modeling approach has not been used to study the effect of sweep humidity on dehumidification performance as they each assume that a vacuum pump will also be used, or that the sweep will be supplied as some percentage of the product air. Moreover, the local mass transfer progression of high-pressure membrane dehumidifiers has only recently been elucidated [41].

Many aspects of membrane dehumidification for aircraft have been explored by Yang et al. who recently published an experimentally validated membrane model. Post-validation, this model was used to demonstrate the unique local mass transfer characteristics that occur for high-pressure membrane dehumidification. Specifically, the mass transfer process is dictated by a partial pressure difference across the membrane, and this concentration gradient can be maintained even if the sweep side humidity ratio is everywhere higher than the feed side. With this localized understanding, Yang et al. study the effects of varying feed pressure, mass flow rate, and sweep ratio. Then, considering the low design flow rate and

considering the substantially higher flow rate of an aircraft environmental control system (ECS), a number of arrangements of multiple modules are compared, as well as an exergy analysis of membrane-based and traditional condensation-based ECS approaches. From this, the purely parallel arrangement is found to perform best, and a membrane-based ECS is found to have less exergy destruction [41].

This work expands on this previous work. A custom component model following the formulation of Yang et al. is developed, verified, and then characterized under a multitude of conditions relevant to aircraft environmental control. Unlike previous studies, the baseline assumption of this work is that a MD will be incorporated in addition to conventional condensation-based ECS components and will not necessarily be used to replace them. Therefore, the conditions under test are unique to this study. Further, novel extensions are made to the model developed by Yang et al. to study various design aspects of MD modules. In particular, the effect of linearly varying packing fraction, membrane water vapor permeability, and flow orientation are studied. Following this, the dehumidification performance under hot sweep conditions is evaluated. Finally, with aircraft applications in mind, a Monte Carlo study is conducted to reveal the impacts of five key module design parameters on volumetric efficiency.

3.2 Formulation

In membrane dehumidification, water vapor moves from feed side to permeate side across a thin, porous membrane. It has been demonstrated that the mass transfer can be reasonably represented in three steps: (1) convective mass transfer across a concentration boundary layer on the feed side, (2) permeation through the dense membrane, and (3) convective mass transfer across the permeate, or sweep, side concentration boundary layer [41]. Each of these modes will be described as necessary and appropriate models invoked to reach a suitable mathematical formulation.

For a given membrane material, let Pe (s) be the permeability of the membrane with respect to water vapor. Then, under steady mass transfer conditions with a concentration gradient from the feed to permeate sides, the mass flux of the water vapor over a cylindrical membrane can be defined as:

$$j_{m,cyl} = \frac{2Pe(p_{v,fm} - p_{v,pm})}{d_o \ln\left(\frac{d_o}{d_i}\right)} \tag{3.1}$$

where d_o and d_i are the outer and inner diameters of the membrane (m), L is the fiber length (m), p_v is the water vapor partial pressure (Pa), and the subscripts fm and pm denote the air-membrane interfaces of the feed and permeate sides respectively. For an MD module containing N fibers, the total mass flux through the membrane is then:

$$j_m = N j_{m,cyl} = \frac{2Pe(p_{v,fm} - p_{v,pm})}{d_o \ln\left(\frac{d_o}{d_i}\right)} \tag{3.2}$$

Considering the analogous nature of heat and mass transfer, note that the permeability is to permeation for mass transfer as the thermal conductivity is to conduction for heat transfer. Following this, the resistance to permeation mass transfer of the cylindrical membrane is given by:

$$r_m = \frac{\ln\left(\frac{d_o}{d_i}\right)}{2\pi PeL} \tag{3.3}$$

such that $j_m = (p_{v,f} - p_{v,p})/r_m$. Now, for a membrane under a high pressure difference, the air flows on both sides of the membrane form a concentration boundary layer, leading to convective mass transfer as well.

3.2.1 Convective mass transfer

Convective mass transfer is the movement of water vapor due to the flow of moist air on either side of the membrane. For the MD systems under consideration where a sweep side flow will always be utilized, the convective flow effects will occur on both sides of the membrane. Similarly to convective heat transfer, convective mass transfer is dictated by

mass transfer coefficients. From the membrane interface on either side to the bulk flow on that side, there is a concentration gradient that forms a boundary layer along the membrane surface. The mass flux in the boundary layers can be defined as:

$$j_f = k_f(\rho_{v,f} - \rho_{v,fm}) \tag{3.4}$$

$$j_p = k_p(\rho_{v,pm} - \rho_{v,p}) \tag{3.5}$$

where k is the convective mass transfer coefficient (m/s) and ρ is the water vapor density (kg/m^3). From the ideal gas law which gives a relationship between water vapor density and partial pressure, these can alternatively be written as:

$$j_f = \frac{M_v k_f}{RT_f}(p_{v,f} - p_{v,fm}) \tag{3.6}$$

$$j_p = \frac{M_v k_p}{RT_p}(p_{v,pm} - p_{v,p}) \tag{3.7}$$

where R is the gas constant, 8.314 J/(mol K), M_v is the molar mass of water vapor, 0.018 kg/mol, T is the temperature (K), and p_v is the water vapor partial pressure (Pa). The convective mass transfer coefficients on either side can be found as:

$$k = \frac{ShD_{va}}{d_h} \tag{3.8}$$

where d_h is the hydraulic diameter on either side of the membrane (m), Sh is the Sherwood number, and D_{va} is the diffusivity of the water vapor in the air (m^2/s). The diffusivity of water vapor in air can be found as:

$$D_{va} = \frac{C_a T^{1.75}}{p\left(v_v^{1/3} + v_a^{1/3}\right)^2}\sqrt{\frac{1}{M_v} + \frac{1}{M_a}} \tag{3.9}$$

where $C_a = 3.203 \times 10^{-4}$, $v_v = 2.01$, $v_a = 12.7$, and M_a is the molar mass of air, 0.029 kg/mol [88].

At this point, Sherwood number correlations are needed for the feed (tube) and permeate (shell) sides of the MD. On the shell side, correlations developed by Lipnizki and Field taking into account the degree of development of velocity and concentration boundary

layers as well as the packing fraction of the membrane module are used as [89]:

$$Sh_p = (Sh_1^3 + Sh_2^3 + Sh_3^3)^{1/3} \tag{3.10}$$

where

$$Sh_1 = 3.66 + 1.2\phi^{-0.4} \tag{3.11}$$

$$Sh_2 = 1.615\left(1 + 0.14\phi^{-0.25}\right)\left(\frac{ReScd_h}{L}\right)^{0.33} \tag{3.12}$$

$$Sh_3 = \left(\frac{2}{1 + 22Sc}\right)^{0.167}\left(\frac{ReScd_h}{L}\right)^{0.5} \tag{3.13}$$

and ϕ is the packing fraction of the fibers in the shell, L is the fiber length, Re is the Reynolds number, and Sc is the Schmidt number. Further, the Sherwood numbers represent flow development regimes as follows: Sh_1 is the Sherwood number if both the hydrodynamic and concentration profiles are fully developed, Sh_2 for fully hydrodynamically developed flow but still developing concentration profile, and Sh_3 for neither concentration nor hydrodynamic profiles developed. On the tube side, the Sherwood number can be calculated using Huasen's correlation [90] as:

$$Sh_f = 4.36 + \frac{0.023ReSc(d_h/L)}{1 = 0.0012ReSc(d_h/L)} \tag{3.14}$$

where Re is Reynolds number, Sc is the Schmidt number, and L is the membrane length (m); this correlation is applicable for laminar flows with the Graetz number $Gr = ReSc(d_h/L) < 4$. The packing fraction is a measure of how tightly packed hollow tube fibers are packed within the MD as

$$\phi = N\left(\frac{D}{d_o}\right)^2 \tag{3.15}$$

where N is the number of fibers and D is the module shell diameter (m).

3.2.2 Mass transfer

At steady state, the rates of mass transfer (i.e., product of mass flux and area) are equal across the membrane and both boundary layers. In the control volume shown in Figure 3.1, the local mass transfer rate $\dot{m}_v$ for the membrane, feed, and permeate sides is as follows:

$$\dot{m}_v = \frac{2N\pi Pedz(p_{v,fm} - p_{v,pm})}{\ln\left(\frac{d_o}{d_i}\right)} \tag{3.16}$$

$$\dot{m}_v = \frac{N\pi M_v k_f dz}{RT_f}(p_{v,f} - p_{v,fm}) \tag{3.17}$$

$$\dot{m}_v = \frac{N\pi M_v k_p dz}{RT_f}(p_{v,pm} - p_{v,p}) \tag{3.18}$$

where dz is the length of the control volume. Applying the resistance-in-series model [41, 91], the interfacial variables $p_{v,fm}$ and $p_{v,pm}$ drop out, leaving:

$$\dot{m}_v = \frac{p_{v,f} - p_{v,p}}{r} \tag{3.19}$$

where r is the overall mass transfer resistance as:

$$r = \frac{\ln\left(\frac{d_o}{d_i}\right)}{2\pi Pedz} + \frac{RT_f}{N\pi d_i M_v k_f dz} + \frac{RT_p}{N\pi d_o M_v k_p dz} \tag{3.20}$$

3.2.3 Governing equations

Within each control volume, for both the feed and permeate sides, conservation of mass and energy are applied to the volume of moist air. To achieve water vapor transfer from the feed to the sweep side, $\dot{m}_v$ is added to the sweep side and subtracted from the feed side. Similarly for heat transfer, the respective heat flow rates are applied to heat side. Finally, the momentum balance on each side within the control volume is determined by the Darcy-Weisbach equation as:

$$\Delta p_f = \frac{f_f \rho_f u_f^2 dz}{2d_i} \tag{3.21}$$

$$\Delta p_p = \frac{f_p \rho_p u_p^2 dz}{2d_h} \tag{3.22}$$

where f_f, f_p are the respective friction coefficients. For all of the flow rates for the current study, the Reynolds number on both the tube and shell sides are less than 2000. For the flow rates of the study presented here, the Reynolds number fall within laminar ranges. Following Zhang and Huang, the friction factors used for the pressure drops on either side are inversely proportional to the Reynolds numbers as [92]:

$$f_f = \frac{64}{Re_f} \tag{3.23}$$

$$f_p = \frac{41.3}{Re_p} \tag{3.24}$$

3.2.4 Heat transfer

For many of the results shown, the membrane model formulation stops here and there is no exchange of heat; this will be referred to as the isothermal formulation. To study the effects of simultaneous heat and mass exchange, the model taken from Yang et al. is extended to include heat transfer and implemented in a separate, non-isothermal membrane dehumidifier component model [41]. For this non-isothermal formulation, the membrane module is assumed adiabatic with respect to its surroundings.

The heat transfer for the membrane dehumidifier consists of convective heat transfer on both sides of the membrane, as well as conduction through the polymer membrane. The conductive heat transfer coefficient on either side is found as:

$$h_f = \frac{k_f Nu_f}{d_{h,f}} \tag{3.25}$$

$$h_p = \frac{k_p Nu_p}{d_{h,p}} \tag{3.26}$$

where k is the thermal conductivity, Nu is the Nusselt number, and the subscripts f and p denote the feed and permate sides. The Nusselt number can be found using the Chilton-Colburn analogy for heat and mass transfer as [93]:

$$Nu = ShLe^{1/3} \tag{3.27}$$

where $Le = Pr/Sc$ is the Lewis number. With the convective heat transfer coefficients and

the thermal conductivity of the membrane, λ, the total thermal resistance is defined as:

$$r_t = \frac{1}{h_f}\left(\frac{d_o}{d_i}\right) + \frac{2\delta}{\lambda}\left(\frac{d_o}{d_o + d_i}\right) + \frac{1}{h_p} \tag{3.28}$$

where λ is the thermal conductivity of the membrane (W/m·K), and $\delta = d_o - d_i$ is the membrane thickness. Hence, the total heat transfer coefficient is given by $h = 1/r_t$. With this, the effectiveness-NTU approach for a counter-flow heat exchanger can be used to resolve the heat flux.

The effectiveness-NTU method is used to calculate the rate of heat transfer when there is insufficient information to calculate the log-mean temperature difference. The effectiveness is ratio of actual to maximum heat transfer. In a device that exchanges heat, the side with the lesser heat capacity rate will undergo the maximum possible temperature change. So, the number of transfer units of such a device is defined as:

$$NTU = \frac{hA_{ext}}{C_{min}} \tag{3.29}$$

where A_{ext} is the lateral surface area of the exterior of the hollow fiber membrane tubes, and the minimum heat capacity rate is given by $C_{min} = min(\dot{m}_f c_{p,f}, \dot{m}_p c_{p,p})$ where $\dot{m}$ is the mass flow rate (kg/s) and c_p is the specific heat capacity (J/kg·K). Then, the effectiveness for a counter-flow exchanger has a well-established form as:

$$\epsilon = \frac{1 - \exp(-NTU(1 - C_r))}{1 - C_r \exp(-NTU(1 - C_r))} \tag{3.30}$$

where $C_r = C_{min}/C_{max}$ is the ratio of minimum to maximum heat capacity rates. With the effectiveness, the heat flow rates for the feed and permeate sides are given by:

$$Q_f = \epsilon C_{min}(T_{p,in} - T_{f,in}) \tag{3.31}$$

$$Q_p = \epsilon C_{min}(T_{f,in} - T_{p,in}) \tag{3.32}$$

3.2.5 Modeling Approach

In order to represent and analyze the local heat and mass transfer within the high-pressure membrane dehumidifier, the formulated differential models for temperature, specific hu-

midity, and pressure are numerically simulated via MATLAB® Simscape™. The equations themselves are integrated into the source code of a custom membrane dehumidifier component written in the Simscape™ language. The fundamental control volume is shown in Figure 3.1. Given the choice of MATLAB® Simscape™ as the modeling language, the custom component model in the Moist Air domain tracks moist air flow variables for the volume of moist air on the feed (also called tube) and permeate (also called shell) side of the MD. These quantities are found by enforcing conservation of mass and energy for each constituent of the mixture for each side, accounting for the water vapor that moves from the feed side to the permeate side, as well as momentum balance and heat transfer calculations.

For each simulation, the back pressure on the feed side is calculated as formulated over the entire length of the MD, using the feed inlet conditions (temperature, mass flow rate, and pressure). This must be determined a priori for the simulation to be able to execute. Each segment also determines a pressure drop, a contribution to the overall, with the segment length dz. On the sweep side, the back pressure is maintained over all cases at atmospheric pressure, or 101.325 kPa. For all tests run here, a relative error of 1×10^{-3} is used as a convergence criterion for the model solver settings. A detailed verification and validation of the isothermal model formulation can be found in Appendices B and C. For all verification and validation results, the product sweep model shown in Figure 3.3 is exercised.

3.2.6 Dehumidification metrics

For the membrane dehumidifier component, the dehumidification efficiency is defined in terms of the inlet and outlet humidity ratios on the tube side as:

$$\eta_{deh} = \frac{w_{tube,in} - w_{tube,out}}{w_{tube,in}} \tag{3.33}$$

This measure is reported for a variety of operating conditions as part of the component verification in the following section. Another parameter of interest is the dehumidification

rate, also called the moisture removal rate (MRR), defined as the sum of the mass flux along the length of the membrane multiplied by the mass transfer area. Alternatively, this can be defined as the sum of the water vapor mass flow rate along the length of the membrane fibers as:

$$MRR = \sum_{z=0}^{z=L} \dot{m}_v \tag{3.34}$$

3.3 Results and Discussion

With a verified formulation, there are two objectives of this work. First, with aircraft applications in mind, the multi-objective membrane module design space will be explored via Monte Carlo. With the set of Pareto-optimal designs, the designs with the highest efficiency per volume and highest dehumidification efficiency are selected. The local heat and mass transfer characteristics of these modules are characterized, as well as their performance over a range of sweep ratios. Then, the module design best suited for aircraft applications is extended to the adiabatic formulation and evaluated under hot sweep conditions.

3.3.1 Multi-objective Optimization for Membrane Module Design

For aircraft applications, the mass flow rate is substantially higher than the typical design flow rate of commercially available MD modules. Consequently, to feasibly handle high flow rates, multiple modules need to be connected in parallel with independent sweeps, shown to be the most efficient multiple module configuration by Yang et al. [41]. Many industrial use cases of MD modules are not subject to strict volumetric constraints; however, for aircraft applications, the dehumidification efficiency per volume is critical to consider. Hence, the problem under consideration is a bounded and constrained multi-objective optimization problem seeking to minimize module volume, V, and simultaneously maximize module dehumidification efficiency, η_{deh}.

The trade-off of the design space between efficiency and module volume can be char-

acterized via a Pareto frontier considering both objectives simultaneously. A similar investigation was recently conducted using a genetic algorithm used to identify a Pareto efficient set of module parameters [94]. However, the parameter bounds and operating conditions were quite limited, corresponding to current manufacturing capabilities and thus a low flow rate capacity. The same approach is of interest for the design of high capacity, volumetrically efficient high-pressure membrane modules for aircraft applications.

Considering that the dehumidification efficiency is a highly nonlinear function of many flow variables, a Monte Carlo approach is taken to explore the parameter space of this optimization problem. For this, 1000 simulations were run of the isothermal membrane model with product sweep ratio of 20% for a feed flow rate, temperature, pressure, and humidity ratio of 0.5 kg/s, 320K, 575 kPa, and 10 g/kg respectively. Each run used a distinct set of module parameter values, randomly generated using the Mersenne Twister generator in MATLAB®. The randomly generated module parameter values, d_o, d_i, D, ϕ, and L, were bounded and an additional constraint is introduced to ensure that the feed side pressure drop is relatively small. With all of this, the optimization problem can be formally stated as:

$$\begin{aligned}
\underset{d_o,d_i,D,\phi,L}{\text{minimize}} \quad & V = \frac{\pi D^2 L}{2} \\
\underset{d_o,d_i,D,\phi,L}{\text{maximize}} \quad & \eta_{deh} = f(d_o, d_i, D, \phi, L, T_{f/p}, \omega_{f/p}, \mu_{f/p}, \rho_{f/p}) \\
\text{subject to} \quad & 0.5 \leq d_o \leq 2 \text{ mm} \\
& 1.25 \leq \frac{d_o}{d_i} \leq 1.7 \\
& 0.15 \leq D \leq 0.3048 \text{ m} \\
& 0.2 \leq \phi \leq 0.8 \\
& 0.2 \leq L_{eff} \leq 0.75 \text{ m}, L_{eff} = 0.75L \\
& \Delta p_f \equiv \frac{128 \mu L \dot{m}_f d_o^2}{\pi \rho \phi D^2 d_i^2} \left(\frac{d_o}{d_i}\right)^2 \leq 25 \text{ kPa}
\end{aligned} \tag{3.35}$$

For the chosen bounds, the smallest volume that can be achieved is 0.005 m^3. There

is an implicit constraint on the fiber length as a proportion of the total module length - it is assumed that the effective fiber length is 75% of the total module length to account for the length of the headers necessary to transition from the inlet pipe size to the shell diameter. While this quantity varies from module to module, this is a reasonable assumption based on currently available commercial products. Further, the permeability is fixed to 1.2 $\times 10^{-12}$ kg/m·s·Pa for all runs, to represent the capabilities of current membrane materials in production at scale.

For a currently available fiber material with a permeability of 1.2 $\times 10^{-12}$ kg/m·s·Pa, the simulation results for these objectives are shown in Figure 3.2, with the Pareto frontier shown in black. The Pareto frontier is the set of Pareto efficient solutions, indicating the efficient trade-offs that exist between different parameter sets. With a specific desired volume or dehumidification efficiency in mind, the optimal design can be selected from this set. The full set of Pareto-efficient points and their corresponding performance metrics is provided in Appendix D. From the Pareto front, it is clear that volumetrically efficiency module designs for typical aircraft environmental control system (ECS) operating conditions tend toward smaller module lengths with larger diameters, and thus a large increase in the number of fibers in the module. Further, with the sweep ratio fixed at 20%, none of the constrained designs are found to be able to perfectly remove the vapor. However, this could be improved by increasing the sweep ratio, as demonstrated in the following section. The design parameters of the module with the highest volumetric efficiency are shown in Table 3.1.

To evaluate the isothermal membrane model under product sweep conditions, a test model with product sweep was constructed as shown in Figure 3.3. The feed air is supplied at a given flow rate, temperature, pressure, and humidity ratio with a back pressure at the feed outlet, and the sweep outflow is kept at the feed temperature and atmospheric pressure. With the sweep air taken from the product air (or feed outlet), the temperature of the sweep

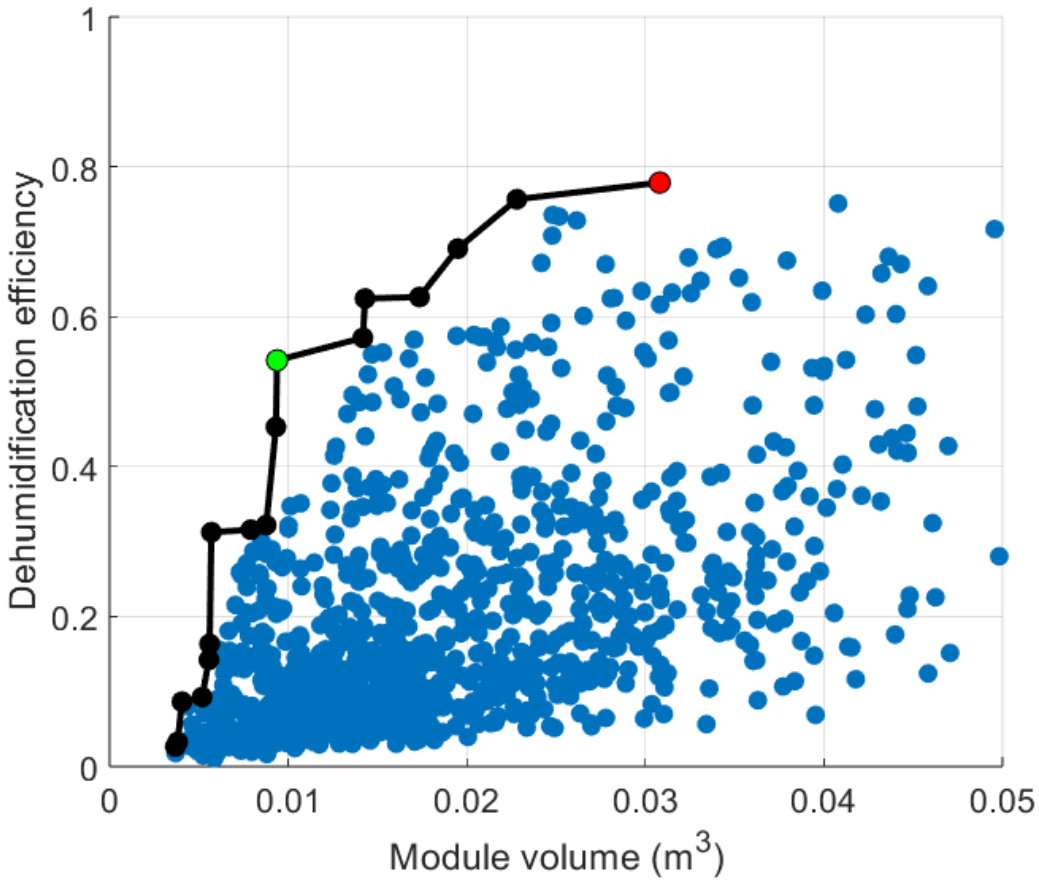

Figure 3.2: Pareto frontier for membrane dehumidifier under aircraft operating conditions, with points of highest efficiency per volume (green) and highest efficiency (red) highlighted.

Parameter	Value	Unit
Fiber outer diameter	0.5603	mm
Fiber inner diameter	0.4326	mm
Shell inner diameter	0.2255	m
Shell packing fraction	0.7597	1
Fiber length	0.2347	m
Module length	0.3129	m

Table 3.1: Geometry of membrane module with highest volumetric efficiency for a fixed permeability of $Pe = 1.2 \times 10^{-12}$ kg/m·s·Pa $\approx$ 200,000 barrer.

is the same as the feed and its humidity is equal to the product humidity. This subsystem will be referred to as the product sweep architecture , as in this model the sweep air is taken from the dry air that the membrane produces. After gathering the multi-objective

optimization results, this model was exercised for the same operating conditions that the optimization was run over: a product sweep ratio of 20% and a feed flow rate, temperature, pressure, and humidity ratio of 0.5 kg/s, 320K, 575 kPa, and 10 g/kg. The membrane geometry was taken to be the most volumetrically efficient design, in order to study its mass transfer characteristics.

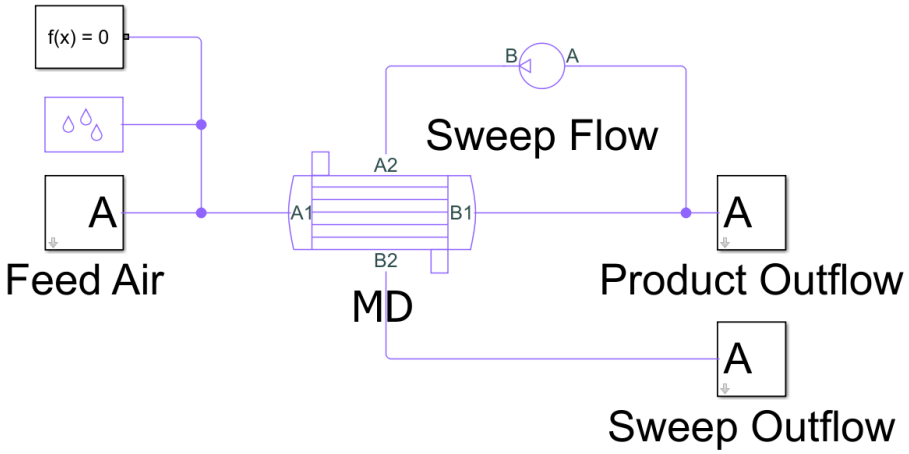

Figure 3.3: Model to evaluate isothermal membrane module under product sweep conditions.

3.3.2 Optimal Module Design: Highest Volumetric Efficiency

The local mass transfer characteristics of the module design with the highest volumetric efficiency is shown in Figure 3.4. Following the trends shown in the various module verification evaluations (see Appendix B), the local mass transfer characteristics behave as expected. Along the length of the membrane module, the feed side flow travels from left to right. As it travels, vapor moves from the feed side to the sweep side, resulting in a reduction of the feed side humidity ratio from 10 g/kg at the inlet to 4.6 g/kg at the feed side outlet. Since this is a counter-flow module with product sweep flow, the sweep air is taken from the feed side outlet; albeit, there is a large pressure drop before it is supplied to the sweep side inlet.

Along the sweep side, which flows right to left along the length of the membrane, the

humidity ratio increases from 4.6 g/kg to 31.6 g/kg as vapor moves across the membrane. Mass transfer is maintained across the length of the membrane despite the fact that the sweep side humidity ratio is everywhere higher than the feed side. This is because a partial pressure difference is maintained along the module length, as shown in the bottom left figure, due to the high pressure of the feed side. This is a unique mass transfer characteristic of high-pressure membrane dehumidification, where the mass transfer is determined by humidity ratio and pressure together; in normal pressure membrane dehumidification, this is determined by humidity ratio only [41]. As expected, the water vapor mass flux across the membrane follows the trend of the partial pressure difference, with the slope decreasing along the membrane length.

To determine if the highest volumetric efficiency design will be able to sufficiently dehumidify the feed air at the chosen operating conditions, the model was exercised with a sweep ratio ranging from 20% to 95%. The results of this are shown in Figure 3.5. From the results, it clear that as sweep ratio increases the additional improvement in dehumidification slows, with similar feed outlet humidity ratios for sweep ratios of 60-95%; this upper bound is set strictly below 100% since using all of the product flow as sweep is impractical, and even in external sweep situations some flow loss is anticipated.

Even with a sweep ratio of 95%, the feed outlet humidity ratio is only reduced to 3.6 g/kg. This corresponds a product air saturation temperature of 268 K which is equivalent to 22.7 °F. While this would result in a subfreezing turbine outlet in an air cycle machine, this is not dry enough to substantially boost the cooling capacity. With this, it seems that while the volumetrically efficient design dehumidifies as expected, it may not be the best suited to determine the potential benefits of a MD for air cycle applications. Instead, the highest efficiency design, which is the point in the Pareto set with the highest volume but also the highest performance, is analyzed.

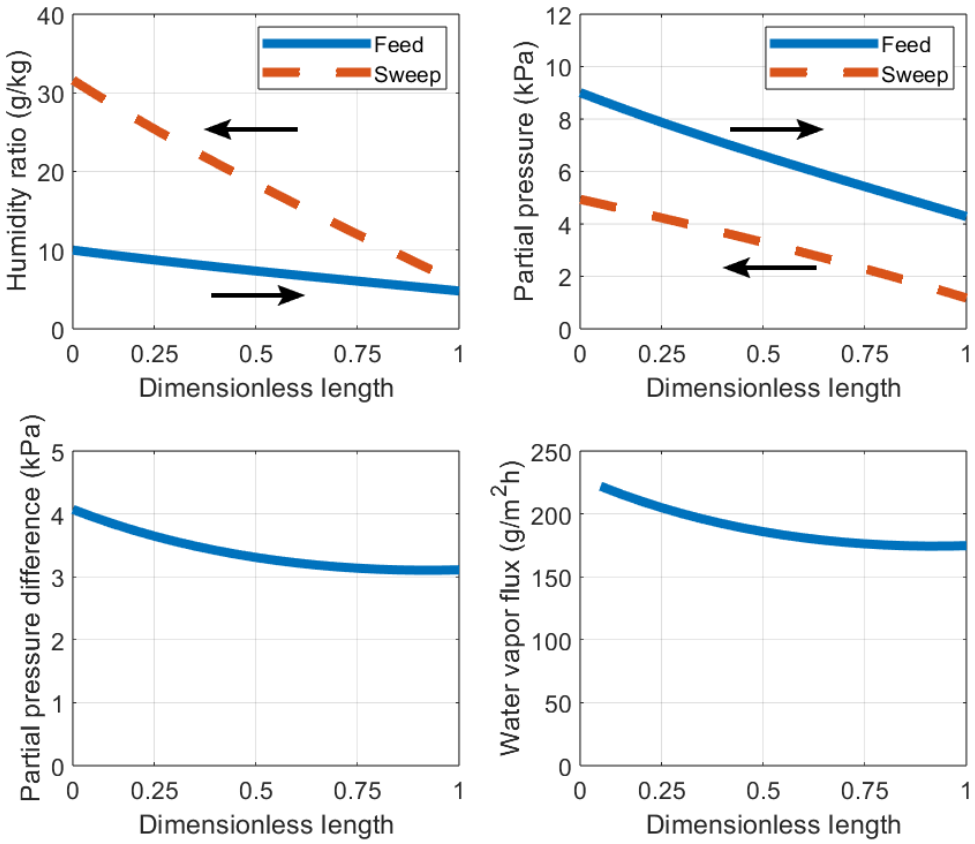

Figure 3.4: Distribution profiles of feed and sweep side humidity ratio (top left), feed and sweep side partial pressure (top right), partial pressure difference (bottom left), and water vapor flux (bottom right) for the volumetrically efficient module design under aircraft relevant conditions with flow direction indicated.

3.3.3 Optimal Module Design: Highest Dehumidification Efficiency

The membrane parameters for the highest dehumidification efficiency module design are shown in Table 3.2. As for the highest volumetric efficiency design, the local mass transfer characteristics and performance over a range of sweep ratios will be evaluated.

The local mass transfer characteristics of the module design with the highest dehumidification efficiency are shown in Figure 3.6, under 20% product sweep conditions. With the increased dehumidification performance, the feed side humidity ratio is now taken from 10 g/kg at the inlet to 2.2 g/kg at the outlet. This is a marked improvement from the 20%

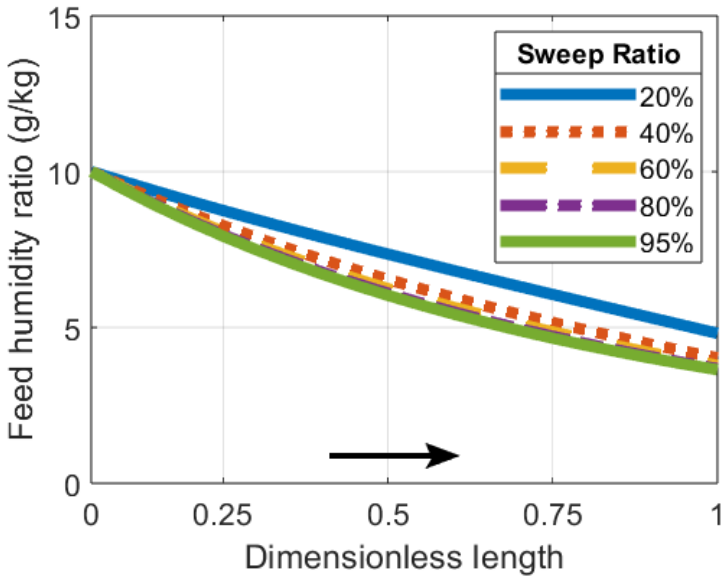

Figure 3.5: Feed side humidity ratio over the volumetrically efficient membrane module for a range of sweep ratios, with flow direction indicated.

Parameter	Value	Unit
Fiber outer diameter	0.5093	mm
Fiber inner diameter	0.4060	mm
Shell inner diameter	0.2516	m
Shell packing fraction	0.4307	1
Fiber length	0.6198	m
Module length	0.8264	m

Table 3.2: Geometry of membrane module with highest dehumidification efficiency for a fixed permeability of $Pe = 1.2 \times 10^{-12}$ kg/m·s·Pa $\approx$ 200,000 barrer.

sweep ratio performance of the volumetrically efficient design. There are a few other features to notice from the local mass transfer results for the maximum efficiency module. First, the sweep side outlet humidity ratio increases to 40.9 g/kg due to increased movement of water vapor from the feed to the sweep sides. This causes the partial pressure of the sweep side to be greater, although still everywhere less than the feed side. The increased sweep side partial pressure leads to a lower partial pressure difference, and therefore lower magnitude flux. However, this module still results in better dehumidification performance than the volumetrically efficient design considering the increased efficiency and increased dehumidification rate of 13.91 kg/h compared to 9.70 kg/h for the volumetrically efficient

design. With the improved performance well understood, a study varying the sweep ratio is conducted similarly to before; now, the results will show the best possible performance for the Pareto-optimal designs identified.

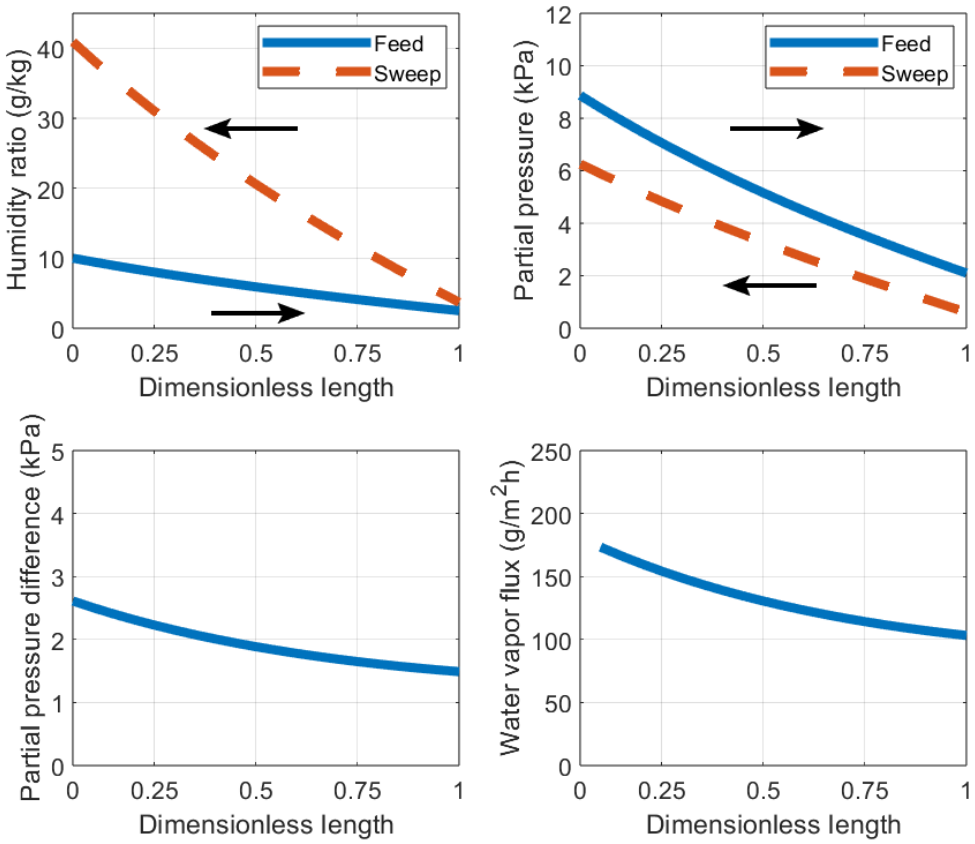

Figure 3.6: Distribution profiles of feed and sweep side humidity ratio (top left), feed and sweep side partial pressure (top right), partial pressure difference (bottom left), and water vapor flux (bottom right) for the module design with maximum dehumidification efficiency under aircraft relevant conditions with flow direction indicated.

The module design with the highest dehumidification efficiency was studied under varying sweep ratio ranging from 20% to 95%. The results of this study are shown in Figure 3.7. As before, the dehumidification improves as the sweep ratio is increased, with reduced rate of improvement at higher sweep ratios. Ultimately, at 95% sweep ratio, the feed side humidity ratio is reduced from 10 g/kg at the inlet to 0.54 g/kg at the outlet,

which corresponds to a saturation temperature of 233 K ≈ -40 °F. With this, it is clear that to achieve very low outlet saturation temperatures with currently available materials, high sweep ratios will be required. However, this is not a huge concern in an air cycle where there are abundant source of exhaust air that could be used as sweep; evaluating this is the focus of Chapter 4.

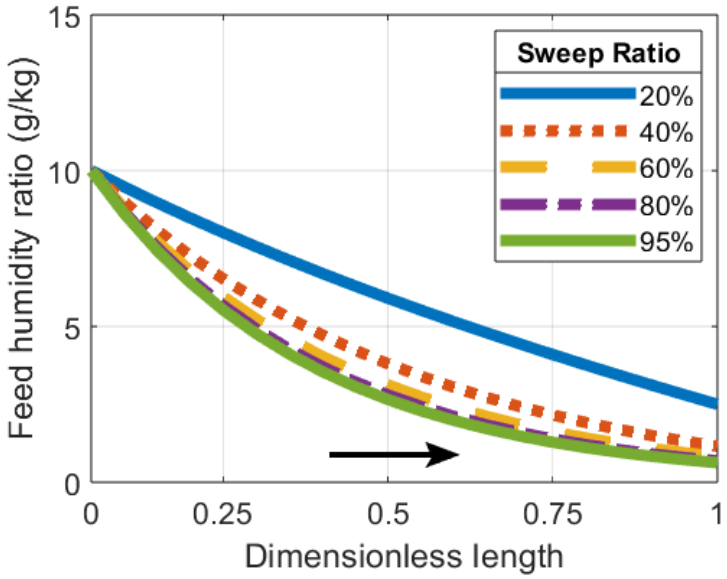

Figure 3.7: Feed side humidity ratio over the module with maximum dehumidification efficiency for a range of sweep ratios, with flow direction indicated.

Thus far, a Pareto optimal membrane design has been identified and its mass transfer capabilities characterized. To evaluate the suitability of the membrane module as a simultaneous heat and mass transfer device, the design is studied under adiabatic, non-isothermal conditions with an external sweep at a range of high temperatures. It should be noted that the polymer fibers have temperature limitations typically around 150°F; for this reason, the maximum allowable temperature of the exhaust sweep tested will be 338 K.

3.3.4 Hot Sweep Evaluation

Considering other studies have been overwhelmingly conducted under isothermal, product sweep conditions, a poorly characterized aspect of membrane dehumidification is the effect

of sweep temperature on local heat and mass transfer characteristics. To evaluate the non-isothermal membrane dehumidifier model, a test model is constructed with an external sweep source as shown in Figure 3.9. As before, the feed air is supplied at a given flow rate, temperature, pressure, and humidity ratio with a back pressure at the feed outlet, and the sweep outflow is kept at atmospheric pressure. With the external sweep source, the temperature and humidity ratio of the sweep air can be set to a desired value that is distinct from the product air properties. Also, the sweep reservoir pressure will be set to the feed side back pressure. Since the sweep air uses a mass flow source block to set the flow rate, which functions as a valve, the large pressure drop that occurs before the sweep air enters the sweep side of the membrane will occur the same as in the isothermal, product sweep architecture. Hence, the only variables being changed in this architecture compared to the product sweep is the sweep temperature and humidity ratio.

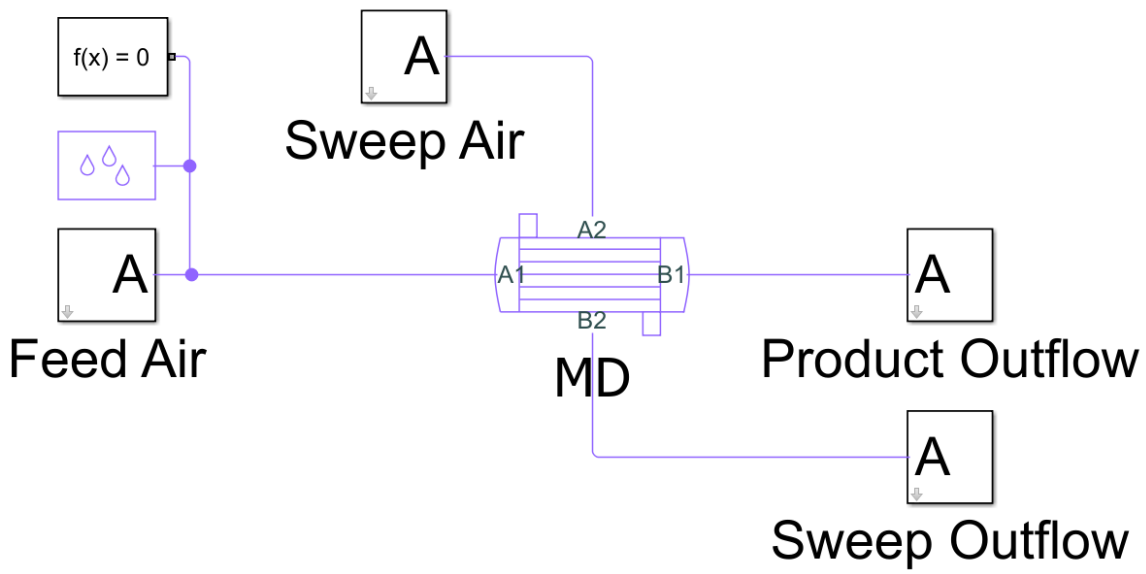

Figure 3.8: Model to evaluate adiabatic membrane dehumidifier under external sweep conditions.

To study the effects of sweep temperature, a study is run of the external sweep model shown in Figure 3.9 with the adiabatic membrane component model; i.e., the extended formulation with heat exchange between the feed and product sides. For this test, the

sweep temperature was set to 338 K, and the sweep humidity ratio was 0.54 g/kg; remark that this is the same as the feed outlet humidity ratio for 95% sweep from the product sweep architecture tests. Hence, no additional moisture is introduced on the sweep side for any test condition, with the goal of this test being to establish the maximum potential impact of hot sweep on membrane performance. All of the other test conditions are the same as before; feed flow rate, temperature, pressure, and humidity ratio were held at 0.5 kg/s, 320 K, 575 kPa, and 10 g/kg. As for the product sweep architecture, the sweep ratio was varied from 20% to 95%.

The temperature on each side of the membrane over the range of sweep ratios is shown in Figure 3.9. From this, it is clear that meaningful heat exchange of the feed side only occurs at higher sweep flow rates. At low sweep ratios, the sweep flow is much slower than the feed flow, and so by the effectiveness-NTU approach it will undergo the most temperature change. As the flow becomes more balanced, i.e. the flow rates become closer on both sides, the feed temperature is more greatly increased. At a sweep ratio of 95%, the outlet feed temperature is 336 K, almost matching the sweep inlet temperature of 338 K.

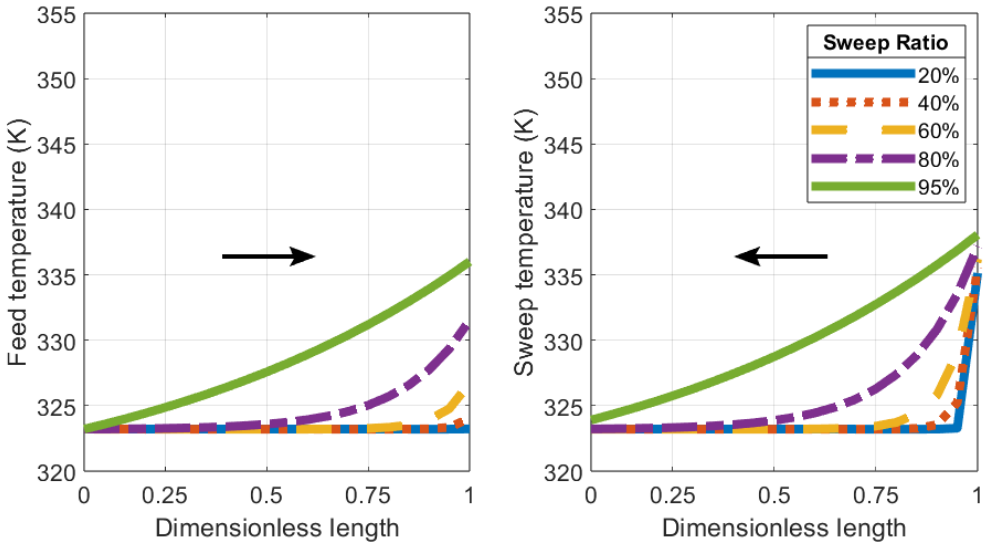

Figure 3.9: Heat exchange on feed and sweep sides of membrane dehumidifier for varying sweep ratios; fixed inlet temperature difference of 18 K.

In addition, at 95% sweep ratio the dehumidification rate is 16.861 kg/h, compared to 16.857 kg/h for the isothermal membrane in the product sweep architecture under the same sweep ratio. This 0.024% increase in dehumidification performance is due to the formulation of the mass transfer resistance - since the convective terms are ultimately proportional to $T^{-0.75}$, and the rate of vapor transfer is inversely proportional to the resistance, an increase in temperature slightly decreases resistance, which increases dehumidification performance. However, it should be noted that the model results presented here assume a constant permeation; in reality, permeability for air separation membranes typically increases as temperature increases, so dehumidification may be more significantly improved by the hot sweep [43]. Anyway, this study shows that the adiabatic membrane component model reasonably represents a membrane dehumidifier with simultaneous heat and mass transfer at sufficiently high sweep ratios.

3.3.5 Pareto-Optimal Module Designs for Future Materials

The multi-objective optimization study is repeated, evaluating the isothermal membrane with randomly generated module parameters over three increasing, constant permeabilities. The results of this study are shown in in Figure 3.10, highlighting the potential design trade-offs possible with future advancement in membrane materials. For all runs, the isothermal membrane model was exercised with product sweep ratio of 20% for a feed flow rate, temperature, pressure, and humidity ratio of 0.5 kg/s, 320K, 575 kPa, and 10 g/kg respectively over 1000 randomly selected values of d_o, d_i, D, ϕ, and L. The randomly selected module parameters were bounded and constrained the same as before, according to Equation 3.35.

Higher permeability offers a vastly increased range of module designs that have moderate volumes and much improved dehumidification efficiency. These material improvements are particularly relevant to applications with limited sweep supply. To utilize current

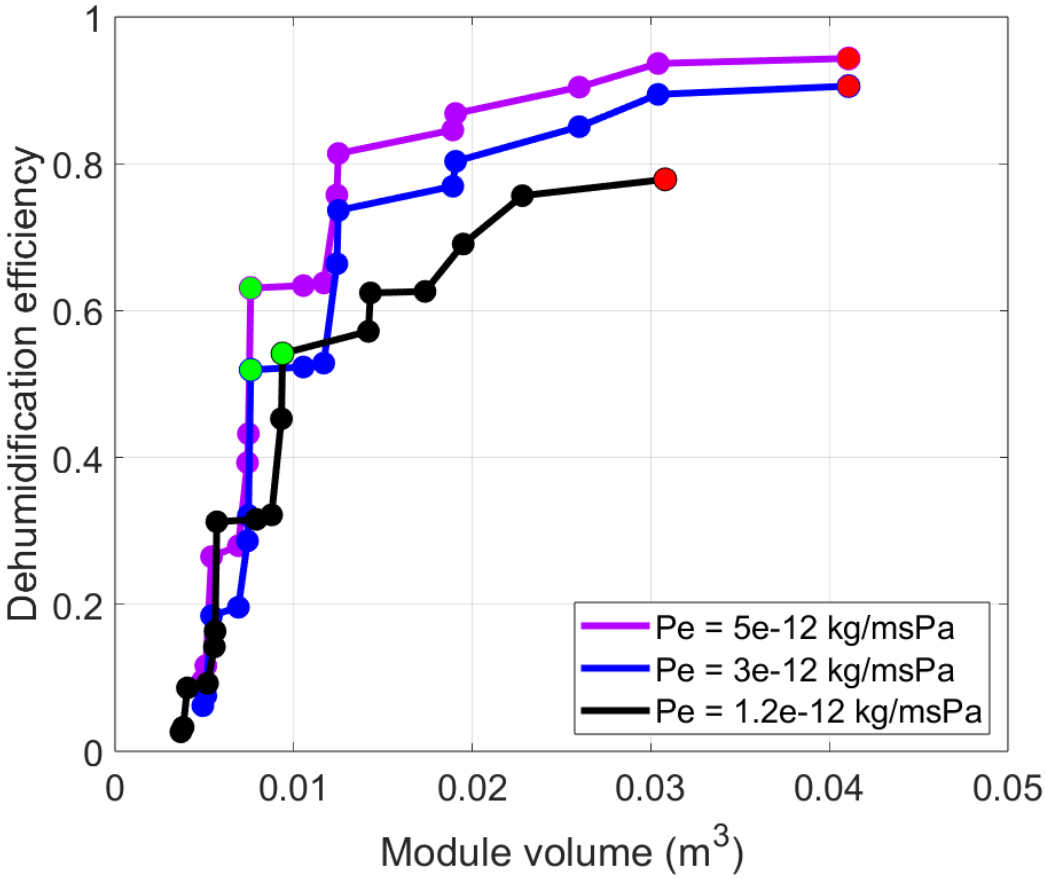

Figure 3.10: Pareto fronts from Monte Carlo searches over module design parameters with permeability fixed to 1.2, 3, and 5e-12 kg/m·s·Pa ≈ 2e5, 5e5, and 8e5 barrer respectively, with highest volumetric efficiency designs (green) and highest dehumidification efficiency designs (red).

materials, it has been demonstrated, as shown in Figs. 3.7 and 3.5, that the module design with the highest dehumidification module under high sweep is necessary to significantly lower the product air dew point. In the future, material advancements could produce the same performance at much lower volumes, thus increasing the volumetric efficiency.

3.4 Conclusions

Component models of a membrane dehumidifier module under isothermal and adiabatic conditions are developed and exercised under aircraft relevant conditions. Following thor-

ough verification and model exploration, a design study of membrane modules to identify the Pareto set of volumetrically efficient designs is conducted. From this, the designs that maximize efficiency per volume and dehumidification efficiency are selected and further evaluated under conditions relevant to aircraft applications. The local mass transfer characteristics are shown, as well as the dehumidification performance over a range of sweep ratios. From this, it is clear that despite its greater volume, the highest efficiency module design under high sweep is best suited to characterize the potential benefits of membrane dehumidification for aircraft applications. Further, the effects of simultaneous heat and mass exchange under hot sweep conditions, similar to aircraft exhaust, is evaluated.

From the design studies over a range of permeabilities corresponding to current and future material capabilities, it is shown that increased permeability enables higher efficiency per volume membranes. However, while the volumetrically efficient designs identified are certainly of interest for aircraft applications, it would be overly simplistic to assume these can be constructed as easily as smaller modules. In fact, the manufacturing process of membrane modules is generally limited to small fiber bundle diameters, with the packaging process growing increasingly complex as the module diameter increases [48–50]. Hence, the multi-objective optimization study shown here shows a potential future direction for membrane module design and fabrication.

Evaluation of a High-pressure Membrane Dehumidifier for Icing Mitigation in an Air Cycle Machine

High-pressure membrane dehumidification is of interest to increase air cycle machine cooling capacity while decreasing the risk of turbine icing. A key concern of this approach is the sweep requirement of membrane modules, with all prior investigations using product sweep. Since this sweep mode would significantly reduce the air cycle flow rate, alternative sweep sources, such as the system exhaust air, must be considered. To investigate the impact of membrane dehumidification and sweep modes on air cycle performance, component models are developed and assembled into three two-wheel air cycle subsystem architectures with thermal control. One architecture serves as a baseline, the second architecture is a membrane-only water vapor separation approach, and the third architecture combines the membrane with the baseline approach. Then, a series of simulations with constant boundary conditions are run to steady-state. The simulation results show that the second architecture yields the greatest performance improvement, increasing the steady state cooling capacity by 68.5% on average over the baseline. Beyond the cooling capacity for each set of boundary conditions, a number of other saturation and control related metrics are discussed. Overall, whether alone or with other water vapor separation components, membrane dehumidification is demonstrated to improve air cycle machine performance and mitigate icing at relatively low altitudes.

4.1 Introduction

In modern aircraft, thermal management system architectures based on air cycle machines have been developed to supply air at the appropriate temperature, pressure, and humidity to the cabin and avionics. An air cycle machine uses bleed air from the engine as its working fluid, and ram air as its coolant. With the increasing electrification of modern aircraft, the thermal management system must be able to handle larger thermal loads. Simultaneously, aircraft survivability requires that no additional penalties in terms of vehicle drag or engine performance be introduced. Thus, thermal management subsystems must find ways to increase the cooling capacity of the available bleed air; at the same flow, this must be done by lowering its temperature. The key barrier to producing colder air for thermal management purposes is the humidity in the bleed air which, at low temperatures, will deposit in the air cycle flowpath, seriously affecting system functionality. Traditionally, air cycle icing is mitigated through a condenser and high-pressure water separator which condense out a significant amount of the water vapor carried in the air, along with regulation of the turbine outlet temperature to just above freezing. This work compares the traditional approach with one that incorporates a membrane dehumidifier, evaluating its feasibility for icing mitigation.

Several investigations have assessed the potential applicability of membrane dehumidification (MD) across a wide array of industrial applications, including thermal waste recovery [85, 95, 96], purification and water recovery from waste gaseous streams [97], and aircraft environmental systems [39–41, 84]. These latter studies are a series of investigations from Yuan et al. into the modeling and simulation of membrane dehumidification in an aircraft environmental control system (ECS). In 2015, they compared a novel membrane dehumidification-based ECS architecture (MD-ECS) to the most advanced commercial ECS - a four wheel architecture similar to a baseline ACM but with an additional fan and turbine (4W-ECS). The results of this investigation show an increased cooling capacity of the MD-ECS over the 4W-ECS under the same operating conditions, indicating the

promise of the proposed architecture [84]. More recently, they published empirical findings of a high-pressure membrane dehumidifier under aircraft conditions with a validated membrane dehumidifier model [41].

This work builds on their model, and extends it to evaluate the subsystem-level benefits of a membrane dehumidifier for a two-wheel air cycle architecture. The two-wheel architecture is selected for its relative simplicity, and also because this work is an initial evaluation of potential benefit. Subsequent studies to optimize a membrane-based ACM architecture are anticipated to be the subject of future work. To conduct this evaluation, a series of physical models are developed in MATLAB® Simscape™, with the architectures considered being novel in and of themselves. Further, the subsystem-benefits of a membrane dehumidifier under exhaust sweep and in addition to the traditional condensing-based HPWS has not been evaluated elsewhere.

4.2 Controlled Air Cycle Machine Architectures

The controlled air cycle machine (ACM) subsystem models each consist of a number of moist air components, connected to form an ACM architecture of interest. Each architecture has a set of sensors at 12 flow points, denoted by S1 through S12, that measure the simulated flow conditions at the indicated locations. These sensors include values for mass flow rate, temperature, pressure, various humidity metrics, and saturation conditions. These sensor readings will be used to compare the steady-state performance of each architecture, and show how the flow properties change as air moves through the system. Each architecture considered as part of this work are two-wheel (2W) architectures, meaning that each consists of two pieces of turbomachinery: a compressor and turbine.

4.2.1 Architecture 1: Condenser-based Dehumidification

The two-wheel air cycle machine architecture (2W-ACM) is shown in Figure 4.1 and consists of the fundamental components that make up a 2W-ACM with high-pressure water separation: bleed and ram air flows, primary and secondary heat exchangers (PHX and SHX respectively), a reheater, a condenser, a compressor, a turbine, and a pressurized exhaust. Due to the inability of the moist air domain to represent and track liquid water that condenses out, the high pressure water separator that would typically be located between S6 and S7 is omitted in these models; the water that condenses from the flow is ideally removed within the condenser component, effectively behaving as both the condenser and a high pressure water separator in a real-world ACM. The heat load applied in all architectures is equal to the available cooling capacity at that point with respect to a maximum exhaust temperature of T_{max} = 330 K as:

$$\text{Applied heat load } = \dot{m}_{10} c_{p,10} (T_{max} - T_{10}) \tag{4.1}$$

This ensures that the temperature at S11, which is used as membrane sweep in the second and third architectures, is always at the same temperature. It also establishes a fair point to compare performance of each system by measuring cooling capacity with respect to the same set point. This specific maximum temperature is chosen for two reasons: (1) to ensure the membrane is operated within its allowable temperature range, and (2) to show the cooling capacity for a real-world heat load, such as avionics, for which a maximum temperature of 330 K is reasonable.

In this baseline architecture, the bleed air is supplied to the PHX where it is cooled by the ram air. Then, it is compressed, cooled again by ram air in the SHX, cooled in the reheater, brought to saturation in the condenser, reheated before expansion, and then put through an expansion turbine. Once expanded, the air is passed through the cold side of the condenser and is now ready for use to offset thermal loads on the aircraft. The air at this point, characterized by the sensor S10, is called the product or exit air of the system. It is

used to offset the applied heat load.

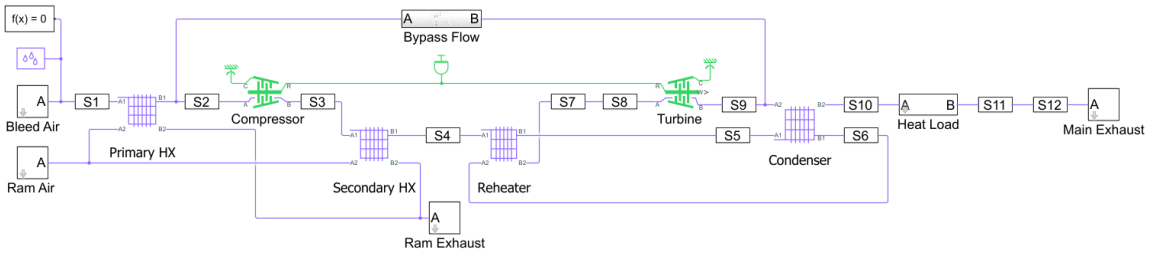

Figure 4.1: Thermally controlled 2-wheel air cycle machine architecture (Architecture 1).

Thermal control is maintained in this architecture via the bypass flow line, which consists of a series of ducts and a flow control valve. The set point of the flow control valve is determined as:

$$T_{set} = \min(277.0\text{ K}, \max(T_{sat,turb,in}, 230\text{ K})) \tag{4.2}$$

where $T_{sat,turb,in}$ is the saturation temperature of the turbine inlet. This control scheme opens the bypass flow valve, and ensures that any condensation that occurs within the turbine will not be able to experience icing. In the baseline architecture, the humidity is almost always high enough to force the bypass controller to a set point of 277.0 K, which is a few degrees above freezing. So, vapor can condense out in the turbine, but will not freeze. However, in membrane-based architecture, lower set points are frequently preferred since the air has been dried in the membrane dehumidifier, and since the saturation point below freezing will be the frost point, no icing will occur so long as thermal control at the outlet is maintained. The minimum allowable turbine outlet temperature is regulated to 230 K to avoid violation of the minimum allowable temperature of the moist air model.

4.2.2 Architecture 2: Membrane-based Dehumidification

This architecture is a two-wheel air cycle machine with a membrane dehumidifier (MD) using exhaust sweep, shown in Figure 4.2. It is fundamentally similar to architecture 1, but

excludes the reheater and condenser as these are the traditional water separation approach. Instead, only the MD is used to dry the air before expansion in the turbine. The MD is incorporated between S6 and S7, with the sweep air is taken from the ACM exhaust flow at S11. Considering that the exhaust air will be at a high temperature because it is taken downstream of an applied heat load, the non-isothermal MD formulation is used; however, considering the temperature of the flow out of the secondary heat exchanger, there is not a large temperature difference across the membrane. As in the baseline model of architecture 1, thermal control of the turbine outlet is achieved via the bypass flow according to the same control scheme.

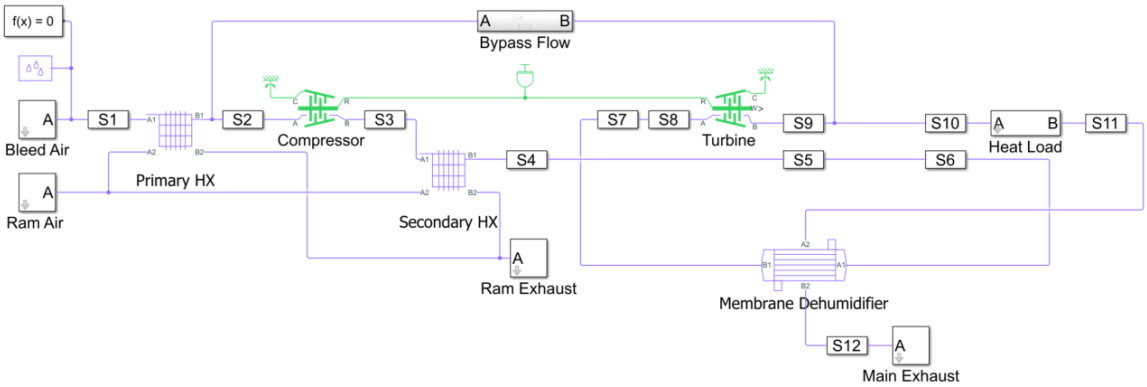

Figure 4.2: Thermally controlled 2-wheel air cycle machine architecture with membrane dehumidifier using exhaust sweep (Architecture 2).

4.2.3 Architecture 3: Combined Dehumidification Approach

The final architecture consists of a two-wheel air cycle machine with a combined water separation approach consisting of a condenser, reheater, and membrane dehumidifier using exhaust sweep. This is fundamentally similar to architecture 1, but introduces an additional component - a hollow-fiber MD - between S7 and S8, with the sweep air taken from the ACM exhaust flow at S11. Considering that the exhaust air will be at a high temperature because it is taken downstream of an applied heat load, the non-isothermal MD formulation is used. However, as for architecture 2, there is not a large temperature difference because

of the reheater. Thermal control of the turbine outlet is achieved via the bypass flow, the same as for architectures 1 and 2.

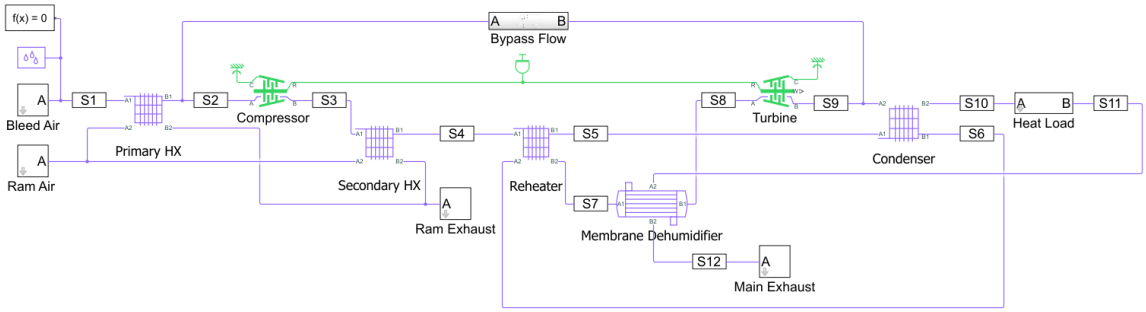

Figure 4.3: Thermally controlled 2-wheel air cycle machine architecture with membrane dehumidifier using exhaust sweep (Architecture 3).

4.3 Formulation

A brief formulation for each of the major components is presented; for a more in-depth treatment, refer to Appendix E.

4.3.1 Phase Change: Condensation and Deposition

In the forced moist air flow within an air cycle machine, the water vapor constituent of the air can condense or deposit out of the air flow if saturation conditions are met. Saturation conditions are defined by relative humidity and temperature. The dew and frost point expressions developed by Romps are used to find the saturation condition for a control volume under consideration [2]. With this, the saturation conditions at each sensor can be determined, enabling saturation temperature control at the turbine inlet with the bypass flow. Depending on whether the turbine outlet is above or below freezing, the rate of phase change will be considered either condensation or icing. Regardless, it is determined by the flow rate of the moist air, m_a, and its supersaturation degree as:

$$\dot{m}_{cond/ice} = \dot{m}_a(x_w - x_{w,sat}) \tag{4.3}$$

The supersaturation degree, $x_w - x_{w,sat}$ is determined from the saturation pressure at the flow conditions. The corresponding energy loss of condensation/icing is:

$$\phi_{cond/ice} = \dot{m}_{condense}(h - h_{vap/sub}) \tag{4.4}$$

where $h_{vap} = h_{vap}(T)$ is the enthalpy of vaporization of water at the flow temperature, and $h_{sub} = 2838$ kJ/kg is the enthalpy of sublimation.

Condensation as described here can be present in an air cycle machine within the heat exchangers whenever the flow is substantially cooled, especially the condenser, as well as the expansion turbine. When the turbine outlet is permitted to be sub-freezing, the phase change products are assumed to be ice. Due to the inability of the developed components to track phase change products, accumulation of condensate or ice/frost is not represented. The expansion of the current modeling tools to include tracking of liquid water and solid ice constituents, as well as contain a variable volume depending on the accumulation of these constituents, would be an appropriate subject for future work.

4.3.2 Membrane Dehumidfier

For a hollow-fiber membrane dehumidifier module consisting of N porous fibers with permeability Pe, length L, and outer and inner diameters d_o and d_i respectively, the rate of mass transfer of water vapor from the feed side to the permeate side is given by:

$$\dot{m}_v = \frac{p_{v,f} - p_{v,p}}{r} \tag{4.5}$$

where $p_{v,p}$ and $p_{v,f}$ are the vapor partial pressures on the permeate and feed sides respectively, and r is the overall mass transfer resistance, defined as:

$$r = \frac{\ln\left(\frac{d_o}{d_i}\right)}{2\pi PeL} + \frac{RT_f}{N\pi d_i M_v k_f L} + \frac{RT_p}{N\pi d_o M_v k_p dz} \tag{4.6}$$

Here, R is the universal gas constant, M_v is the molar mass of water vapor, and T_f, T_p and k_f, k_p are the temperatures and convective mass transfer coefficients on the feed and permeate sides respectively. For a more complete treatment of the mass transfer in the membrane

dehumidifier, refer to the formulation of Chapter 3. The membrane parameters used for all design point simulations are shown in Table 4.1, and correspond to the membrane module with the highest dehumidification efficiency identified in Chapter 3.

Parameter	Value	Unit
Fiber outer diameter	0.5093	mm
Fiber inner diameter	0.4060	mm
Shell inner diameter	0.2516	m
Shell packing fraction	0.4307	1
Fiber length	0.6198	m
Module length	0.8264	m

Table 4.1: Geometry of membrane module with highest dehumidification efficiency for a fixed permeability of $Pe = 1.2 \times 10^{-12}$ kg/m·s·Pa $\approx$ 200,000 barrer.

4.3.3 Turbomachinery

An air cycle relies on two pieces of turbomachinery - an axial flow compressor and turbine - to compress and subsequently expand the air to a lower temperature than the initial working fluid conditions. The compressor is powered by the turbine, which extracts power from the flow as it expands it. This power is transmitted to the compressor via a common shaft, which then compresses the incoming air.

The compressor model represents simplified air compressor behavior where power from a mechanical rotational network is used to drive the moist air flow of the air cycle. In this simplified model, the compressor map is scaled based on a known nominal operating condition and its shape is approximated by empirical coefficients. The nominal operating condition is defined by a design pressure ratio, corrected mass flow rate, and corrected shaft speed, denoted by $PR_{des}, \dot{m}_{corr,des}$, and $\omega_{corr,des}$. This nominal operating condition corresponds to reference pressure, temperature, and relative humidity conditions of p_{ref}, T_{ref}, and RH_{ref} respectively. In addition, the compressor has mechanical and polytropic efficiencies of η_{mech} and η_{poly}. With these, the actual operating conditions can first be scaled to the reference conditions and then corrected to give the corresponding outlet conditions

via the compressor map. The efficiencies are used to determine the work done by the compressor and corresponding torque; a detailed formulation can be found in Appendix E.1.1.

An axial flow turbine is used to expand the moist air in an air cycle machine. This component is critical for icing considerations, with the inlet saturation temperature dictating the required bypass control. The turbine model used represents simplified turbine behavior where work is extracted from the moist air to drive the common shaft that connects the compressor and turbine. To establish a known performance point, nominal pressure ratio and corrected flow rate values, denoted PR_{des} and $\dot{m}_{corr,des}$ respectively, are provided as inputs. These are scaled to other operating conditions using Stodola's ellipse [98,99]. Other necessary input parameters are a reference condition, defined by pressure p_{ref}, temperature T_{ref}, and relative humidity RH_{ref}. In addition, the turbine has polytropic and mechanical efficiencies of η_{poly} and η_{mech}. As for the compressor, the turbine efficiencies are used to determine the work done and torque of the common shaft; a detailed formulation can be found in Appendix E.1.2.

The reference pressure, temperature, and relative humidity for both the turbine and compressor were set to 101.325 kPa, 288.15 K, and 0 respectively. The full set of input parameters for both turbomachinery components are provided in Table 4.2. The design corrected mass flow rate changes with the set system flow rate; further discussed in 4.3.5.

Component	Parameter	Value	Unit
Compressor	η_{mech}	0.98	1
	η_{poly}	0.92	1
	PR_{des}	2	1
	$\omega_{corr,des}$	40,000	rpm
Turbine	η_{mech}	0.98	1
	η_{poly}	0.92	1
	PR_{des}	0.25	1

Table 4.2: Turbo-machinery design and performance parameters.

4.3.4 Heat Exchangers

All of the heat exchangers (HXs) in the air cycle are modeled as unmixed, cross-flow moist air-moist air exchangers. The specific geometries of the exchanger cores are not represented; instead, the effectiveness-NTU method is used to estimate the heat transfer between the hot and cold flows since the outlet conditions are unknown and must be determined from the inlet conditions. To use the ϵ-NTU method, a number of design parameters are required. Each side of each HX has a design temperature, T_{des}, mass flow rate, $\dot{m}_{des}$, and specific heat capacity, $c_{p,des}$. In addition, the heat transfer performance is dictated by a design heat transfer rate, Q_{des}, and a design pressure drop Δp_{des} is provided as well. From these design conditions, the design effectiveness, number of transfer units, NTU$_{des}$, and overall heat transfer coefficient times heat transfer area, UA, are found. The design heat transfer performance is then scaled to the actual operating conditions, and the scaled heat transfer rate is used to determine the temperature change on each side. Similarly, the design pressure drop is scaled to find the actual pressure drop. For a full treatment of the ϵ-NTU method and how it is scaled to the operating conditions, refer to Appendix E.2. The full set of design parameters provided to each heat exchanger for all of the simulations are provided in Table 4.3.

4.3.5 Design Point Boundary Conditions

For this study, operational design points at mach 0.2 and a range of altitudes are selected, leading to the set of ambient and ram conditions shown in Table 4.4, as well as the corresponding source and sink parameters for the bleed air, ram air, and exhausts shown in Table 4.5. The detailed formulation for the ram and ambient conditions can be found in Appendix E.3.

For each altitude, the ram and bleed flow rates are each set to 0.5, 1.0, and 1.5 lbm/s. Recalling that the MD module was designed for a flow rate of 0.5 kg/s ($\approx$ 1.1 lbm/s), this

Component	Parameter	Value	Unit
Primary heat exchanger	Q_{des}	100	kW
	T_{des}	450	K
	$T_{cool,des}$	260	K
	$\dot{m}_{cool,des}, \dot{m}_{des}$	1	kg/s
	Δp_{des}	20	kPa
Secondary heat exchanger	Q_{des}	150	kW
	T_{des}	450	K
	$T_{cool,des}$	260	K
	$\dot{m}_{cool,des}, \dot{m}_{des}$	1	kg/s
	Δp_{des}	20	kPa
Reheater	Q_{des}	10	kW
	T_{des}	310	K
	$T_{cool,des}$	290	K
	$\dot{m}_{cool,des}, \dot{m}_{des}$	1	kg/s
	Δp_{des}	20	kPa
Condenser	Q_{des}	30	kW
	T_{des}	320	K
	$T_{cool,des}$	277	K
	$\dot{m}_{cool,des}, \dot{m}_{des}$	1	kg/s
	Δp_{des}	20	kPa

Table 4.3: Heat exchanger design parameters for the controlled ACM architectures.

Flight Altitude (ft)	Ambient Temperature T_{amb} (K)	Ambient Pressure p_{amb} (kPa)	Ambient Humidity Ratio HR_{amb} (g/kg)	Ram Temperature T_{ram} (K)	Ram Pressure p_{ram} (kPa)
5,000	290.8	85.4	10.9	293.1	87.8
10,000	281.1	71.3	5.4	283.4	73.3
20,000	261.9	48.2	1.1	264.0	49.6

Table 4.4: Ambient and ram conditions corresponding to operational design points.

range is chosen to demonstrate the effects of operating the MD at and off design. The bleed and ram flow rates are assumed equal to yield balanced flow in the primary and secondary heat exchangers, minimizing their size. The ram source flow rate is double the bleed/ram flow since only one source is used for two ram heat exchangers, and the source flow is split between them. The values chosen for the bleed/ram flow rate can reasonably be achieved for a given design point via control valves and ram duct design. Further, the turbomachinery are assumed to operate at the given flow rate, i.e. the design flow rate of the compressor

and turbine are scaled with the bleed flow rate. For the compressor, the design flow rate is set equal to the bleed flow rate; for the turbine, it is set to one fourth of that rate.

Component	Parameter	Value	Unit
Bleed air source	Temperature	450	K
	Pressure	≤ 265	kPa
	Humidity ratio	HR_{amb}	g/kg
	Mass flow rate	[0.5, 1.0, 1.5]	lbm/s
Ram air source	Temperature	T_{ram}	K
	Pressure	p_{ram}	kPa
	Humidity ratio	HR_{amb}	g/kg
	Mass flow rate	[1.0, 2.0, 3.0]	lbm/s
Main Exhaust sink	Temperature	293.15	K
	Pressure	120	kPa
Ram exhaust sink	Temperature	T_{amb}	K
	Pressure	p_{amb}	kPa

Table 4.5: Source and sink conditions for all operational design points.

The bleed air is kept at a constant temperature with a maximum regulated pressure, as shown. A range of pressures can be readily achieved for each design point via pressure regulating valves, and for the chosen back pressure the bleed pressure varies between 185 and 265 kPa ($\approx$ 27-38 psia). While the bleed temperature does vary during flight the chosen value is reasonable for low speed, low altitude operation. Exercising the controlled two-wheel architecture at these boundary conditions with the corresponding heat exchanger and turbomachinery parameters yields the typical temperature, pressure, mass flow rate, and humidity profiles at each sensor, showing good agreement with similar steady-state operation [29, 84]. Each simulation is run for 600 seconds to reach steady-state.

4.4 Results and Discussion

The air cycle subsystem architectures were each exercised over the range of operational design points detailed in Table 4.4. For each architecture and each design point, the cooling capacity with respect to a maximum temperature of 330 K is found, as well as the saturation

temperature at the turbine inlet and the amount of bypass flow needed for thermal control; these results are shown in Tables 4.6 and 4.7.

There are many interesting trends that these steady-state results indicate. First, across all operational design points, it is clear that incorporating a MD increases the cooling capacity of the system, regardless of whether it is used alone or in combination with the traditional water separation approach (i.e., condenser, high-pressure water separator, and reheater). Architecture 2 shows the largest increase in cooling capacity since it does not have a condenser, which consumes large amounts of latent cooling capacity. On average, architecture 2 increases the cooling capacity by 68.5%, and architecture 3 increases it by 24.3%. Moreover, the increased cooling capacity holds across the range of relatively low altitudes considered, with the highest average increase for architecture 2 at 20,000 ft, the highest altitude. This makes sense as the ambient humidity is lowest at this operational design point, and so the MD produces the driest air under these conditions.

Beyond the increased cooling capacity of the architectures which incorporate a MD, Table 4.7 shows the saturated turbine inlet temperature, bypass flow set point for the turbine outlet, bypass flow rate, relative humidity into the MD, and the rate of turbine condensation or icing for all architectures at all operational design points. From this, it is clear that the MD reduces the turbine inlet saturation temperature, with the lowest saturation points shown for architecture 3. However, due to the presence of the condenser, the lower turbine outlet temperatures which result in lower bypass flow are negated by the condenser; this is why architecture 3 does not show as much increase in cooling capacity as architecture 2, even though it often has lower turbine outlet temperatures. Because architecture 2 lacks a condenser, any decrease in the turbine outlet temperature control can be directly used to offset the applied heat load.

With architecture 3 consistently having the lowest turbine inlet saturation temperature, it also typically requires the lowest bypass flow. However, both architectures 2 and 3 require less bypass than architecture 1 across all conditions. The final saturation related metric

Altitude (ft)	$\dot{m}_{bleed/ram}$ (lbm/s)	ACM Architecture	$\dot{Q}$ (kW)	Increase compared to Architecture 1 (%)
	0.5	1	8.72	
		2	13.47	54.5
		3	11.09	27.2
5,000	1.0	1	14.89	
		2	24.24	62.8
		3	16.37	9.9
	1.5	1	16.17	
		2	36.62	126.5
		3	22.35	38.2
	0.5	1	9.90	
		2	15.83	59.9
		3	12.65	27.8
10,000	1.0	1	17.37	
		2	27.76	59.8
		3	20.00	15.1
	1.5	1	20.00	
		2	37.66	88.3
		3	26.69	33.5
	0.5	1	11.47	
		2	21.13	84.2
		3	13.99	22.0
20,000	1.0	1	20.85	
		2	35.93	72.3
		3	24.91	19.5
	1.5	1	26.32	
		2	49.62	88.5
		3	33.15	25.9

Table 4.6: Cooling capacity of controlled ACM architectures over a range of altitudes and system flow rates with percent increase in cooling capacity of architectures 2 and 3 compared to architecture 1, taken as a baseline.

shown is the inlet relative humidity to the MD in architectures 2 and 3. Considering the MD cannot handle liquid water, it is pertinent that the relative humidity be 100% or less; i.e., supersaturation may decrease real-world membrane performance. With this in mind, architecture 2 is shown to have good inlet relative humidity for all conditions. On the other hand, architecture 3 is supersaturated going into the membrane at the low flow rate, low altitude condition. This highlights potential integration issues for a MD into existing air

cycle water separation loops.

The last two columns of Table 4.7 show the rate of condensation and icing for each architecture at each operational design point. These values demonstrate that the rate of phase change in the turbine is reduced when a membrane dehumidifier is introduced, but not always to zero. This is because the enacted control at the turbine outlet is solely temperature-based, but the saturation conditions depend on temperature and pressure. A key observation from these results is that at 20,000 ft., the rate of icing in the turbine is reduced to 0 for both membrane-based architectures over all flow rates. This highlights the importance of operational design point on expected system performance, and shows that membrane-based icing mitigation can truly be realized when the ambient humidity is relatively low.

Figure 4.4 shows a number of flow quantities at each sensor location for each architecture at the 10,000 ft. operational design point with a bleed and ram flow rate of 0.5 lbm/s. As expected, the typical decreases and increases in temperature (top left) and pressure (middle left) are shown across the HXs and turbomachinery, with the turbine outlet temperature controlled to the bypass set point. The enthalpy of the flow (top right) tracks with the temperature, with decreases in temperature corresponding to decreased flow enthalpy. Ultimately, the architecture 1 has the greatest final exhaust temperature, and so it also has the highest exhaust enthalpy. Remark that although the turbine outlet temperature is lowest for architecture 3, because the air is then warmed in condenser it has less cooling capacity at sensor 10 than the air conditioned via architecture 2. This is precisely why architecture 2 provides greater benefit overall, and potential condenser/architecture re-designs may be able to alleviate this performance difference.

The bypass flow required for each architecture is shown in the air mass flow rate (middle right) at each sensor, with architecture 1 requiring the most bypass flow, architecture 2 requiring less, and architecture 3 requiring essentially none at this operational design point. Because the pressure ratios across the turbine and compressor are fixed, their design points are set to the bleed flow rate, and the back pressure is fixed, the maximum pressure achieved

Altitude (ft)	$\dot{m}_{bleed}$ (lbm/s)	ACM Architecture	$T_{sat,turb,in}$ (K)	T_{set} (K)	$\dot{m}_{bypass}$ (kg/s)	$RH_{MD,in}$ (%)	$\dot{m}_{cond}$ (g/s)	$\dot{m}_{ice}$ (g/s)
	0.5	1	297.2	277.0	0.06	-	0.92	-
		2	270.6	270.6	0.04	99.87	0.08	-
		3	223.9	230	4e-7	102.02	-	0
5,000	1.0	1	300.7	277.0	0.10	-	2.29	-
		2	278.6	277.0	0.09	57.33	0.34	-
		3	275.1	275.1	0.09	93.95	0.23	-
	1.5	1	304.1	277.0	0.10	-	3.64	-
		2	285.0	277.0	0.10	25.01	0.87	-
		3	280.1	277.0	0.12	82.88	0.51	-
	0.5	1	288.7	277.0	0.07	-	0.55	-
		2	260.4	260.4	0.03	45.32	-	0.02
		3	189.1	230	4e-7	67.27	-	0
10,000	1.0	1	291.0	277.0	0.12	-	1.23	-
		2	269.4	269.4	0.07	28.80	-	0.12
		3	265.8	265.8	0.06	64.28	-	0.07
	1.5	1	292.7	277.0	0.14	-	1.90	-
		2	275.7	275.7	0.11	14.39	0.33	-
		3	272.0	272.0	0.11	59.38	-	0.20
	0.5	1	271.2	271.2	0.07	-	-	0.16
		2	170.4	230	4e-7	7.33	-	0
		3	161.6	230	4e-7	24.08	-	0
20,000	1.0	1	271.5	271.5	0.13	-	-	0.32
		2	251.5	251.5	0.03	6.06	-	0
		3	246.4	246.4	0.02	22.32	-	0
	1.5	1	272.1	272.1	0.17	-	-	0.47
		2	258.1	258.1	0.05	3.72	-	0
		3	255.0	255.0	0.05	20.71	-	0

Table 4.7: Saturation, control, and phase change metrics for all architectures, including the turbine inlet saturation temperature, turbine outlet set point, bypass flow rate, relative humidity at the membrane dehumidifier inlet, and rates of condensation and icing in the turbine.

between the compressor and turbine varies for each architecture depending on the bypass flow required. Since architecture 3 requires very little bypass, the compressor is actually operating at its design point and thus the commanded pressure ratio of 2 is achieved. The pressure ratios for architecture 1 and 2 decrease as their required bypass flow increases, with architecture 1 (which requires the most bypass flow) having a pressure ratio of only 1.64 across the compressor. For architecture 2, the decrease is maximum pressure also

leads to decreased dehumidification performance in the membrane, since the partial pressure on the feed side will be lower at lower total pressure; turbomachinery re-design could improve this.

The final two plots show the humidity ratio (bottom left) and relative humidity (bottom right) traces across all of the sensors for each architecture. In the baseline architecture, water vapor condenses out in the reheater, condenser, and turbine, corresponding to points where the relative humidity reaches saturation. For architecture 2, the water vapor is only decreased by the membrane between sensors 6 and 7; under these operating conditions, the MD is able to remove 94% of the water vapor present, reducing the vapor from 5.4 g/kg at sensor 6 to 0.33 g/kg at sensor 7. In architecture 3, the inlet humidity for the membrane is much lower since it has been reduced already in the reheater and condenser. Accordingly, the membrane is able to remove 98.8% of the vapor, reducing the humidity ratio from 2 g/kg at sensor 7 to 0.02 g/kg at sensor 8. In terms of relative humidity, saturation is reached in the reheater and condenser for architecture 3 as well, corresponding to condensing of vapor from the flow. The humidity ratio and relative humidities at sensor 8, the turbine inlet, are reflected by the turbine inlet saturation temperatures discussed earlier, shown in Table 4.7. Overall, the results demonstrate that the MD significantly reduces water vapor content prior to expansion.

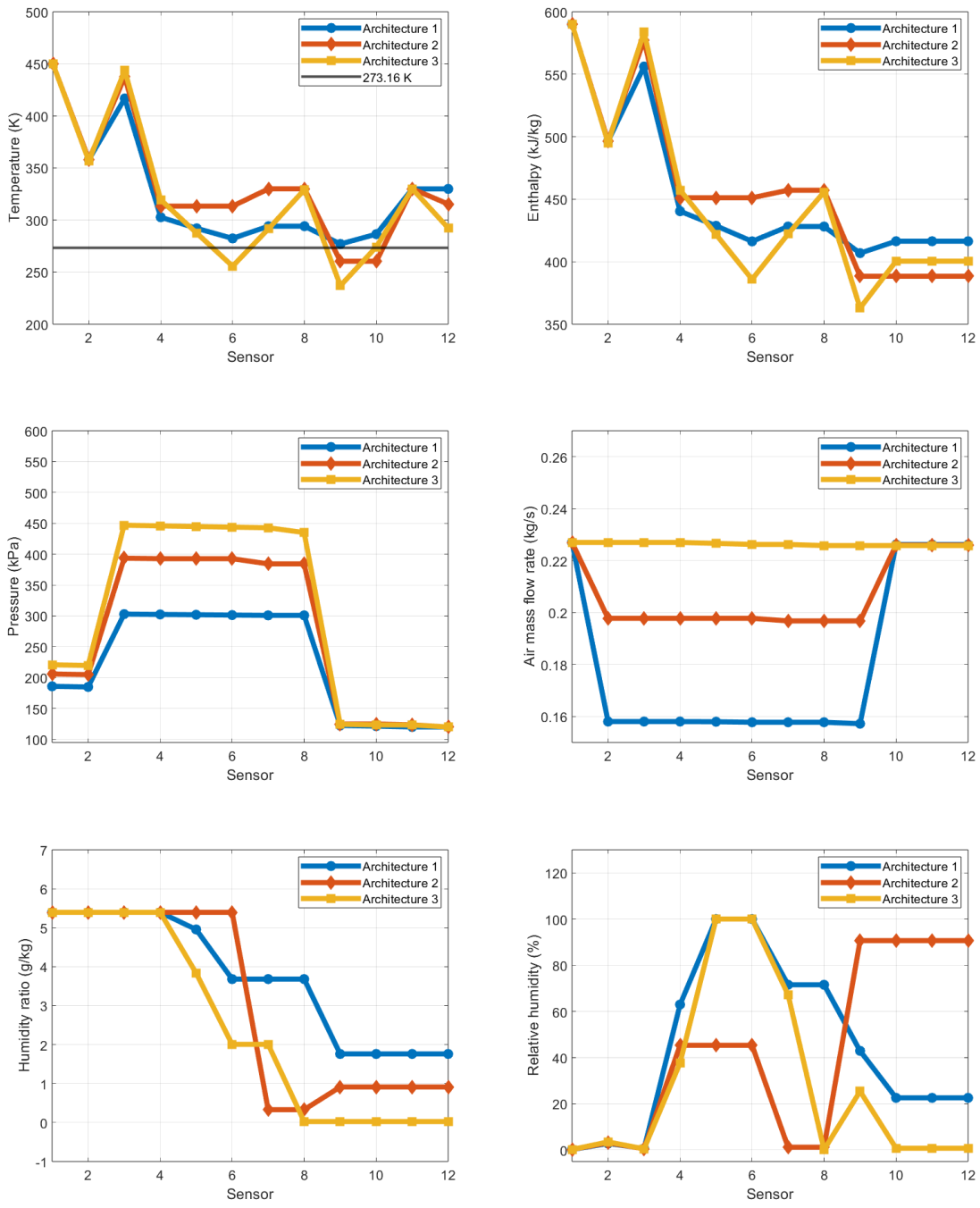

Figure 4.4: Flow characteristics at each sensor for all architectures at 10,000 ft. and bleed/ram mass flow rate of 0.5 lbm/s.

4.5 Conclusions

Subsystem models of two-wheel air cycle machine architectures subject to turbine outlet temperature control via a bypass flow are defined, developed, and exercised over a range of relevant operational design points. Formulations for each major component are presented, with extended formulations presented in Appendix E. The simulation results indicate that incorporating a membrane dehumidifier increases air cycle cooling capacity, with the architecture only using a membrane dehumidifier showing the greatest benefit. From analysis of steady-state sensor readings, as well as saturation, control, and phase change metrics, a better understanding of the impact of a membrane dehumidifier on the chosen architectures and design points is established. Ultimately, this study presents an initial evaluation of potential membrane-based air cycle architectures, and highlights the operational design points where membrane-based water vapor separation approaches can most effectively mitigate icing.

Summary of Contributions, Results, and Impacts

The three chapters of this work investigated the fundamentals of desublimation, membrane dehumidification, and subsystem integration for air cycle machines. The investigation pertaining to frost growth and densification yielded a novel, non-restrictive analytical solution for sufficiently cold flat surfaces. The accuracy of this solution was compared to relevant frost thickness databases for different frost densities, required for model closure. Then, the accuracy was compared to other predictive methods. In all, the proposed solution is numerically simpler and was found to be comparably or more accurate. The development of this solution enables straightforward frost predictions and is applicable to a wide number of investigations for frost growth; a corresponding manuscript has been submitted to the International Journal of Heat and Mass Transfer, and is currently under review.

With this solution, modeling and model validation of frost growth in relevant air cycle components, such as air-air plate-fin heat exchangers, could be the subject of of a future experimental validation campaign. The frost growth and densification solution that has been developed here could be implemented in a custom component for a variable volume air-air plate-fin heat exchanger. Moreover, empirical data will be required to validate this. For this, a number of experimental heat exchanger studies varying air temperature, humidity, etc. could be conducted to study the effective blockage ratio of the flow channels over time, and compared with model predictions. In the long-term, this approach would provide an accurate way to predict and track the growth of frost on sub-freezing heat exchanger surfaces

which will become increasingly relevant as sub-freezing air cycle operation is practically realized.

With respect to membrane dehumidification, the investigations detailed here present a reasonable approach to optimization of high capacity membrane module design. A number of related novel findings characterize the design space for currently available materials, as well as the benefits of material advancements in the near-term and longer. Further, a number of modeling explorations to evaluate whether certain model assumptions, such as constant packing fraction, are reasonable considering knowledge of real-world manufacturing practices. In all, the optimal module designs identified provide motivation for manufacturing advancement of membrane dehumidification modules.

The proposed design approach could be extended to a wide range of operating design points, i.e. ambient humidities and nominal flow rates. This would better characterize the potential design space relevant to aircraft applications of membrane dehumidifiers. Other natural extensions to the current work would be expanding the mass transfer formulation to include variable membrane permeation as a function of temperature and humidity. Another worthwhile consideration would be a volumetric efficiency comparison of membrane dehumidifiers to desiccant approaches; however, in aircraft applications, desiccant dryers typically require unfavorable maintenance schedules. One final related idea would be the exploration of incorporating an ejector on the sweep side of the membrane, to further reduce the sweep side total pressure, and thus its partial pressure.

In the final chapter, an investigation into a membrane-based air cycle machine using exhaust sweep is presented. This investigation is altogether novel in utilizing exhaust sweep for the membrane, and elaborates on prior work establishing limitations on product sweep mode for membrane dehumidifiers in air cycle machines. The findings demonstrate that, compared to a baseline two-wheel architecture with high-pressure water separation, a membrane-based architecture using exhaust sweep results in a significant increase in cooling capacity. In all, the results shown here provide the first evidence that high sweep ratio

membrane dehumidification is a promising technology for sub-freezing air cycle machine operation, and establishes that membrane-based air cycles are best-suited for relatively low altitude applications with low bleed flow rates. Beyond this initial investigation, many more architectures could be considered that require re-design of many system components.

In addition to these extensions of the current work, there are many known limitations in the capabilities of the presented component and subsystem models to accurately represent the dynamics and impacts of phase change within sub-freezing air cycle machines. In particular, the best way to improve the fidelity of the approach would be to develop a custom MATLAB® Simscape™ domain that can track liquid and solid phases of water, in addition to the current vapor tracking capability. This would enable tracking of the quantity and accumulation of phase change products, i.e. condensate and ice/frost, across and through components. In particular, liquid tracking would enable the development of a high-pressure water separator and ice tracking would naturally lend to development of models for desublimation in the air flow itself (i.e., snow rather than frost growth on a surface). Further, many components are based on generally accepted models of idealized behavior, and could be improved through the creation of custom components incorporating higher fidelity formulations.

Appendix A: Absolute Comparisons of Predicted Frost Growth

A.1 Flat Plate

For the chosen density expressions, the predicted frost thickness values were calculated for the operating conditions and each elapsed time corresponding to the experimental data points. Following the work of Leoni et al., a qualitative comparison via demonstration cases from the 1997 experimental data of Lee et al. and Piucco was conducted [9, 17, 100]. The comparison consists of three cases - one based on low/high velocity, the next on low/high relative humidity, and the final on a range of wall temperature values. For each of these cases, all other experimental parameters are held constant. A summary of the test conditions for each case is shown in Table A.1. For the proposed solution and three selected frost density expressions, the frost thickness is calculated for the given test conditions. The results for the velocity, relative humidity, and wall temperature cases are shown in Figures A.1, A.2, and A.3 respectively.

Case	T_a [$^\circ$ C]	T_w [$^\circ$ C]	RH [%]	u_a [m/s]
Velocity	25	-15	70	0.5, 2.0
Relative humidity	25	-15	50, 80	1.0
Wall temperature	16	-4, -8, -12, -16	80	1.0

Table A.1: Absolute comparison test conditions from flat plate database.

Figure A.1 shows the velocity case results. For the low velocity test conditions, the proposed model seems to agree well with all three density expressions with the closest agreement from the Yang and Lee density. On the other hand, the high velocity case shows more significant deviation by the Leoni et al. density and the best agreement with the Hermes et al. density. The proposed model adheres to the trend that thicker frost grows under higher velocity conditions for all density expressions.

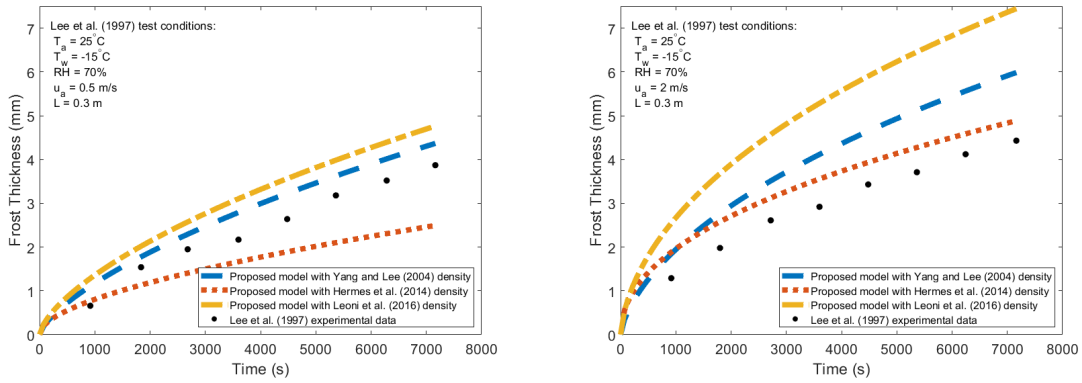

Figure A.1: Absolute comparison of flat plate frost thickness predictions for different densities: velocity case. Low velocity (left) and high velocity (right).

The relative humidity case results are shown in Figure A.2. Unlike the velocity case, the Hermes et al. density shows the best agreement for both the low and high relative humidity conditions. Again, the proposed model for each density expression follows the trend that thicker frost grows under higher humidity conditions. Unlike other frost thickness models, it does not seem that higher relative humidity leads to less spread in the results; from this qualitative comparison for these test conditions, it seems that the spread is greatest for the high relative humidity conditions.

The wall temperature results in Figure A.3 show the behavior of the proposed model with each density expression over a range of wall temperature values. For the Yang and Lee density, it is clear that the calculated values do not match well until quite late in the frost growth process. The other two density expressions yield results which are in better

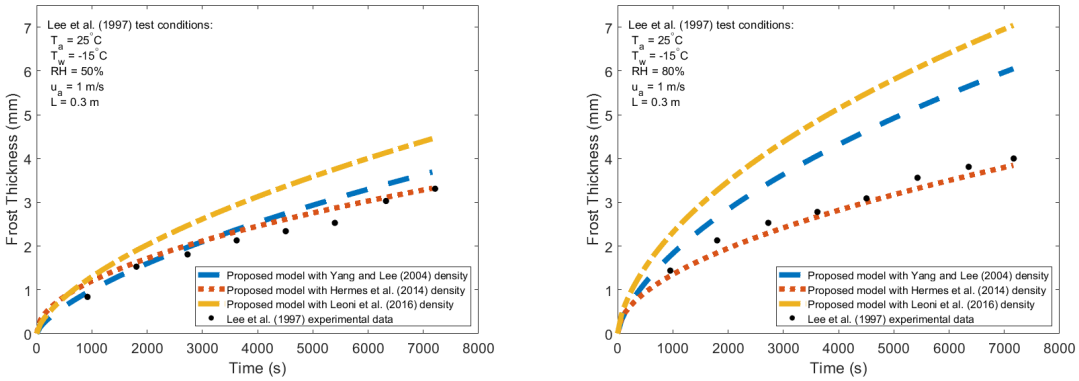

Figure A.2: Absolute comparison of flat plate frost thickness predictions using proposed model with different densities: relative humidity case. Low relative humidity (left) and high relative humidity (right).

agreement during the early frost growth period, with the Hermes et al. density giving the best results throughout. Also, the Leoni et al. density expression yield results which are quite spread throughout the frost growth process - early in the process, the calculated frost thickness is less than it should be, but later in the process the thickness is overestimated. Remark that the Piucco (2008) dataset is not included in the database used for quantitative comparison due to a lack of experimental result resolution; values were extracted in bulk and cannot be appropriately sorted. However, comparison with these results demonstrates well the behavior of the proposed solution over a range of wall temperatures.

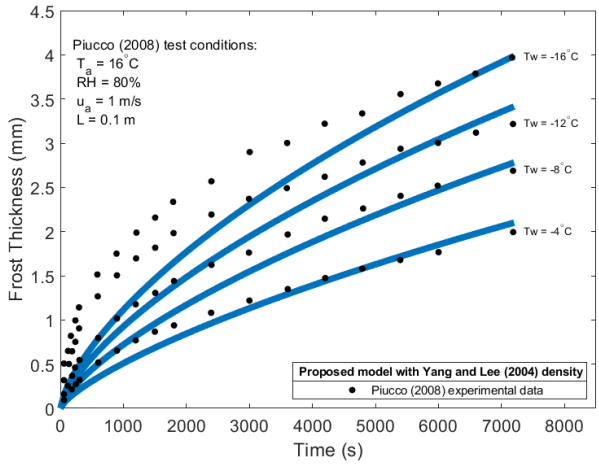

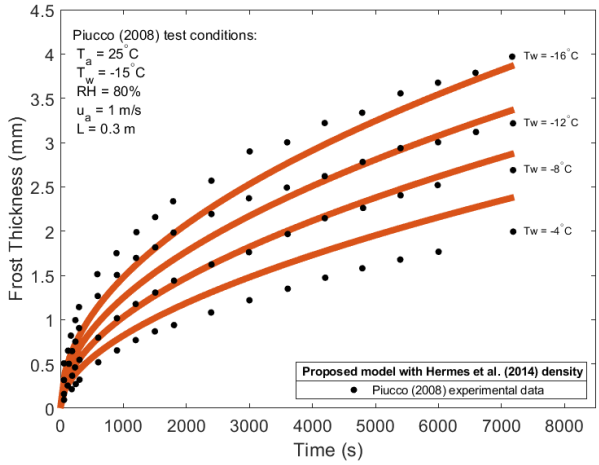

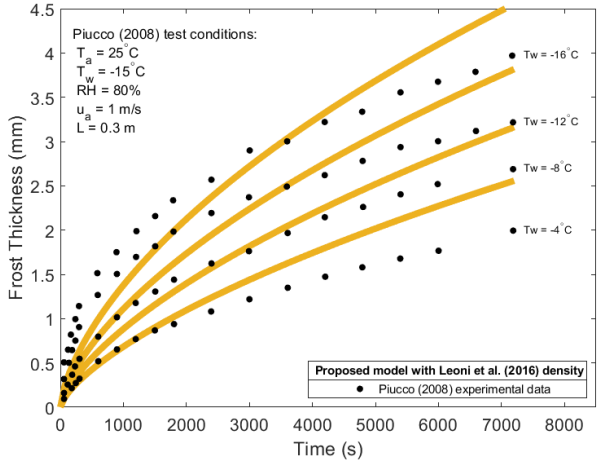

Figure A.3: Absolute comparison of flat plate frost thickness predictions using proposed model with different densities: wall temperature case.

A.2 Parallel Flat Plates

For the chosen density expressions, the predicted frost thickness values were calculated for the operating conditions and each elapsed time corresponding to the experimental data points. Following the work of Leoni et al., a qualitative comparison via demonstration cases from the experimental data of O'Neal and Tree and Ostin and Andersson was conducted [15, 20]. The comparison consists of three cases - one based on intermediate/high velocity, the next on low/high relative humidity, and the final on a range of wall temperature values. For each of these cases, all other experimental parameters are held constant. A summary of the test conditions for each case is shown in Table A.2. For the proposed solution and three selected frost density expressions, the frost thickness is calculated for the given test conditions. The results for the velocity, relative humidity, and wall temperature cases are shown in Figures A.4, A.5, and A.6 respectively.

Case	T_a [° C]	T_w [° C]	RH [%]	u_a [m/s]
Velocity	6	-5	65	2.2, 4.9
Relative humidity	21	-11	31, 72	3.0
Wall temperature	7	-5, -8, -12	65	2.9

Table A.2: Absolute comparison test conditions from parallel plate database.

Figure A.4 shows the velocity case results for the chosen run from the parallel plate database. For the low velocity test conditions, the proposed model agrees best with the Hermes et al. density with the Leoni et al. and Yang and Lee densities underestimating the frost thickness. On the other hand, the high velocity case shows significant overestimation from the Hermes et al. density and very good agreement from both the Yang and Lee and Leoni et al. densities. The proposed model adheres to the trend that thicker frost grows under higher velocity conditions for all density expressions.

The relative humidity case results for the parallel plate data are shown in Figure A.5. Much like the high velocity case, the predicted frost thickness is over-estimated for the

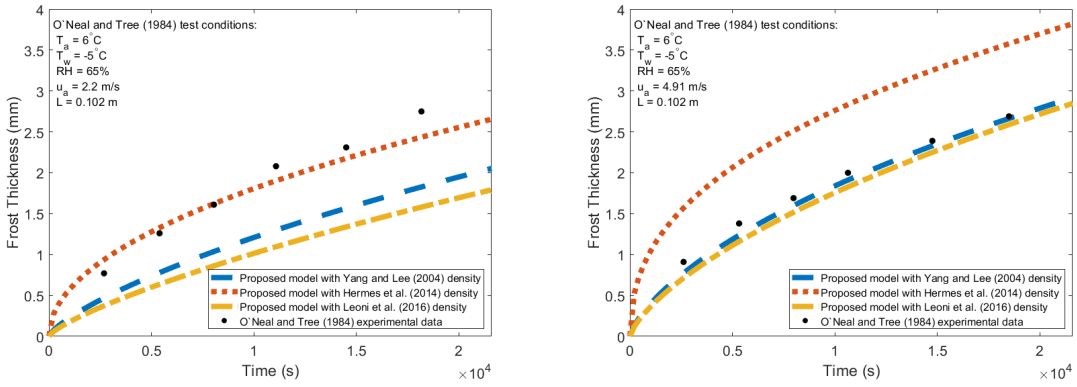

Figure A.4: Absolute comparison of parallel plate frost thickness predictions for different densities: velocity case. Low velocity (left) and high velocity (right).

low relative humidity case when using the Hermes et al. density. Good agreement is shown by predictions using both the Yang and Lee and Leoni et al. densities. The high relative humidity case shows over-prediction from all three density expressions. Again, the proposed model for each density expression follows the trend that thicker frost grows under higher humidity conditions.

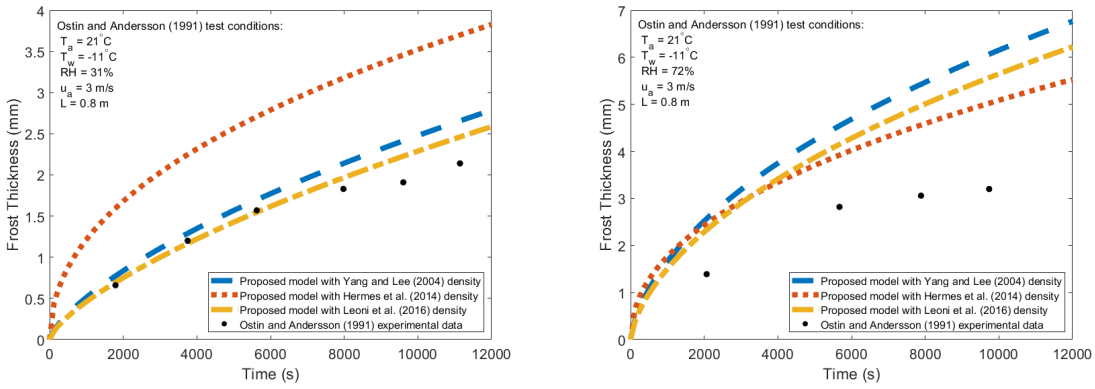

Figure A.5: Absolute comparison of parallel plate frost thickness predictions using proposed model with different densities: relative humidity case. Low relative humidity (left) and high relative humidity (right).

The wall temperature results corresponding to points from the parallel plate database shown in Figure A.6 present the behavior of the proposed model with each density expres-

sion over a range of wall temperature values. For both the Yang and Lee and Leoni et al. density expressions, the calculated values agree quite well throughout the frost growth process. The Hermes et al. density overestimates the frost thickness in every case.

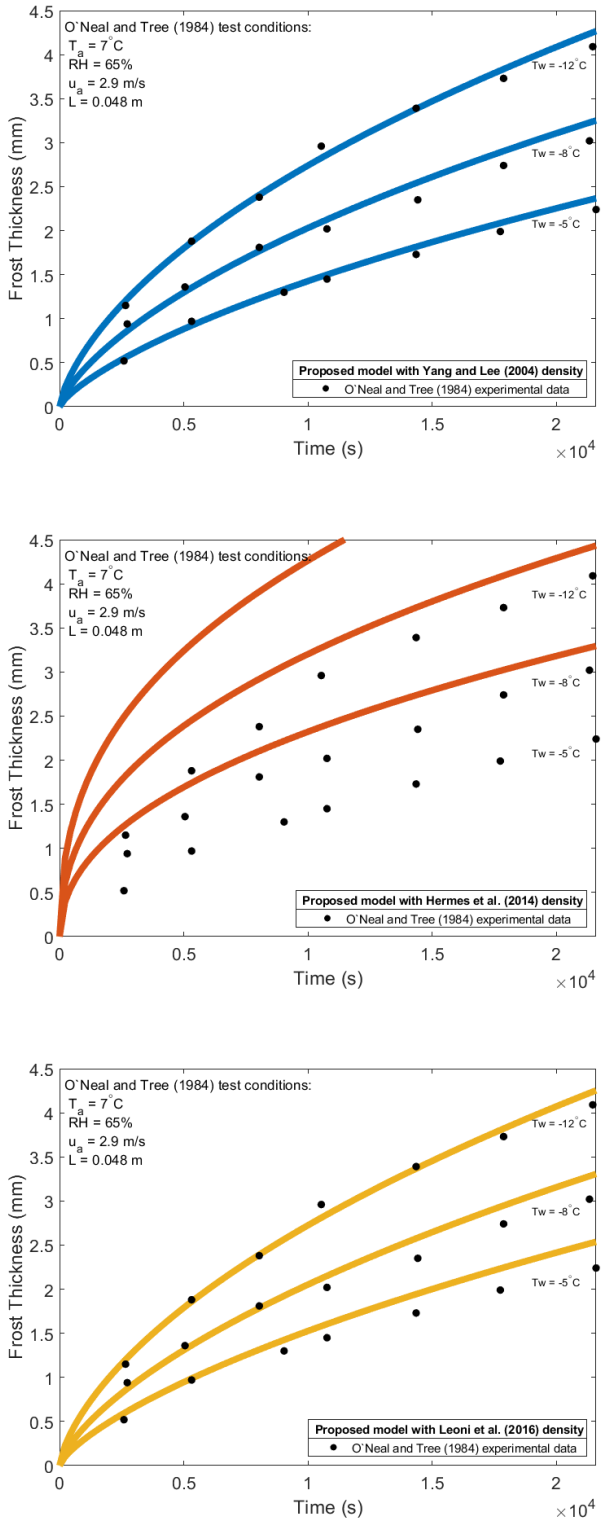

Figure A.6: Absolute comparison of parallel plate frost thickness predictions using proposed model with different densities: wall temperature case.

Appendix B: Isothermal Membrane Dehumidifier Verification

Considering that the isothermal membrane dehumidifier formulation matched that of Yang et al., several sets of simulations were run at their membrane geometry and operating conditions to verify the models behavior [41]. For all simulation results shown here, the feed temperature, humidity ratio, sweep ratio, and sweep outlet pressure are fixed at 338.15 K, 21 g/kg, 20%, and atmospheric pressure (101.325 kPa) respectively. The membrane permeability, fiber outer diameter, fiber inner diameter, shell inner diameter, packing fraction, and length were 1.2×10^{-12} kg/m·s·Pa, 0.6 mm, 0.3 mm, 80 mm, 0.495, and 640 mm respectively. The test model that was run used product sweep with a fixed sweep ratio, as shown in Figure B.1.

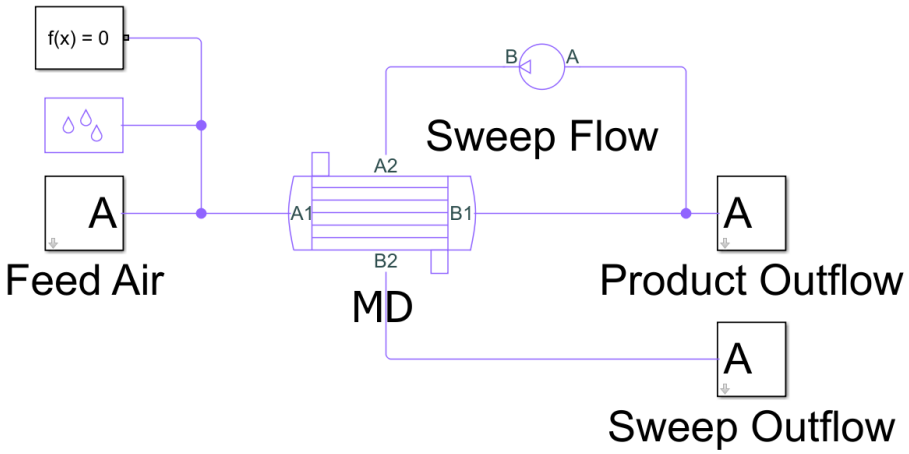

Figure B.1: Test model for isothermal membrane dehumidifier using product sweep.

First, a study to determine the appropriate number of discrete segments was conducted for varying feed flow rates and pressures. Figure B.2 shows the results, indicating that 20 segments is sufficient as there is less than 2% difference when compared within 50 segments. This agrees well with Figure 4 of Yang et al. [41]. The local mass transfer characteristics over various operating conditions are shown in Figures B.3, B.4, and B.5. All of the simulation runs show good agreement when compared with Figures 11, 12, and 13 by Yang et al. [41]. For the results shown in Figure B.3 the feed mass flow rate is fixed at 50 kg/hr.

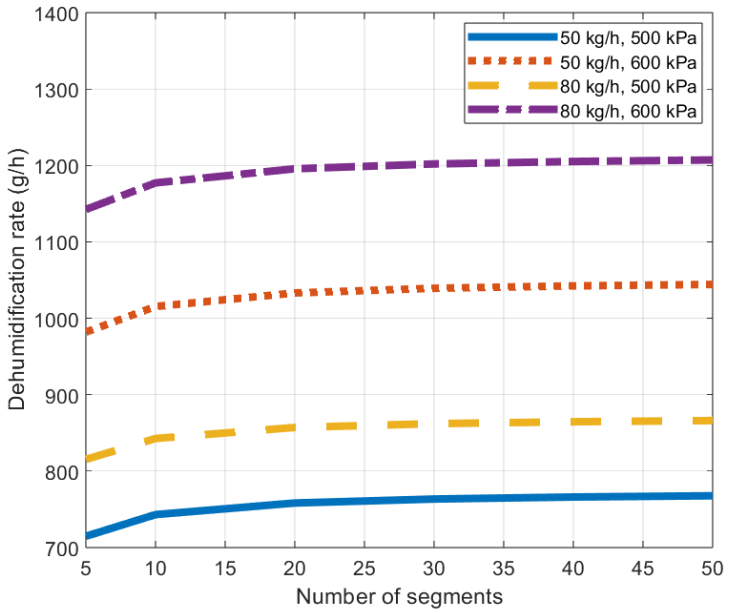

Figure B.2: Convergence of dehumidification rate for various operating conditions over a range of discretized membrane segments.

Generally, the water vapor flux is shown in increase with increased feed mass flow rate and pressure. As water vapor is moved from the feed side to the permeate/sweep side, its humidity ratio decreases, and the corresponding increase on the other side is observed. Moreover, mass transfer is maintained despite the fact that the sweep side humidity ratio is everywhere greater than the feed side; this is due to a maintained partial pressure difference, due to the elevated feed side pressure. For a more detailed discussion of the local

mass transfer characteristics for each case, refer to Yang et al. [41]. Figure B.6 shows the calculated feed side pressure drop - which is used to set the back pressure for each run - as a function of feed mass flow rate and pressure. Again, this shows good agreement with Figure 8 from Yang et al. [41].

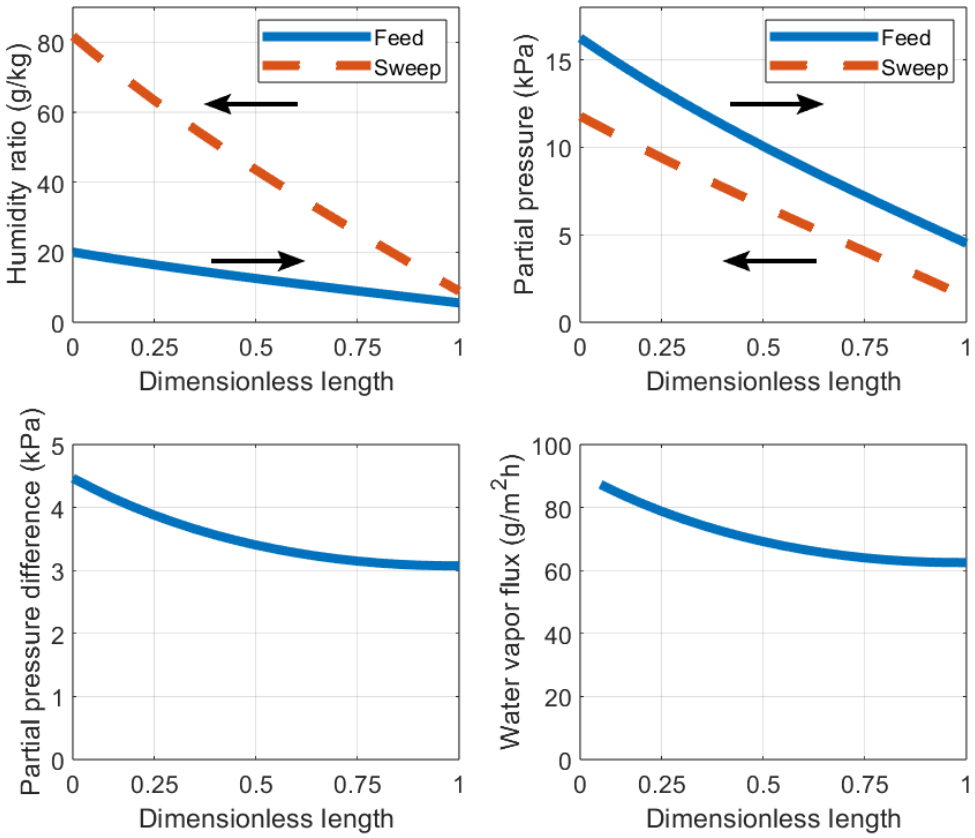

Figure B.3: Distribution profiles of humidity ratio, partial pressure, partial pressure difference, and mass transfer flux, with arrows representing flow direction along each side.

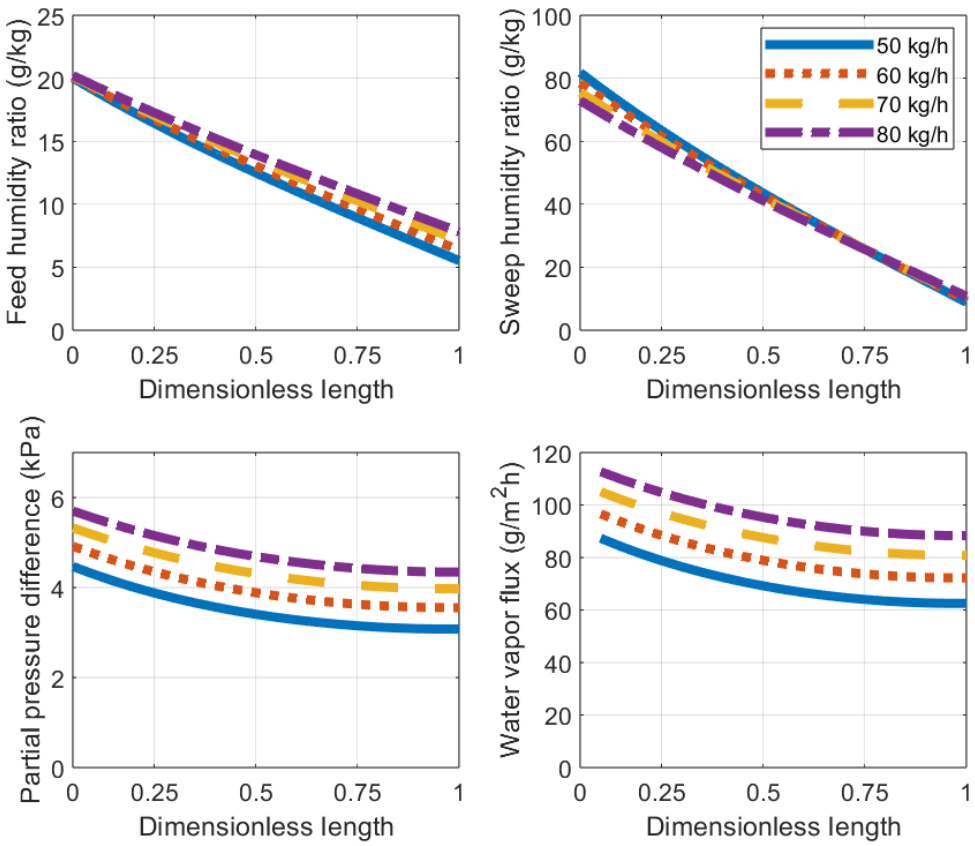

Figure B.4: Distribution profiles of humidity ratio, partial pressure, partial pressure difference, and mass transfer flux at various feed mass flow rates.

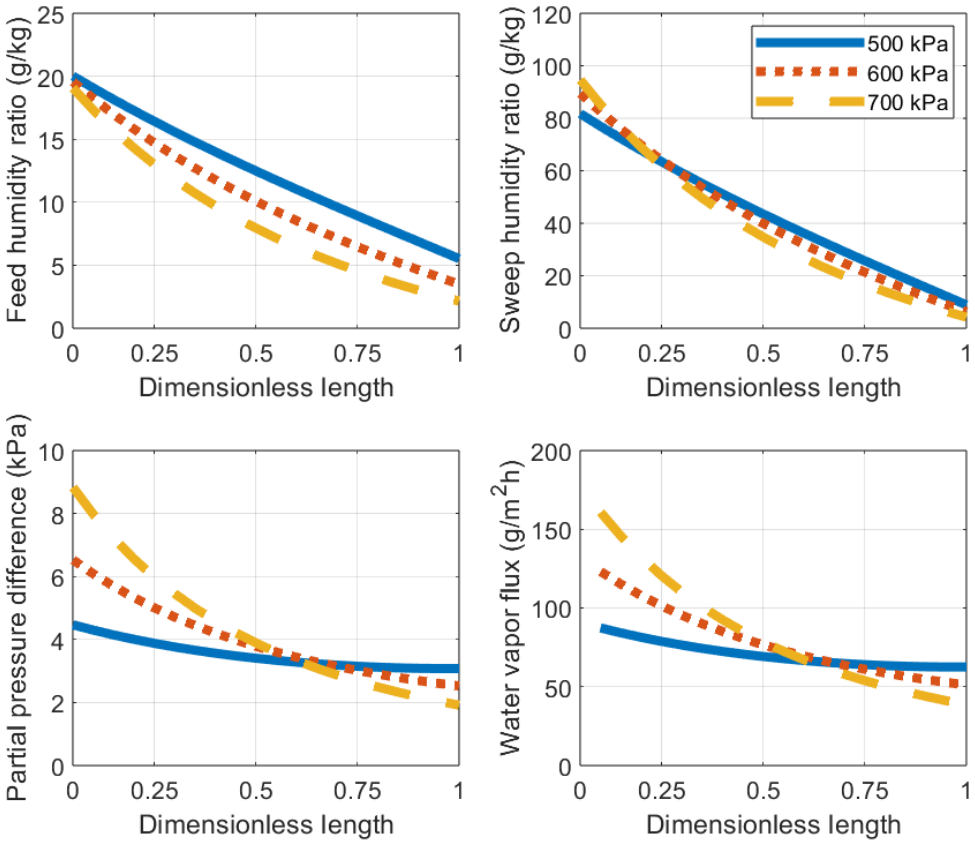

Figure B.5: Distribution profiles of humidity ratio, partial pressure, partial pressure difference, and mass transfer flux at various feed pressures.

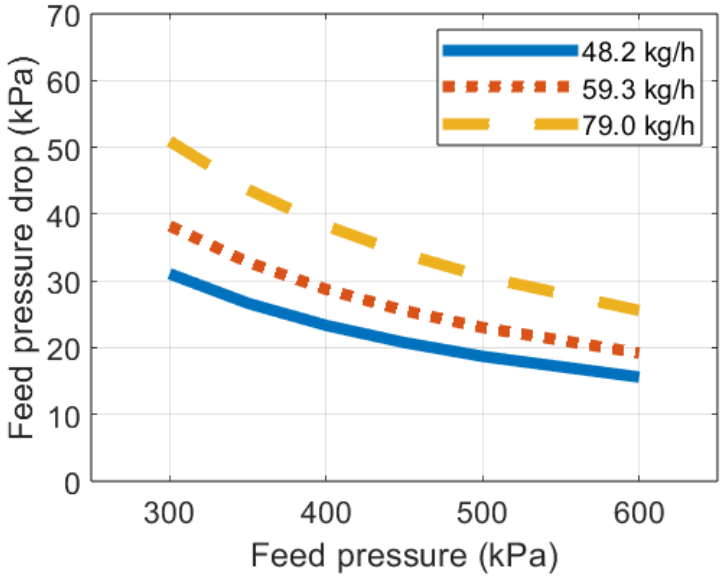

Figure B.6: Feed side pressure drop as a function of feed mass flow rate and feed pressure.

Appendix C: Modeling Investigations of Isothermal Membrane Dehumidifier

Even with the in-depth understanding of the local mass transfer characteristics of the membrane dehumidifier module, there are certain material and manufacturing details that are not represented in the current formulation. In particular, the packing fraction is known to monotonically increase along the flow direction to create the largest partial pressure difference at the feed side inlet [48]. Further, the potential dehumidification performance for future material advancements is shown by exercising the model with increasing membrane water vapor permeability. The range of permeabilities tested represent the material capabilities that are currently in production at scale, on the cutting edge of material science, and in the far future assuming continued research and improvement. The flow orientation of the module is also studied. Overwhelmingly, membrane modules are manufactured to be counter-flow mass exchange devices due to their increased dehumidification performance over a parallel flow orientation. This is demonstrated and quantified for better understanding of manufacturing practices. Finally, two further verification studies to build on those in Appendix B are conducted. The variation of dehumidification performance is shown first for varying sweep ratio, then for varying feed humidity ratio.

Following the results in Appendix B, for all simulation results shown here, the feed temperature, humidity ratio, sweep ratio, and sweep outlet pressure are fixed at 338.15 K, 21 g/kg, 20%, and atmospheric pressure (101.325 kPa) respectively, unless state otherwise. Similarly, the membrane permeability, fiber outer diameter, fiber inner diameter, shell inner

diameter, packing fraction, and length were 1.2×10^{-12} kg/m·s·Pa, 0.6 mm, 0.3 mm, 80 mm, 0.495, and 640 mm respectively, unless stated otherwise.

C.1 Constant vs. Axially-Varying Packing Fraction

First, the effects of varying the packing fraction was studied with a constant sweep ratio of 20% and feed temperature and humidity ratio of 300 K and 3 g/kg respectively. Reviewing the manufacturing process of the membrane dehumidifiers under consideration, it is known that the packing fraction is not constant; rather, it monotonically increases along the longitudinal axis of the module [48]. This axial variation of the packing fraction allows for better control of the shell-side flow direction. Moreover, it better utilizes the permeation characteristics of the membrane since the feed side inlet, which has the highest partial pressure, will enter the MD module at its lowest packing density [48]. To study the effects of a varying vs. constant packing fraction, the developed component was modified such that the packing fraction within the i^{th} discretized segment was given by:

$$\phi_i = \phi_{min} + \frac{\phi_{max} - \phi_{min}}{N-1}(i-1) \tag{C.1}$$

where N is the number of segments and ϕ_{min} and ϕ_{max} are the minimum and maximum packing densities, with the minimum located at feed side inlet and increasing along the feed side flow direction. With all of this, the constant packing fraction component was simulated under the defined operating conditions with $\phi = 0.5$ and compared to runs of the MD component with ϕ_{min} ranging from 0.2 to 0.4 and ϕ_{max} ranging from 0.6 to 0.8.

The local mass transfer results are shown in Figure C.1. The feed and sweep humidity ratios along the length of the MD show that the varying packing density affects the local rate of mass transfer, leading to more gradual changes in water vapor concentration. In all cases, the partial pressure difference across the membrane and the water vapor flux decrease as the dehumidification process progresses. However, the trend is more extreme when the packing density varies, with the highest partial pressure difference and thus the highest flux

for the scenario with ϕ_{min} = 0.2 and the lowest when ϕ_{max} = 0.8. Recall though that the actual rate of mass transfer of the water vapor is dictated by the product of the mass flux and the mass transfer area, and when the packing fraction is less there are less fibers and thus a proportionally lower mass transfer area. Hence, the overall dehumidification rate when incorporating axial packing density variation was within 1.5% of the constant case for all tested ranges, so the assumption of a constant packing fraction in the current formulation is reasonable.

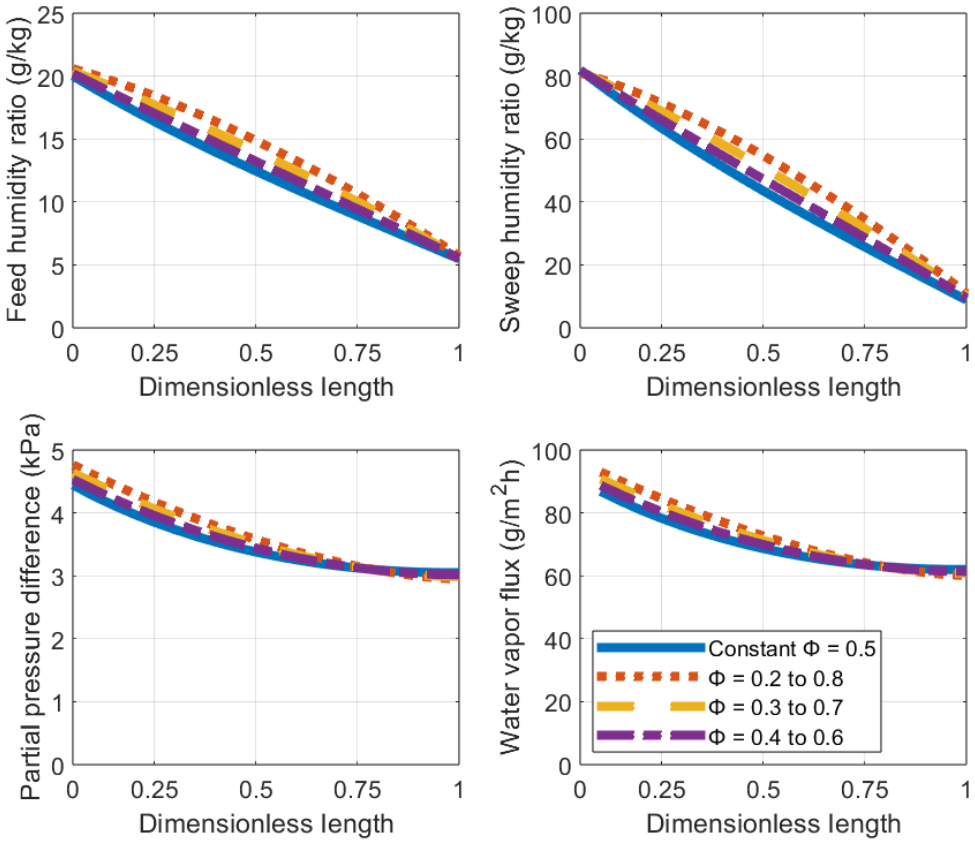

Figure C.1: Effects of axial variation of packing fraction on local mass transfer characteristics compared to constant case.

C.2 Varying Permeability

As the specific value of permeability for polysulfone can be provided as a range encompassing an order of magnitude [49], and moreover the units and measures for permeability are often not standardized (e.g., barrer units, which are widely used in industry but have no official definition from the National Institute of Standards and Technology [52]), a range of membrane permeabilities were tested using the product sweep architecture to study the effects on local mass transfer characteristics. For this study, the permeability was set to 1.2, 3, and 5 $\times 10^{-12}$ kg/m·s·Pa. This range was chosen to represent materials currently used in membrane module production, the cutting edge of feasible membrane materials, and the future potential with improved material properties. More specifically, a permeability of 1.2 $\times 10^{-12}$ kg/m·s·Pa was used by Yang et al. in their recent high-pressure membrane model, which showed good agreement with their experimental results [41]. In the literature, the upper bounds of water vapor permeability exist around 450,000+ barrer, approaching 500,000 - this is roughly equivalent to 3 $\times 10^{-12}$ kg/m·s·Pa [58]. This range of material advancement was accomplished within the last 20 years, so it is assumed continual improvement from new membrane fabrication methods will continue to yield improved mass transfer performance, represented by the 5 $\times 10^{-12}$ kg/m·s·Pa permeability test.

The results of varying membrane water vapor permeability are shown in Figure C.2. From this, it is clear that an increased permeability results in increased water vapor flux and increased dehumidification performance. With current material capabilities, the feed side outlet humidity ratio is reduced to 6.2 g/kg from 10 g/kg at the inlet. With improved materials, this is shown to decrease to 2.3 g/kg for the highest permeability case. The rapid vapor movement from feed to permeate side is reflected in the lower partial pressure differences at higher permeabilities - these do not indicate poor mass transfer performance, but considering the high feed humidity ratio instead indicate that the vast majority of the water vapor moves from feed to sweep side in the entry length of the module, corresponding to the rapid increase in the sweep side humidity ratio. Along with this, the dehumidification

rate was also observed to increase from 758.3 g/h at the lowest permeability to 946.4 g/h at the highest.

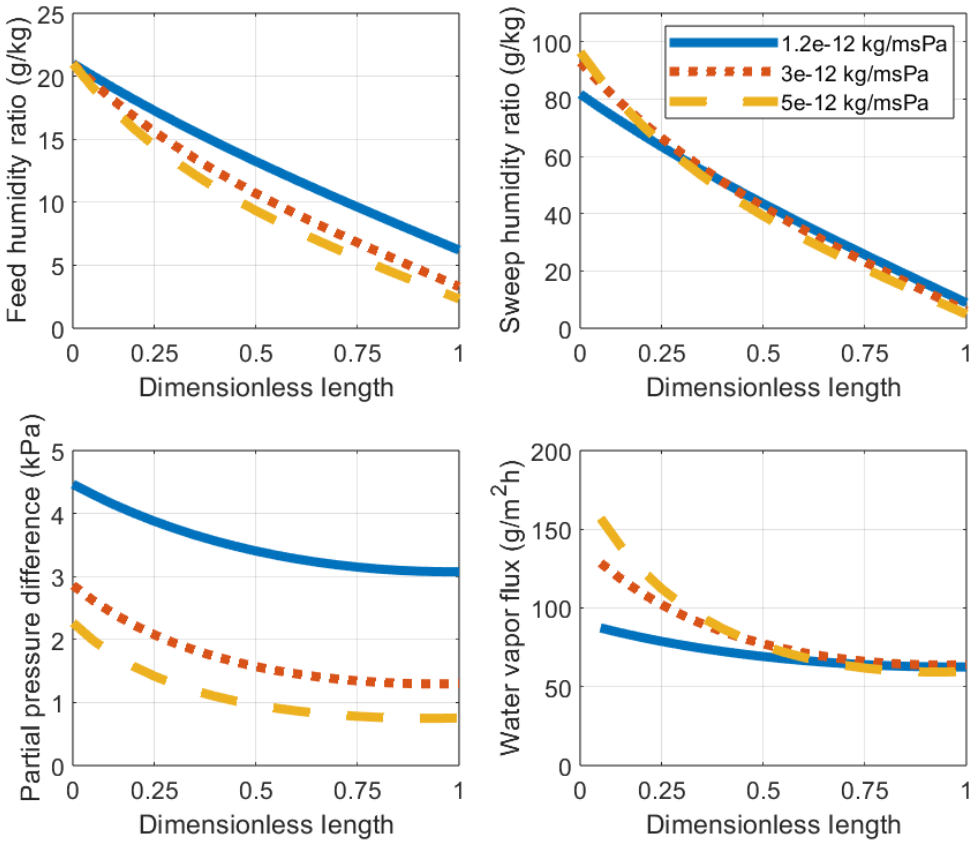

Figure C.2: Effects of varying water vapor permeability of membrane on local mass transfer characteristics.

C.2.1 Counter-flow vs. Parallel Flow

For completeness, a discretized MD component model with parallel flow was developed and exercised under product sweep conditions. The formulation remains the same for these models; the only difference is the location of the sweep inlet and outlet. In the cross-flow case, the sweep inlet is located at the same axial location as the product outlet. For the parallel flow orientation, the sweep inlet is located at the same axial location as the product

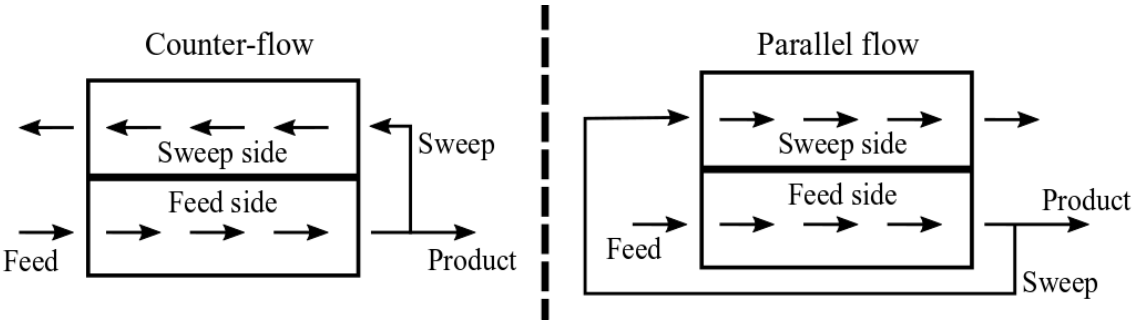

Figure C.3: Counter-flow vs. parallel flow orientation.

inlet; Figure C.3 illustrates this.

Figure C.4 shows the results of running the product sweep architecture with both the counter-flow and parallel flow orientations. From the local mass transfer characteristics, it is clear that the counter-flow orientation results in a sustained partial pressure difference, and thus a decreasing but positive vapor flux along its length. In contrast, the parallel flow orientation yields a significantly higher initial partial pressure difference because the most humid air, the feed inlet, is exchanging mass with the least humid air, the sweep inlet (which has the same conditions as the feed outlet, or product air). However, this partial pressure pressure difference drops to zero as concentration equilibrium is reached, thus reaping no mass transfer benefit from the latter fiber/module length. Consequently, the dehumidification rates of the counter-flow and parallel flow MDs are 758.3 and 469.0 g/h respectively. Therefore, it is evident that the counter-flow orientation will more effectively dry the feed air.

The mass transfer behavior is shown even more clearly by the partial pressure on each side in Figure C.5. The counter-flow MD maintains a higher partial pressure on the feed side than the sweep side along the whole length, while the partial pressures in the parallel flow MD tend to same value. Following the analogy between heat and mass transfer, remark that the trends for partial pressure in the MD are the same as for temperature, the driving force of heat transfer, in counter-flow and parallel flow heat exchangers [101].

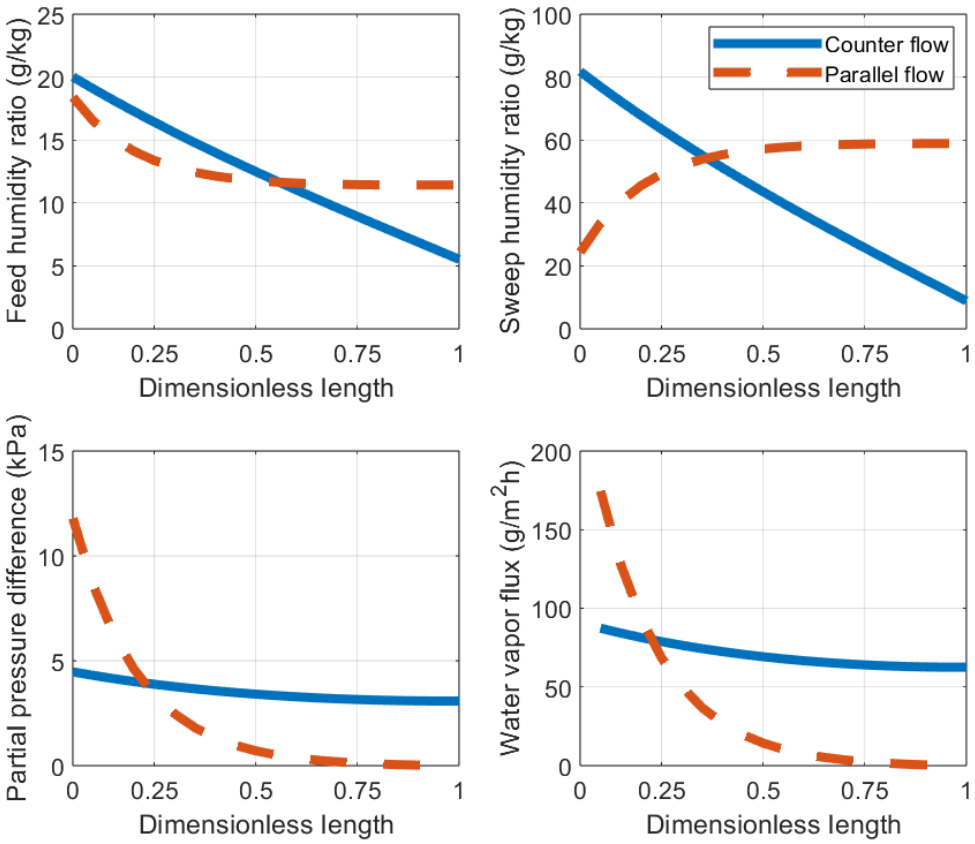

Figure C.4: Comparison of counter-flow vs parallel flow sweep orientation on local mass transfer characteristics.

C.3 Varying Sweep Ratio

Figure C.6 shows the results for exercising the product sweep architecture over a range of sweep ratios and feed mass flow rates. From the results, it is clear that a higher sweep ratio results in both higher dehumidification rate and efficiency. The effect of changing mass flow rate is opposite though. Since the dehumidification rate is dependent on the partial pressure, which will be higher for higher flow rates, it increases. On the other hand, the efficiency measures the vapor removed compared to what is supplied and this decreases as the flow rate increases because the moist air spends less time in the membrane dehumidifier, resulting in less of the supplied vapor removed. These results show good agreement with a

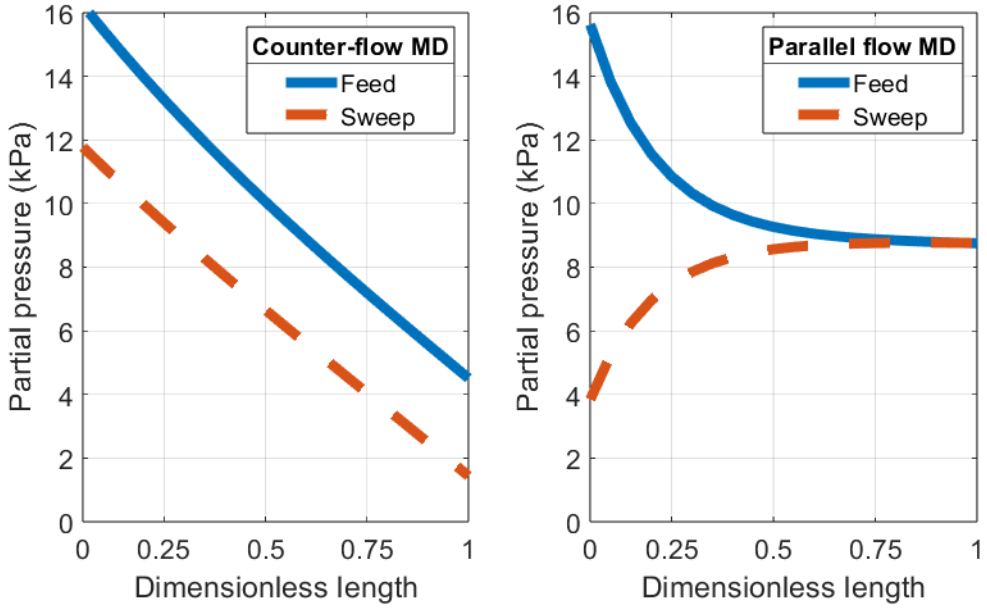

Figure C.5: Partial pressure on each side of membrane for parallel vs. counter-flow MD orientation.

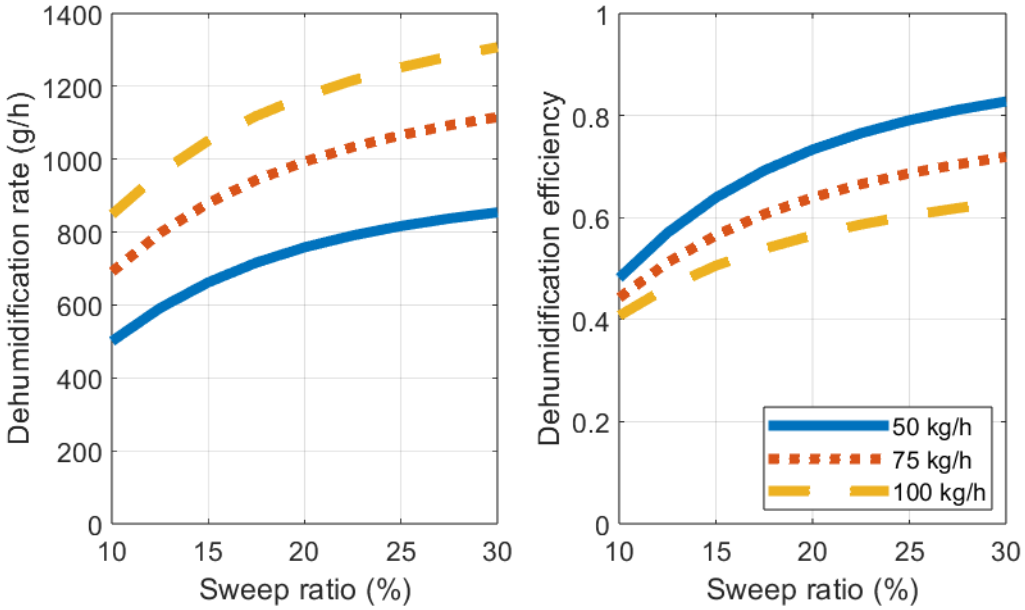

Figure C.6: Effect of varying sweep ratio for different mass flow rates on dehumidification rate and dehumidification efficiency.

similar investigation by Yuan et al. [84].

C.4 Varying Feed Humidity

The eventual application of the this component model is for aircraft environmental control systems, to be incorporated in addition to the traditional condensation-based water separator approach. To be placed downstream of the high pressure water separator, it follows that the typical operating conditions of the MD will be a lower humidities than ambient and potentially over a range of feed temperatures. To study the effects of the feed humidity, which may vary over the course of an aircraft mission, a study was run for feed humidity varying from 5 to 20 g/kg. At the fixed feed temperature of 338.15 K, these humidity values are all below saturation.

The local mass transfer results of the feed humidity ratio study are shown in Figure C.7. As the feed humidity ratio increases, the dehumidification proceeds at similar rates, with the membrane capable of producing the driest air for the lowest feed humidity condition. The elevated feed humidity ratio causes a increased partial pressure difference across the membrane for the entire length of the MD, and subsequently an increased water vapor flux. Accordingly, the dehumidification rate increases with the feed humidity ratio, with mass transfer capacities of 177.0, 356.7, 538.2, and 721.4 g/h respectively.

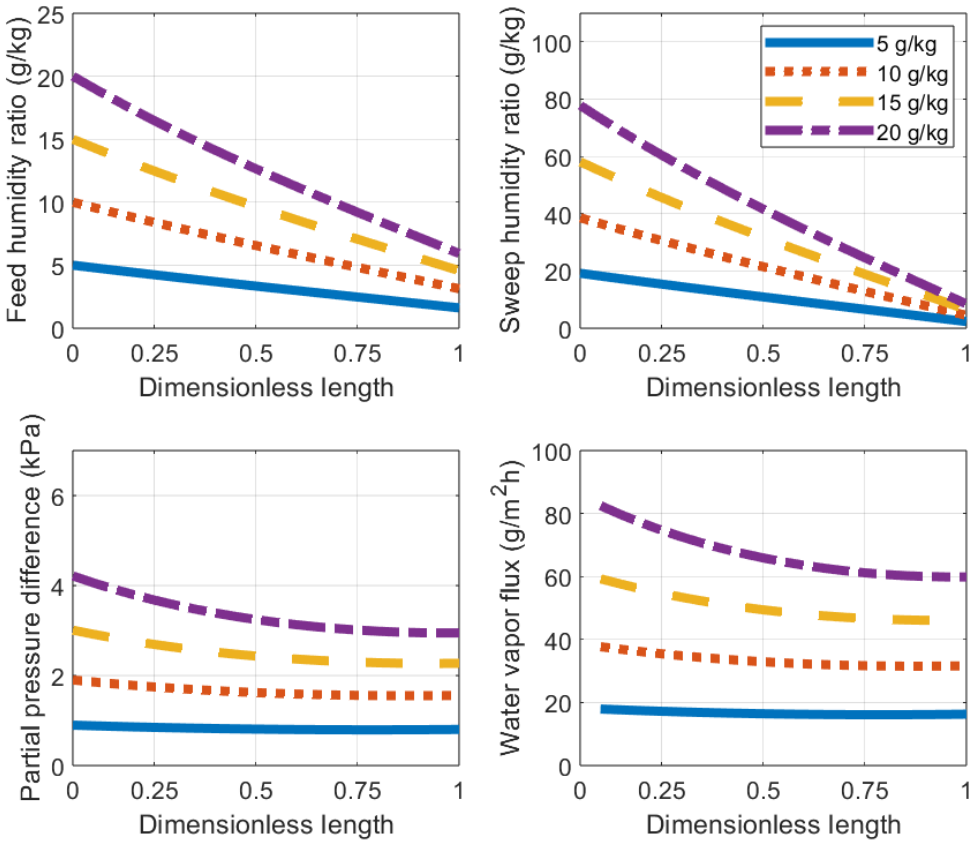

Figure C.7: Local mass transfer characteristics at various feed humidity ratios.

Appendix D: Detailed Membrane Dehumidifier Module Designs

Tables D.1 and D.2 show the module design parameters and corresponding performance metrics for the 17 points that constitute the identified Pareto efficient set of membrane module designs for a permeability of 1.2 $\times 10^{-12}$ kg/m·s·Pa, corresponding to commercially available materials currently used in membrane module production. The Monte Carlo search that resulted in this Pareto set consisted of 1000 constrained model evaluations under conditions relevant to an aircraft air cycle machine. For all runs, a product sweep ratio of 20% was used as well as a feed side flow rate, temperature, pressure, and humidity ratio of 0.5 kg/s, 320 K, 575 kPa, and 10 g/kg.

d_o [mm]	d_i [mm]	D [m]	ϕ [1]	L [m]
0.5093	***0.4060***	***0.2516***	***0.4307***	***0.8264***
0.7458	0.5942	0.2167	0.5292	0.2859
0.5135	0.4071	0.2658	0.5324	0.5481
1.0954	0.7087	0.1523	0.2753	0.2695
1.1477	0.8564	0.1533	0.6427	0.2926
0.7477	0.5977	0.1561	0.4965	0.6107
0.5858	0.4467	0.1604	0.6153	0.6148
1.4583	1.0478	0.1500	0.4409	0.2872
0.5179	0.3636	0.3006	0.7512	0.3663
0.7640	0.4839	0.1565	0.5752	0.3855
0.5603	**0.4326**	**0.2255**	**0.7597**	**0.3129**
0.5617	0.4079	0.2252	0.6708	0.4748
0.5693	0.4356	0.2379	0.7179	0.4291
0.9100	0.6484	0.1740	0.3955	0.2904
0.5315	0.3825	0.2429	0.7996	0.4992
0.6662	0.5255	0.1776	0.6068	0.3066
0.7780	0.4896	0.1696	0.7087	0.3304

Table D.1: Module design parameters of Pareto set, with the highest volumetric efficiency module design in bold and highest dehumidification efficiency in italicized bold.

η [%]	V [m^3]	$\frac{\eta}{V}$ [m^{-3}]	Δp_f [kPa]	MRR [kg/h]
77.8739	***0.0411***	***25.2798***	***18.3264***	***13.9090***
31.5776	0.0105	39.9454	3.2520	5.6661
75.6510	0.0304	33.1727	8.8575	13.5149
2.6484	0.0049	7.1932	12.7195	0.4766
8.6328	0.0054	21.3229	3.0042	1.5526
32.1866	0.0117	36.7318	14.0086	5.7750
45.2837	0.0124	48.6261	21.2012	8.1143
3.2692	0.0051	8.5852	3.2329	0.5883
69.0737	0.0260	35.4322	5.2428	12.3480
14.2200	0.0074	25.5795	18.4510	2.5560
54.1648	**0.0125**	**57.7714**	**4.5983**	**9.6971**
57.1754	0.0189	40.3131	10.0755	10.2331
62.4115	0.0191	43.6445	6.0228	11.1644
9.2434	0.0069	17.8565	7.2006	1.6623
62.6144	0.0231	36.0824	8.8358	11.2005
31.2372	0.0076	54.8538	5.9088	5.6052
16.3471	0.0075	29.2009	10.8176	2.9377

Table D.2: Performance metrics of Pareto set, with the highest volumetric efficiency module design in bold and highest dehumidification efficiency in italicized bold.

Appendix E: Extended Component Formulations

E.1 Turbomachinery

The foundation of an air cycle machine is its turbomachinery - an axial flow turbine and compressor - which are used to extract power from the flow and then use that power to compress the incoming flow respectively. The equations supporting each of these components are presented in the following subsections.

E.1.1 Compressor

The compressor model represents simplified air compressor behavior where power from a mechanical rotational network is used to drive the moist air flow of the air cycle. In this simplified model, the compressor map is scaled based on a known nominal operating condition and its shape is approximated by empirical coefficients. The nominal operating condition is defined by a design pressure ratio, corrected mass flow rate, and corrected shaft speed, denoted by $PR_{des}, \dot{m}_{corr,des}$, and $\omega_{corr,des}$. This nominal operating condition corresponds to reference pressure, temperature, and relative humidity conditions of p_{ref}, T_{ref}, and RH_{ref} respectively. In addition, the compressor has mechanical and polytropic efficiencies of η_{mech} and η_{poly}.

For a given inlet flow rate, temperature, and pressure of $\dot{m}_{in}, T_{in}$, and p_{in} and shaft speed ω, the outlet conditions can be found by first correcting to the reference conditions

as:

$$\dot{m}_{corr} = \dot{m}_{in}\sqrt{\left(\frac{R_{in}T_{in}}{p_{in}}\right)\left(\frac{R_{ref}T_{ref}}{p_{ref}}\right)} \tag{E.1}$$

$$\omega_{corr} = \omega\sqrt{\frac{R_{ref}T_{ref}}{R_{in}T_{in}}} \tag{E.2}$$

where R_{in} and R_{ref} are the specific gas constants found at the inlet and reference conditions respectively. Then, the corrected conditions are scaled to the design conditions as:

$$PR_{scaled} = \frac{PR - 1}{PR_{des} - 1} \tag{E.3}$$

$$\dot{m}_{corr,scaled} = \frac{\dot{m}_{corr}}{\dot{m}_{corr,des}} \tag{E.4}$$

$$\omega_{corr,scaled} = \frac{\omega_{corr}}{\omega_{corr,des}} \tag{E.5}$$

With this, the inlet conditions have been scaled and corrected to reflect the actual operation of the compressor under the given conditions. The shaft torque is found as:

$$\tau = \frac{\dot{m}_{in}\Delta h_{total}}{\eta_{mech}\omega} \tag{E.6}$$

where $\Delta h_{total} = h_{t,out} - h_{t,in}$ is the change is specific total enthalpy. Conservation of mass and energy are enforced as:

$$\dot{m}_{in} + \dot{m}_{out} = 0 \tag{E.7}$$

$$\Phi_{in} + \Phi_{out} + P_{fluid} = 0 \tag{E.8}$$

where $P_{fluid} = \dot{m}_{in}\Delta h_{total}$ is the power added to the fluid. The polytropic compression process relates the work done by the compressor to the pressure ratio as:

$$\eta_{poly}\int\frac{\Delta h_{total}}{T} = R_{in}\ln\left(PR\right) \tag{E.9}$$

where R_{in} is the specific gas constant at the inlet conditions, and $\Delta h_{total} = h_{out} - h_{in}$.

Due to the large changes in pressure and temperature within a compressor, its range of stable operating conditions can be characterized by a performance map. The boundaries of this map correspond to two unstable modes of behavior: surge flow and choked flow. Surge flow is characterized by a breakdown in steady flow conditions, resulting in a rapid

flow reversal. Choked flow occurs when the flow is choked within the compressor, meaning the mass flow rate is at its maximum for the given inlet conditions and discharge pressure; operating at choked conditions is characterized by increased vibration, temperature, and rapid decrease of compressor efficiency. Stable operation of axial flow compressors exists along within operational margins established to avoid these unstable modes [102–104].

A compressor map plots lines of constant corrected shaft speed as a function of pressure ratio and corrected mass flow rate. So, for a chosen shaft speed, the the variation of pressure ratio with corrected mass flow rate is established. The shape and distribution of the speed lines is determined by three curve fit coefficients, b_1, b_2, and b_3; these are provided as inputs to the compressor block [105]. For all results presented here, the map coefficients b_1, b_2, and b_3 were 1.5, 0.25, and 0.08 respectively. With these, the curve on the compressor map given along the bend of the corrected speed line is given by:

$$\dot{m}_{corr,scaled,bend} = \left(\omega_{corr,scaled}\right)^{b_2} \tag{E.10}$$

$$PR_{scaled,bend} = \left(\dot{m}_{corr,scaled,bend}\right)^{b_1} \tag{E.11}$$

Then, the value of the scaled, corrected mass flow rate on the map is given by:

$$\dot{m}_{corr,scaled,map} = \dot{m}_{corr,scaled,bend} + b_3 \left(1 - \exp\left(\frac{PR_{scaled} - PR_{scaled,bend}}{2b_3\omega_{corr,scaled}}\right)\right) \tag{E.12}$$

For a given pressure ratio, this is used to find the corresponding operational shaft speed; hence, over dynamic operating conditions, the compressor map is used to adjust the compressor behavior over the range of inlet conditions.

E.1.2 Turbine

Stodola's Law of the Ellipse is a useful method for calculating the highly nonlinear off-design extraction pressure of a compressed air turbine [98, 99]. For given nominal conditions and efficiencies, the method can be streamlined to the calculation of a proportionality

constant as:

$$K_{Stodola} = \frac{\dot{m}_{corr,des}\sqrt{R_{ref}T_{ref}}}{p_{ref}\sqrt{1 - PR_{des}^{\frac{\eta_{poly}+1}{\eta_{poly}}}}} \tag{E.13}$$

With this, the mass flow through the turbine can be found at the actual operating conditions as:

$$\dot{m} = K_{Stodola}\left(\frac{p_{in}}{R_{in}T_{in}}\right)\sqrt{1 - PR^{\frac{\eta_{poly}+1}{\eta_{poly}}}} \tag{E.14}$$

where PR is the actual pressure ratio across the turbine, determined from polytropic process calculation as was done the compressor. The polytropic turbine process relates the work done by the turbine to the pressure ratio as:

$$\eta_{poly}\int\frac{\Delta h_{total}}{T} = R_{in}\ln(PR) \tag{E.15}$$

where R_{in} is the specific gas constant at the inlet conditions. Now, the shaft torque in the turbine is given by:

$$\tau = \frac{\eta_{mech}\dot{m}_{in}\Delta h_{total}}{\omega} \tag{E.16}$$

Due to the phase change processes that can occur within the turbine, the total enthalpy change is given by $\Delta h_{total} = h_{in} - h_{work}$, where

$$h_{work} = (1 - x_w + x_{w,sat})h_{out} + (x_w - x_{w,sat})h_{pc} \tag{E.17}$$

Correspondingly, the mass and energy conservation account for phase change as well and are enforced as:

$$\dot{m}_{in} + \dot{m}_{out} - \dot{m}_{pc} = 0 \tag{E.18}$$

$$\Phi_{in} + \Phi_{out} + P_{fluid} - \Phi_{pc} = 0 \tag{E.19}$$

where $P_{fluid} = \dot{m}_{in}\Delta h_{total}$ is the shaft power.

E.2 The Effectiveness-NTU Method

The effectiveness-NTU (ϵ-NTU) method is used to calculate the rate of heat transfer in heat exchangers (HXs) when there is insufficient information to calculate the log-mean temperature difference, i.e., when the outlet conditions are unknown and must be determined from the inlet conditions. To define HX effectiveness, it is necessary to find the maximum possible heat transfer that could hypothetically be achieved in an infinitely long HX. In that case, the side with the lesser heat capacity rate would undergo the maximum possible temperature change.

Let the temperatures, mass flow rates, and heat capacities of the hot and cold sides of the heat exchanger be $T_{hot}, \dot{m}_{hot}, c_{p,hot}$ and $T_{cold}, \dot{m}_{cold}, c_{p,cold}$ respectively. Then, the heat capacity rates can be found as:

$$\begin{aligned} C_{hot} &= \dot{m}_{hot} c_{p,hot} \\ C_{cold} &= \dot{m}_{cold} c_{p,cold} \end{aligned} \tag{E.20}$$

Hence, the maximum heat transfer rate is:

$$q_{max} = \min(C_{hot}, C_{cold})(T_{hot,in} - T_{cold,in}) = C_{min}(T_{hot,in} - T_{cold,in}) \tag{E.21}$$

and so the effectiveness is defined as:

$$\epsilon = \frac{q}{q_{max}} \tag{E.22}$$

where the actual heat transfer is given by:

$$q = C_{hot}(T_{hot,in} - T_{hot,out}) = C_{cold}(T_{cold,in} - T_{cold,out}) \tag{E.23}$$

Now, for any HX, it can be shown that the $\epsilon = f(NTU, C_{ratio})$, where NTU is the number of transfer units as:

$$NTU = \frac{UA}{C_{min}} \tag{E.24}$$

and U is the overall heat transfer coefficient, A is the heat transfer area, and C_{ratio} is the

Problem Type	Prescribed Values	Calculated Values
Design Problem (Sizing Problem)	HX effectiveness Pressure drop on each side	HX length HX width HX height
Performance Problem (Rating Problem)	HX length HX width HX height	Heat transfer rate Outlet temperatures Pressure drops

Table E.1: Heat exchanger design (sizing) problem vs. performance (rating) problem.

heat capacity ratio, defined as:

$$C_r = \frac{C_{min}}{C_{max}} \tag{E.25}$$

Hence, with the knowledge of ϵ and the inlet conditions of each side of the heat exchanger, the rate of heat transfer can be found as:

$$q = \epsilon C_{min}(T_{hot,in} - T_{cold,in}) \tag{E.26}$$

All of this together can be used to find the temperatures of each side out of the HX, $T_{hot,out}$ and $T_{cold,out}$. For an unmixed, cross-flow, single pass HX, the expression for effectiveness can be expressed in terms of the number of transfer units, NTU, and heat capacity ratio, C_r, as:

$$\epsilon = 1 - exp\left(\frac{NTU^{0.22}}{C_r}\left(exp(-C_r(NTU)^{0.78}) - 1\right)\right) \tag{E.27}$$

This expression cannot be manipulated to find the number of transfer units as a function of effectiveness and heat capacity ratio, unlike other HX flow orientations [93]. Using the effectiveness-NTU approach outlined here, there are two problems that are commonly encountered; namely, the sizing (a.k.a. design) problem and the rating (a.k.a. performance) problem. These problems are summarized in Table E.1; for an in-depth procedure for solving each, refer to [101].

E.2.1 Scaling to Actual Conditions

For each side of each heat exchanger, a design temperature, T_{des}, mass flow rate, $\dot{m}_{des}$, and specific heat capacity, $c_{p,des}$ must be provided. Further, the heat transfer performance is dictated by a design heat transfer rate, Q_{des}, and a design pressure drop Δp_{des}. From the pairs of $\dot{m}_{des}$ and $c_{p,des}$, the maximum and minimum design heat capacity rates can be determined as

$$C_{min,des} = \min(c_{p1,des}\dot{m}_{1,des}, c_{p2,des}\dot{m}_{2,des} \tag{E.28}$$

$$C_{max,des} = \max(c_{p1,des}\dot{m}_{1,des}, c_{p2,des}\dot{m}_{2,des} \tag{E.29}$$

Then, the design effectiveness can be calculated as

$$\epsilon_{des} = \frac{Q_{des}}{C_{min,des} abs(T_1 - T_2)} \tag{E.30}$$

and the approximate ratio of the design heat transfer coefficients is found as:

$$\lambda = \left(\frac{\dot{m}_{2,des}}{\dot{m}_{1,des}}\right)^{4/5} \left(\frac{c_{p2,des}}{c_{p1,des}}\right)^{1/3} \tag{E.31}$$

With the design effectiveness, a root finding algorithm is used to find the corresponding number of transfer units, NTU_{des}, for the design effectiveness from Eq. E.27. Once NTU_{des} is determined, the design overall heat transfer coefficient times the heat transfer area is given by:

$$UA_{des} = NTU_{des} C_{min,des} \tag{E.32}$$

With the design parameters fully determined, it is next necessary to find C_{min} and C_{max} from the actual operating conditions. Then, the actual values of UA and NTU are scaled

to the actual operating conditions as:

$$\dot{m}_{1,rat} = \left(\frac{\dot{m}_1}{\dot{m}_{1,des}} \right)^{4/5} \tag{E.33}$$

$$\dot{m}_{2,rat} = \left(\frac{\dot{m}_2}{\dot{m}_{2,des}} \right)^{4/5} \tag{E.34}$$

$$UA = \frac{UA_{des}}{\frac{1}{\dot{m}_{1,rat}(1+1/\lambda)} + \frac{1}{\dot{m}_{2,rat}(1+1/\lambda)}} \tag{E.35}$$

$$NTU = \frac{UA}{C_{min}} \tag{E.36}$$

and the actual effectiveness ϵ can be calculated using Eq. E.27. Finally, the actual rate of heat transfer from side 1 to side 2 is given by:

$$Q = \epsilon C_{min}(T_{1,in} - T_{2,in}) \tag{E.37}$$

Remark that the inlet temperatures are used to calculate the heat transfer so that the internal temperatures represent the flow characteristics after heat exchange has taken place. The actual pressure drop on each side of the heat exchanger is given by:

$$\Delta p_1 = \frac{\Delta p_{des}}{2\dot{m}_{1,des}^2} \dot{m}_1^2 \tag{E.38}$$

$$\Delta p_2 = \frac{\Delta p_{des}}{2\dot{m}_{2,des}^2} \dot{m}_2^2 \tag{E.39}$$

E.3 Ambient and Ram Conditions

The temperature of the ram air, T_{ram}, is assumed to be at the ram duct recovery temperature, which can be calculated for a given Mach number M as:

$$T_{rec} = T_{atm} \left(1 + \frac{\gamma - 1}{2} M^2 \right) \tag{E.40}$$

where $\gamma = 1.401$ is the ratio of specific heats, constant for the assumed low, constant speed of M = 0.2. The ram pressure is equal to the total pressure, or the sum of the ambient and dynamic pressures as:

$$p_{tot} = p_{amb} + \frac{1}{2} \rho_{amb} u^2 \tag{E.41}$$

where ρ_{amb} is the ambient air density, $u = Mc$ is the air velocity, and c is the speed of sound at the ambient temperature.

The ambient temperature, pressure, and water vapor density are found from the annual reference standard atmosphere for low-latitudes [106]. At such locations, seasonal variations are not significant, and so for an altitude of $0 \leq h \leq 10$ km, the temperature, T_{amb} in K, pressure, p_{amb} in kPa, and water vapor density, $\rho_{v,amb}$ in kg/m^3, are given by:

$$T_{atm}(h) = 300.4222 - 6.3533h + 0.005886h^2 \tag{E.42}$$

$$p_{atm}(h) = 1001.20306 - 10.90338h + 0.36316h^2 \tag{E.43}$$

$$\rho_{v,amb}(h) = 19.6542 \exp(-0.2313h - 0.1122h^2 + 0.01351h^3 - 0.0005923h^4) \tag{E.44}$$

These are valid for all of the altitudes considered as part of this work, which are well below 10 km. The ambient density follows from the ideal gas law as: $\rho_{amb} = \frac{p_{amb}}{R_a T_{amb}}$, where R_a = 287.05 J/kgK is the specific gas constant for air.

The water vapor density can be used to find the vapor pressure, in kPa, for a given altitude as:

$$e = \frac{\rho_{v,amb}(h)T(h)}{2167} \tag{E.45}$$

Then, the mixture pressure is given by:

$$p_{mix} = p_{amb}(h) + e \tag{E.46}$$

Next, the saturation vapor pressure can be found from the Buck equation as [107]:

$$e_s = \frac{\rho_{v,amb}(h)T(h)}{2167} \tag{E.47}$$

Finally, the humidity ratio ω, specific humidity x_w, and relative humidity RH are found as:

$$\omega = \frac{eM_v}{M_a(p_{mix} - e)} \tag{E.48}$$

$$x_w = \frac{eM_v}{M_a\left(p_{mix} - \left(1 - \frac{M_v}{M_a}\right)e\right)} \tag{E.49}$$

$$RH = 100 \times \frac{e}{e_s} \tag{E.50}$$

where M_v = 18.02 g/mol and M_a = 28.97 g/mol are the molar masses of water vapor and air respectively.

Bibliography

[1] Yunus A. Cengel and Michael A. Boles. *Thermodynamics: an engineering approach*. McGraw-Hill Education, eighth edition edition, 2015.

[2] David M. Romps. Accurate expressions for the dew point and frost point derived from the Rankine-Kirchhoff approximations. *Journal of the Atmospheric Sciences*, in press, 2021.

[3] Xiao Huang, Nick Tepylo, Valérie Pommier-Budinger, Marc Budinger, Elmar Bonaccurso, Philippe Villedieu, and Lokman Bennani. A survey of icephobic coatings and their potential use in a hybrid coating/active ice protection system for aerospace applications. *Progress in Aerospace Sciences*, 105:74–97, 2019.

[4] Y. Zhao, Q. Guo, T. Lin, and P. Cheng. A review of recent literature on icing phenomena: Transport mechanisms, their modulations and controls. *International Journal of Heat and Mass Transfer*, 159:120074, Oct 2020.

[5] Christian J.L. Hermes. An analytical solution to the problem of frost growth and densification on flat surfaces. *International Journal of Heat and Mass Transfer*, 55(23–24):7346–7351, 2012.

[6] Christian JL Hermes, Robson O Piucco, Jader R Barbosa Jr, and Cláudio Melo. A study of frost growth and densification on flat surfaces. *Experimental Thermal and Fluid Science*, 33(2):371–379, 2009.

[7] Christian J.L. Hermes, Valter S. Nascimento Jr., Felipe R. Loyola, Rodrigo P. Cardoso, and Andrew D. Sommers. A study of frost build-up on hydrophilic and hydrophobic surfaces under forced convection conditions. *Experimental Thermal and Fluid Science*, 100:76–88, 2018.

[8] Christian JL Hermes, Felipe R Loyola, and Valter S Nascimento Jr. A semi-empirical correlation for the frost density. *International journal of refrigeration*, 46:100–104, 2014.

[9] Aurélia Léoni, Michèle Mondot, François Durier, Rémi Revellin, and Philippe Haberschill. State-of-the-art review of frost deposition on flat surfaces. *International Journal of Refrigeration*, 68:198–217, 2016.

[10] Dong-Keun Yang and Kwan-Soo Lee. Dimensionless correlations of frost properties on a cold plate. *International Journal of Refrigeration*, 27(1):89–96, 2004.

[11] Max Kandula. Frost growth and densification on a flat surface in laminar flow with variable humidity. *International communications in heat and mass transfer*, 39(8):1030–1034, 2012.

[12] Kwan-Soo Lee, Sung Jhee, and Dong-Keun Yang. Prediction of the frost formation on a cold flat surface. *International journal of heat and mass transfer*, 46(20):3789–3796, 2003.

[13] W Wang, QC Guo, WP Lu, YC Feng, and W Na. A generalized simple model for predicting frost growth on cold flat plate. *international journal of refrigeration*, 35(2):475–486, 2012.

[14] Y Hayashi, A Aoki, S Adachi, and K Hori. Study of frost properties correlating with frost formation types. 1977.

[15] Dennis O'Neal and D. Tree. Measurement of frost growth and density in a parallel plate geometry. *ASHRAE Transactions*, 90:278–290, 1984.

[16] B Jones and J Parker. Frost variation with varying environmental parameters. *ASME J. Heat Transf.*, 97:255–259, 1975.

[17] Kwan-Soo Lee, Woo-Seung Kim, and Tae-Hee Lee. A one-dimensional model for frost formation on a cold flat surface. *International Journal of Heat and Mass Transfer*, 40(18):4359–4365, 1997.

[18] JD Yonko and CF Sepsy. An investigation of the thermal conductivity of frost while forming on a flat horizontal plate. *ASHRAE Transactions*, 73:1.1–1.11, 1967.

[19] L Cai, R Wang, P Hou, and X Zhang. Study on restraining frost growth at initial stage by hydrophobic coating and hygroscopic coating. *Energy Build*, 43:1159–1163, 2011.

[20] R. Östin and S. Andersson. Frost growth parameters in a forced air stream. *International Journal of Heat and Mass Transfer*, 34(4–5):1009–1017, Apr 1991.

[21] Ando Masanao, Satoh Osamu, Uryu Shijo, and Ohara Koichi. Air cycle machine and air conditioning system using the same, U.S. Patent 6 427 471 B1, Aug. 2002.

[22] Caroline Laforte, Caroline Blackburn, and Jean Perron. A review of icephobic coating performances over the last decade. pages 2015–01–2149, 2015.

[23] Liqun Ma, Zichen Zhang, Linyue Gao, Yang Liu, and Hui Hu. *Bio-Inspired Icephobic Coatings for Aircraft Icing Mitigation: A Critical Review*, page 171–201. Wiley, 1 edition, 2021.

[24] Peyman Irajizad, Sina Nazifi, and Hadi Ghasemi. Icephobic surfaces: Definition and figures of merit. *Advances in Colloid and Interface Science*, 269:203–218, 2019.

[25] Y. Tu and G. P. Lin. Dynamic simulation of aircraft environmental control system based on flowmaster. *Journal of Aircraft*, 48(6):2031–2041, 2011.

[26] Philip Jordan and Gerhard Schmitzm. A modelica library for scalable modelling of aircraft environmental control systems. page 599–608, 2014.

[27] A.P.P. Santos, C.R. Andrade, and E.L. Zaparoli. A thermodynamic study of air cycle machine for aeronautical applications. *International Journal of Thermodynamics*, 17(3):117, Sep 2014.

[28] Daniel Bender. Integration of exergy analysis into model-based design and evaluation of aircraft environmental control systems. *Energy*, 137:739–751, 2017.

[29] Ian Jennions, Fakhre Ali, Manuel Esperon Miguez, and Ignacio Camacho Escobar. Simulation of an aircraft environmental control system. *Applied Thermal Engineering*, 172:114925, 2020.

[30] Lindsey Gonzales. Dynamic modeling and simulation of frost and defrost conditions for refrigeration systems. Master's thesis, University of Illinois at Urbana-Champaign, 2015.

[31] Daniel Linares. Modeling and simulation of an aircraft environmental control system. Master's thesis, University of Montreal, 2016.

[32] Sabin Poudel. Modelling of a generic aircraft environmental control system in modelica. Master's thesis, Linköping University, 2019.

[33] Humphrey J. Maris. Introduction to the physics of nucleation. *Comptes Rendus Physique*, 7(9):946–958, 2006.

[34] Ming Qu, Omar Abdelaziz, Zhiming Gao, and Hongxi Yin. Isothermal membrane-based air dehumidification: A comprehensive review. *Renewable and Sustainable Energy Reviews*, 82:4060–4069, Feb 2018.

[35] D. La, Y.J. Dai, Y. Li, R.Z. Wang, and T.S. Ge. Technical development of rotary desiccant dehumidification and air conditioning: A review. *Renewable and Sustainable Energy Reviews*, 14(1):130–147, Jan 2010.

[36] Xiangjie Chen, Saffa Riffat, Hongyu Bai, Xiaofeng Zheng, and David Reay. Recent progress in liquid desiccant dehumidification and air-conditioning: A review. *Energy and Built Environment*, 1(1):106–130, Jan 2020.

[37] Kishor S. Rambhad, Pramod V. Walke, and D.J. Tidke. Solid desiccant dehumidification and regeneration methods—a review. *Renewable and Sustainable Energy Reviews*, 59:73–83, Jun 2016.

[38] Zhiming Gao, Omar Abdelaziz, and Ming Qu. Modeling and simulation of membrane-based dehumidification and energy recovery process. *2017 ASHRAE Winter Conference*, 2017.

[39] Weixing Yuan, Yunxiang Li, and Chenjie Wang. Comparison study of membrane dehumidification aircraft environmental control systems. *Journal of Aircraft*, 49(3):815–821, May 2012.

[40] Bo Yang, Weixing Yuan, Feng Gao, and Binghan Guo. A review of membrane-based air dehumidification. *Indoor and Built Environment*, 24(1):11–26, Feb 2015.

[41] Bo Yang, Weixing Yuan, Xiangming Kong, Tianqi Zheng, and Feifei Li. Mass transfer study on high-pressure membrane dehumidification applied to aircraft environmental control system. *International Journal of Heat and Mass Transfer*, 202:123680, Mar 2023.

[42] Jason Woods. Membrane processes for heating, ventilation, and air conditioning. *Renewable and Sustainable Energy Reviews*, 33:290–304, May 2014.

[43] *Materials Science of Membranes for Gas and Vapor Separation*. Wiley, 1 edition, Jun 2006.

[44] Edward A. Mason and A. P. Malinauskas. *Gas transport in porous media: the dusty-gas model*. Chemical engineering monographs. Elsevier, Amsterdam; New York, 1983.

[45] R. Datta, S. Dechapanichkul, J.S. Kim, L.Y. Fang, and Uehara H. A generalized model for the transport of gases in porous, non-porous, and leaky membranes. i. application to single gases. *Journal of Membrane Science*, 75(3):245–263, Dec 1992.

[46] *Encyclopedia of Membranes*. Springer Berlin Heidelberg, Berlin, Heidelberg, 2016.

[47] J.G. Wijmans and R.W. Baker. The solution-diffusion model: a review. *Journal of Membrane Science*, 107(1–2):1–21, Nov 1995.

[48] Philip Alei, Jeffrey Schletz, John Jensvold, Ward Tegrotenhuis, Wickham Allen, Frederick Coan, Karen Skala, Daniel Clark, and Harold Wait Jr. Loom processing of hollow fiber membranes, U.S. Patent 5 598 874, Feb. 1997.

[49] Frederick Coan and John Jensvold. Air dehydration membrane, U.S. Patent 7 249 174 B2, Nov. 2007.

[50] Frederick Coan and Jeffrey Schletz. Integrated membrane module for gas dehydration and gas separation, U.S. Patent 8 398 755 B2, Mar. 2013.

[51] S. A. Stern. The “barrer” permeability unit. *Journal of Polymer Science Part A-2: Polymer Physics*, 6(11):1933–1934, Nov 1968.

[52] Oleksandr Tanskyi. Zeolite membrane water vapor separation for building air-conditioning and ventilation systems. doctoral dissertation, texas a amp; m university. 2015.

[53] Ho Bum Park, Jovan Kamcev, Lloyd M. Robeson, Menachem Elimelech, and Benny D. Freeman. Maximizing the right stuff: The trade-off between membrane permeability and selectivity. *Science*, 356(6343):eaab0530, Jun 2017.

[54] Jong Hak Kim. Grand challenges in membrane applications—gas and vapor. *Front. Membr. Sci. Technol.*, 1, 2022.

[55] S Metz, W Vandeven, J Potreck, M Mulder, and M Wessling. Transport of water vapor and inert gas mixtures through highly selective and highly permeable polymer membranes. *Journal of Membrane Science*, 251(1–2):29–41, Apr 2005.

[56] F. H. Akhtar, M. Kumar, L. F. Villalobos, H. Vovusha, R. Shevate, U. Schwingenschlögl, and K.-V. Peinemann. Polybenzimidazole-based mixed membranes with exceptionally high water vapor permeability and selectivity. *J. Mater. Chem. A*, 5(41):21807–21819, 2017.

[57] Faheem Hassan Akhtar, Hakkim Vovushua, Luis Francisco Villalobos, Rahul Shevate, Mahendra Kumar, Suzana Pereira Nunes, Udo Schwingenschlögl, and Klaus-Viktor Peinemann. Highways for water molecules: Interplay between nanostructure and water vapor transport in block copolymer membranes. *Journal of Membrane Science*, 572:641–649, Feb 2019.

[58] Fengkai Wang, Shurui Han, Yanli Zhang, Lei Gao, Xu Li, Lizhi Zhao, Hui Ye, Hong Li, Qingping Xin, and Yuzhong Zhang. Constructing rapid water vapor transport channels within mixed matrix membranes based on two-dimensional mesoporous nanosheets. *Communications Chemistry*, 5(1):65, May 2022.

[59] The Mathworks Inc. *Simscape™ Language Guide, R2021b*, 2021.

[60] HW Schneider. Equation of the growth rate of frost forming on cooled surfaces. *International Journal of Heat and Mass Transfer*, 21(8):1019–1024, 1978.

[61] Shao-Ming Li and Chi-Chuan Wang. Predictive models on the frost formation for plain surface - a review and comparative study. *International Communications in Heat and Mass Transfer*, 129:105670, Dec 2021.

[62] R. Le Gall, J.M. Grillot, and C. Jallut. Modelling of frost growth and densification. *International Journal of Heat and Mass Transfer*, 40(13):3177–3187, 1997.

[63] Byeongchul Na and Ralph L. Webb. Mass transfer on and within a frost layer. *International Journal of Heat and Mass Transfer*, 47(5):899–911, 2004.

[64] Christian JL Hermes, Andrew D Sommers, Colton W Gebhart, and Valter S Nascimento Jr. A semi-empirical model for predicting frost accretion on hydrophilic and hydrophobic surfaces. *International Journal of Refrigeration*, 87:164–171, 2018.

[65] Andrew D. Sommers, Andrew C. Napora, Nicholas L. Truster, Edgar J. Caraballo, and Christian J.L. Hermes. A semi-empirical correlation for predicting the frost density on hydrophilic and hydrophobic substrates. *International Journal of Refrigeration*, 74:313–323, Feb 2017.

[66] Christian J.L. Hermes, Andrew D. Sommers, and Jader R. Barbosa. Time scaling of frost accretion and the square-root-of-time rule. *International Communications in Heat and Mass Transfer*, 108:104281, 2019.

[67] M. Popovac, J. Emhofer, and Ch. Reichl. Frosting in a heat pump evaporator part b: Numerical analysis. *Applied Thermal Engineering*, 199:117488, Nov 2021.

[68] S. M. Sami and T. Duong. Mass and heat transfer during frost growth. *ASHRAE Transactions*, 95:158–165, 1989.

[69] Y. X. Tao, R. W. Besant, and Y. Mao. Characteristics of frost growth on a flat plate during the early growth period. *ASHRAE Transactions: Symposia, Ch-93-2-2*, pages 746–753, 1993.

[70] S.A Sherif, S.P Raju, M.M Padki, and A.B Chan. A semi-empirical transient method for modelling frost formation on a flat plate. *International Journal of Refrigeration*, 16(5):321–329, Jan 1993.

[71] Chin-Hsiang Cheng and Yu-Chieh Cheng. Predictions of frost growth on a cold plate in atmospheric air. *International Communications in Heat and Mass Transfer*, 28(7):953–962, Oct 2001.

[72] Y.B. Lee and S.T. Ro. Analysis of the frost growth on a flat plate by simple models of saturation and supersaturation. *Experimental Thermal and Fluid Science*, 29(6):685–696, Jul 2005.

[73] Max Kandula. Frost growth and densification in laminar flow over flat surfaces. *International Journal of Heat and Mass Transfer*, 54(15–16):3719–3731, Jul 2011.

[74] Yunus A. Cengel and Afshin J. Ghajar. *Heat and mass transfer: fundamentals applications*. McGraw Hill Education, fifth edition edition, 2015.

[75] B.D Storey and A.M Jacobi. The effect of streamwise vortices on the frost growth rate in developing laminar channel flows. *International Journal of Heat and Mass Transfer*, 42(20):3787–3802, 1999.

[76] Merle C. Potter, Jack L. Goldberg, and Edward Aboufadel. *Advanced engineering mathematics*. Oxford University Press, New York, 3rd ed edition, 2005.

[77] John H. Lienhard and John H. Lienhard. *A heat transfer textbook*. Phlogiston Press, Cambridge, M.A., 4th ed edition, 2017.

[78] Chris Tofallis. A better measure of relative prediction accuracy for model selection and model estimation. *Journal of the Operational Research Society*, 66(8):1352–1362, 2015.

[79] J Niu. Membrane-based enthalpy exchanger: material considerations and clarification of moisture resistance. *Journal of Membrane Science*, 189(2):179–191, Aug 2001.

[80] L Zhang, C Liang, and L Pei. Heat and moisture transfer in application scale parallel-plates enthalpy exchangers with novel membrane materials. *Journal of Membrane Science*, 325(2):672–682, Dec 2008.

[81] Jingchun Min and Ming Su. Performance analysis of a membrane-based energy recovery ventilator: Effects of membrane spacing and thickness on the ventilator performance. *Applied Thermal Engineering*, 30(8–9):991–997, Jun 2010.

[82] Hui Yu, Xing Yang, Rong Wang, and Anthony G. Fane. Numerical simulation of heat and mass transfer in direct membrane distillation in a hollow fiber module with laminar flow. *Journal of Membrane Science*, 384(1–2):107–116, Nov 2011.

[83] Khin Zaw, M. Reza Safizadeh, Joachim Luther, and Kim Choon Ng. Analysis of a membrane based air-dehumidification unit for air conditioning in tropical climates. *Applied Thermal Engineering*, 59(1–2):370–379, Sep 2013.

[84] Weixing Yuan, Bo Yang, Binghan Guo, Xiangping Li, Yansheng Zuo, and Wenchao Hu. A novel environmental control system based on membrane dehumidification. *Chinese Journal of Aeronautics*, 28(3):712–719, Jun 2015.

[85] Yilin Liu, Xin Cui, Weichao Yan, Jincai Su, Fei Duan, and Liwen Jin. Analysis of pressure-driven water vapor separation in hollow fiber composite membrane for air dehumidification. *Separation and Purification Technology*, 251:117334, 2020.

[86] Thuan Duc Bui, Feng Chen, Aqdas Nida, Kian Jon Chua, and Kim Choon Ng. Experimental and modeling analysis of membrane-based air dehumidification. *Separation and Purification Technology*, 144:114–122, 2015.

[87] Li-Zhi Zhang, Cai-Hang Liang, and Li-Xia Pei. Conjugate heat and mass transfer in membrane-formed channels in all entry regions. *International Journal of Heat and Mass Transfer*, 53(5–6):815–824, Feb 2010.

[88] L Zhang. Fabrication of a lithium chloride solution based composite supported liquid membrane and its moisture permeation analysis. *Journal of Membrane Science*, 276(1–2):91–100, May 2006.

[89] Frank Lipnizki and Robert W Field. Mass transfer performance for hollow fibre modules with shell-side axial feed flow: using an engineering approach to develop a framework. *Journal of Membrane Science*, 193(2):195–208, Nov 2001.

[90] Lixin Mi and Sun-Tak Hwang. Correlation of concentration polarization and hydrodynamic parameters in hollow fiber modules. *Journal of Membrane Science*, 159(1–2):143–165, Jul 1999.

[91] Paul Scovazzo and Ramsay MacNeill. Membrane module design, construction, and testing for vacuum sweep dehumidification (vsd): Part i, prototype development and module design. *Journal of Membrane Science*, 576:96–107, Apr 2019.

[92] Li-Zhi Zhang and Si-Min Huang. Coupled heat and mass transfer in a counter flow hollow fiber membrane module for air humidification. *International Journal of Heat and Mass Transfer*, 54(5–6):1055–1063, Feb 2011.

[93] Frank P. Incropera, David P. DeWitt, Theodore L. Bergman, and Adrienne S. Lavine. *Fundamentals of Heat and Mass Transfer*. John Wiley Sons, Inc., New York City, New York, 6th edition, 2007.

[94] Yilin Liu, John C. Chai, Xin Cui, Weichao Yan, Na Li, and Liwen Jin. Multi-objective optimization of air dehumidification membrane module based on response surface method and genetic algorithm. *Energy Reports*, 9:2201–2212, Dec 2023.

[95] Baiwang Zhao, Liang-Yi Wang, and Tai-Shung Chung. Enhanced membrane systems to harvest water and provide comfortable air via dehumidification moisture condensation. *Separation and Purification Technology*, 220:136–144, 2019.

[96] Sebastian Englart and Krzysztof Rajski. Performance investigation of a hollow fiber membrane-based desiccant liquid air dehumidification system. *Energies*, 14(11):3320, 2021.

[97] Adele Brunetti, Francesca Macedonio, Giuseppe Barbieri, and Enrico Drioli. Membrane condenser as emerging technology for water recovery and gas pre-treatment: current status and perspectives. *BMC Chemical Engineering*, 1(1):19, 2019.

[98] D. H. Cooke. On prediction of off-design multistage turbine pressures by stodola's ellipse. *Journal of Engineering for Gas Turbines and Power*, 107(3):596–606, Jul 1985.

[99] Aurel Stodola. *Steam and gas turbines : with a supplement on The prospects of the thermal prime mover*. McGraw-Hill, New York, 1927.

[100] R. O. Piucco. *Análise teórico-experimental da formação de geada em refrigeradores domésticos*. PhD thesis, Federal University of Santa Catarina, Florianópolis, Brazil, 2008.

[101] R.K. Shah and D.P. Sekulic. *Fundamentals of Heat Exchanger Design*. John Wiley Sons, Inc., Hoboken, New Jersey, 1st edition, 2003.

[102] Guoxiang Gu, S. Banda, and A. Sparks. An overview of rotating stall and surge control for axial flow compressors. In *Proceedings of 35th IEEE Conference on Decision and Control*, volume 3, page 2786–2791, Kobe, Japan, 1996. IEEE.

[103] E. M. Greitzer. Surge and rotating stall in axial flow compressors—part i: Theoretical compression system model. *Journal of Engineering for Power*, 98(2):190–198, Apr 1976.

[104] E. M. Greitzer. Surge and rotating stall in axial flow compressors—part ii: Experimental results and comparison with theory. *Journal of Engineering for Power*, 98(2):199–211, Apr 1976.

[105] E. M. Greitzer and et al. N+3 aircraft concept designs and trade studies, final report volume 2: Appendices—design methodologies for aerodynamics, structures, weight, and thermodynamic cycles. *NASA-CR-2010-216794 Vol 2*, 2010.

[106] International Telecommunication Union. *Reference standard atmospheres, Recommendation ITU-R P.835-6*, 2017.

[107] A. L. Buck. New equations for computing vapor pressure and enhancement factor. *J. Appl. Meteorol.*, 20:1527–1532, 1981.